Nonlinear Dynamics and Vibration of Gear and Bearing Systems using A Finite Element/Contact Mechanics (FE/CM) Model and A Hybrid Analytical-Computational (HAC) Model

Xiang Dai

Dissertation submitted to the Faculty of the
Virginia Polytechnic Institute and State University
in partial fulfillment of the requirements for the degree of

Doctor of Philosophy
in
Mechanical Engineering

Robert G. Parker, Chair
Corina Sandu
Lei Zuo
Christopher G. Cooley

Jul. 10, 2017
Blacksburg, Virginia, USA

Keywords: Dynamics, Vibration, Gear

Nonlinear Dynamics and Vibration of Gear and Bearing Systems using A Finite Element/Contact Mechanics (FE/CM) Model and A Hybrid Analytical-Computational (HAC) Model

Xiang Dai

ABSTRACT

This work investigates the nonlinear dynamics and vibration in gear systems, including spur and helical gear pairs, idler gear trains, and planetary gears. The spur gear pairs are analyzed using a finite element/contact mechanics (FE/CM) model. A hybrid analytical-computational (HAC) model is proposed for nonlinear gear dynamics. The HAC predictions are compared with FE/CM results and available experimental data for validation.

Chapter 2 investigates the static and dynamic tooth root strains in spur gear pairs using a finite element/contact mechanics approach. Extensive comparisons with experiments, including those from the literature and new ones, confirm that the finite element/contact mechanics formulation accurately predicts the tooth root strains. The model is then used to investigate the features of the tooth root strain curves as the gears rotate kinematically and the tooth contact conditions change. Tooth profile modifications are shown to strongly affect the shape of the strain curve. The effects of strain gage location on the shape of the static strain curves are investigated. At non-resonant speeds the dynamic tooth root strain curves have similar shapes as the static strain curves. At resonant speeds, however, the dynamic tooth root strain curves are drastically different because large amplitude vibration causes tooth contact loss. There are three types of contact loss nonlinearities: incomplete tooth

contact, total contact loss, and tooth skipping, and each of these has a unique strain curve. Results show that different operating speeds with the same dynamic transmission error can have much different dynamic tooth strain.

Chapters 3, 4, and 5 develops a hybrid-analytical-computational (HAC) method for nonlinear dynamic response in gear systems. Chapter 3 describes the basic assumptions and procedures of the method, and implemented the method on two-dimensional vibrations in spur gear pairs. Chapters 4 and 5 extends the method to two-dimensional multi-mesh systems and three-dimensional single-mesh systems.

Chapter 3 develops a hybrid analytical-computational (HAC) model for nonlinear dynamic response in spur gear pairs. The HAC model is based on an underlying finite element code. The gear translational and rotational vibrations are calculated analytically using a lumped parameter model, while the crucial dynamic mesh force is calculated using a force-deflection function that is generated from a series of static finite element analyses before the dynamic calculations. Incomplete tooth contact and partial contact loss are captured by the static finite element analyses, and included in the force-deflection function. Elastic deformations of the gear teeth, including the tooth root strains and contact stresses, are calculated. Extensive comparisons with finite element calculations and available experiments validate the HAC model in predicting the dynamic response of spur gear pairs, including near resonant gear speeds when high amplitude vibrations are excited and contact loss occurs. The HAC model is five orders of magnitude faster than the underlying finite element code with almost no loss of accuracy.

Chapter 4 investigates the in-plane motions in multi-mesh systems, including the idler

chain systems and planetary gear systems, using the HAC method that introduced in Chap. 3. The details of how to implement the HAC method into those systems are explained. The force-deflection function for each mesh is generated individually from a series of static finite element analyses before the dynamic calculations. These functions are used to calculated the dynamic mesh force in the analytical dynamic analyses. The good agreement between the FE/CM and HAC results for both the idler chain and planetary gear systems confirms the capability of the HAC model in predicting the in-plane dynamic response for multi-mesh systems. Conventional softening type contact loss nonlinearities are accurately predicted by HAC method for these multi-mesh systems.

Chapter 5 investigates the three-dimensional nonlinear dynamic response in helical gear pairs. The gear translational and rotational vibrations in the three-dimensional space are calculated using an analytical model, while the force due to contact is calculated using the force-deflection. The force-deflection is generated individually from a series of static finite element analyses before the dynamic calculations. The effect of twist angle on the gear tooth contact condition and dynamic response are included. The elastic deformations of the gear teeth along the face-width direction are calculated, and validated by comparing with the FE/CM results.

Nonlinear Dynamics and Vibration of Gear and Bearing Systems using A Finite Element/Contact Mechanics (FE/CM) Model and A Hybrid Analytical-Computational (HAC) Model

Xiang Dai

GENERAL AUDIENCE ABSTRACT

Gears are widely used in power transmission systems. The dynamics and vibrations of the gears causes system noise because those vibrations are transmitted to the gear housing through the supporting bearings and shafts. The tooth root strains and stresses are directly related to the system failure. These effect becomes significantly important when the system is operating near resonances that high amplitude vibrations are excited and contact loss nonlinearity occurs. We want a fast, accurate, and reliable model to analyze the nonlinear dynamics in those gear and bearing systems.

This work investigates the dynamics and vibration in gear systems, including spur and helical gear pairs, idler gear chains, and planetary gears. The static and dynamic tooth root strains in spur gear pairs are studied using a finite element/contact mechanics (FE/CM) approach. Extensive comparisons with experiments, including those from the literature and new ones, validates the accuracy of the FE/CM formulation. The model is then used to investigate the features of the tooth root strain curves as the gears rotate kinematically and the tooth contact condition changes. The three types of contact loss nonlinearities are investigated and explained.

A hybrid analytical-computational (HAC) method is developed for nonlinear gear dy-

namics. This model takes advantage of the good features of the different traditional models, and is available for fast and accurate nonlinear gear dynamic analysis. The HAC method is validated by comparing with the FE/CM results, including near resonant gear speeds when high amplitude vibrations are excited and contact loss occurs. The HAC method is five orders of magnitude faster than the underlying finite element code with almost no loss of accuracy.

Acknowledgments

In sincerely thank Professor Robert Parker for his support and guidance of my PhD studies during the past years. As my PhD advisor, he not only helps me solve technical problems during research, but also guides me how to be a qualified engineer. Under his supervision, I learnt how to think, work, and solve problems independently, from which I will benefit during my entire career in the future. His emphasize on high quality research and communication skills also have made deep impressions on me. I thank Professor Parker for the trust, encouragement, patient, and freedom he gives on research, and the effort he has made to give us a comfortable working environment and a positive research atmosphere. I thank him for his friendship and helps in daily life.

I thank Professor Corina Sandu, Lei Zuo, Shane Ross, and Christopher Cooley for serving on my doctoral committee. I thank Professor Sandu for the helps in making my PhD plan of study. I thank Professor Zuo for his help and courage in my academic progress. Professor Ross's excellent teaching in advanced dynamics topics gave me a great inspiration on my research. I would like to especially thank Professor Cooley, for his help and guidance in the start of my PhD study. I thank him for the patient and trust that he gave when I was struggling in detailed research problems. I thank him for the help and guidance in technical

writing and presentation skills. I thank him for his friendship and accompany during my most difficult time in Shanghai.

I thank Dr. Sandeep Vijayakar from Advanced Numerical Solutions LLC., for the use and technical help of his Calyx software. I thank the engineers from Avio Aero, Luca Ronchiato, Paolo Vargue, Paolo Calza, and Alberto Demenego, for their support and their effort in experiments.

I thank the lab members and my dear friends at Shanghai Jiao Tong University, Chunguang Liu, Yue Wu, Zheng Liu, and Chengzhi Shi, for their helps during my early graduate studies. I thank them for their friendship and for the happy days with them. I thank the lab members at Virginia Tech, Xiaoqi Li, Bin Dong, Chenxin Wang, Li Tan, Guanghui Liu, Qiaoyun Yan, Zi Wang, Kedar Vaidya, Emma Pierson, Xueping Xu, Zehua Hu, Yan Song, and Yuhao Zhou, for their friendship and accompany at Blacksburg.

Finally, I would like to thank my family for their help and support. I thank my parents, Jianguo Dai and Lu Dong, for their selfness financial and moral support. I thank my beloved wife, Yao Lu, for her patient, encouragement and sacrifice for my PhD study and for our family. I thank her for taking good care of our child. I thank my dearest baby boy, Daniel Dai. His appearance gives me great encouragement in working hard towards the goals and live with positive attitude and full of hope.

Contents

List of Figures

List of Tables

Chapter 1

Introduction

1.1 Motivation

Gears are important components in many industrial applications. They are widely used in power transmission systems in different types of combinations (like gear chains, planetary gears, and compound gears, etc.) in order to satisfy the requirement of the system. In some applications, like turbofan engines, helicopter and automobile gearboxes, and wind turbines, the reliability of the gears are especially crucial for safety and economy concerns. These gears are taking high loads, or at high speeds, thus causing dynamic problems. The main excitation in gear systems are from the periodically changing tooth contact conditions. The gear vibrations are transmitted to the main structure through bearings, and are directed related to the noise in the system. The large gear tooth root stresses and strains are as a result of dynamic mesh force, which may cause system failure. These effects are especially significant near resonant gear speeds when high amplitude vibrations are excited and contact loss occurs. Understanding and predicting the dynamic response of the gears remains a challenging task for engineers trying to avoid system noise and structural failure in the

designing phase.

Among the many tools for gear dynamics, lumped-parameter models are the most commonly used. These models assume the gears to have rigid bodies, and connected by stiffness elements. For unmodified or slightly modified gears, the lumped-parameter models can usually predict the gear translational and rotational vibrations with acceptable accuracy and relatively high computational efficiency. For the gears with significant modifications, however, conventional lumped-parameters are lack of accuracy. Additionally, as lumped parameter models assume the gear bodies to be rigid, the elastic deformations in the gear body and tooth contact zone can not be calculated directly.

The gears are also studied using finite element methods. When the gear teeth are engaged, the elastic deformation in the contact zone is orders of magnitude smaller than that in the gear body, a highly refined finite element mesh is usually needed near the tooth contact region. Additionally, as the gears are rotating kinematically, the contact location moves along the tooth surface. Therefore, the finite element mesh needs to be regenerated for each time step or the entire tooth surface requires a highly refined mesh. Either option is computationally inefficiency. As a result, most conventional finite element codes are not built for gear dynamic analyses.

A finite element/contact mechanics (FE/CM) model has been developed for contact problems in multi-body dynamic, and applied to gear dynamic analyses. This model combines an analytical solution for the tooth contact and conventional finite element solutions for the elastic gear teeth and blank. The micro-geometry on the tooth contact surface due to tooth profile and lead modifications is precisely modeled. Dynamic analyses are possible

using this model because of its high computational efficiency. For gear pairs, it takes a few hours to reach steady state of the system. For planetary gears or system level gear boxes, however, the FE/CM model still lacks of computational efficiency. It may take weeks to get the steady state response for these systems at a particular speed and load condition.

There are few methods available for fast and accurate predictions of the dynamic response in gear systems, especially for the systems with complicated structure and multiple tooth contact. Those that do exist have either too strong simplifications or relatively low computational efficiency. We want a reliable, fast, and accurate model for nonlinear gear dynamics.

1.2 Literature Review

1.2.1 Analytical Lumped-Parameter models

The gears have been studies analytically for decades using lumped-parameter models, that is, assuming the gears to have rigid bodies, and are connected by stiffness elements. Works prior to 1996 using lumped-parameter models on gear dynamics can be found in the review articles [4, 5]. More recent works are found in Ref. [6], which focuses on the nonlinear dynamics in gear systems. In an early work, Gregory et al. [7] investigated the dynamic behavior of spur gear pairs. The peak-to-peak transmission error is compared with experiments. Blankenship and Singh [8, 9] investigated the three-dimensional vibrations in helical gears using a mesh interface dynamic model. Velex and Maatar [5] investigated the

dynamic response in gear pairs. Their model includes gear tooth modifications and mounting errors. Velex and Ajmi [10] studied helical gear pair systems using a lumped-parameter model that excited by transmission errors. Eritenel and Parker [11, 12] investigated the three-dimensional nonlinear vibration of gear pairs using a lumped-parameter model with discretized stiffness network. The effect of partial contact loss, where portions of gear teeth contact lines losing contact, is captured. Palermo et al. [13] introduced a three-dimensional mesh interface model for multi-body dynamics simulations. Eritenel and Parker [14] investigated the nonlinear vibration of spur gear pairs using a lumped-parameter model. The closed-form solution of the nonlinear gear vibrations are given from a perturbation method. Cooley et al. [15] compared two approaches of calculating the gear tooth mesh stiffness, which is commonly used in lumped-parameter models.

There are other works on gear pairs using lumped-parameter models. The parametric instability in gear pairs are investigated in Refs. [16, 17, 18]. The bifurcation in gear pairs due to backlash is investigated in Refs. [19, 20, 21]. Lumped-parameter models assume that the gears have rigid gear bodies, the tooth root stresses and strains due to elasticity are not calculated directly. The dynamic tooth root stresses are calculated in Refs. [22, 23, 24] using analytical expressions for tooth root stresses that depend on dynamic tooth forces from the lumped-parameter model.

The models discussed above does not incorporate the effect of friction at the contact surface. In early works, elasto-hydrodynamic lubrication and tribology theory are used to derive the theoretical friction coefficients [25, 26, 27]. Velex and Cahouet [28] investigated the influence of tooth friction in spur and helical gear pairs using a lumped-parameter model,

and compared with experiments. Vaishya and Singh [29, 30] developed a nonlinear lumped-parameter model for spur gear pairs including coulomb frictions. The excitation consists of three separate terms, that is, unloaded transmission error, time invariant external torque, and the periodically varying sliding friction force. Vaishya and Singh [31] compared the strategies for modeling friction in gear pair systems. Liu and Parker [32] investigated the impact of tooth friction and its bending effect on gear dynamics. The excitations from periodically changing friction bending is incorporated.

The lumped-parameter models are also used in studies for multi-mesh idler gear chain systems [33, 34, 35, 36, 37]. Lin and Parker [33, 34] investigated the parametric instability in three-gear systems. The effects from mesh stiffness, contact ratios, and mesh phasing are studied. Liu and Parker [35] developed a lumped-parameter model for multi-mesh gear vibrations. Their model includes time-varying mesh stiffnesses, profile modifications, and contact losses. Liu and Parker [36] gave closed-form expressions for three-gear systems using a perturbation method. The perturbation results are validated by numerical integration and harmonic balance. Liu and Parker [37] investigated the frequency response for two-stage counter-shaft gear systems using the method multiple scales.

The lumped-parameter models are used extensively for the more complicated planetary gear systems. Studies prior to 1992 on planetary gears are found in the review article [38]. More recent works about planetary gears using lumped parameter models are found in Ref. [39]. In an early work, Cunliffe et al. [40] investigated the dynamic tooth loads in epicyclic gears using a thirteen degree of freedom model. The natural frequency and vibration modes of the system are analyzed and studied. Botman [41] developed an eighteen degree of freedom

model for planetary gears. The effects from carrier rotation and variation of planet bearing stiffness are included. Frater et al. [42] extended Botman's model [41], and studied the vibration in planetary gear systems with unequal planet stiffnesses. Kahraman [43] investigated the natural modes of planetary gear systems. The planet translations are described in Cartesian coordinates. Saada and Velex [44] developed an extended lumped parameter model for planetary gears. The generalized displacements are expressed in the rotating frames. Lin and Parker [45] derived the equation of motion for general planetary gear systems using a lumped parameter model, and investigated the modal properties at low speed. They revealed the three types of mode shapes in the systems with identical and equally spaced planet gears. Lin and Parker [46] systematically investigated the natural frequency and vibration mode sensitivities to key planetary gear design parameters using the same lumped-parameter model. Lin and Parker [47] investigated the structured vibration characteristics of planetary gears with unequally spaced planets. Lin and Parker [48] studied the eigenvalue veering phenomena in planetary gears. The influence of model parameters on free vibrations are more fully defined using the veering results, along with the modal properties and eigensensitivity analysis [45, 46]. Sun and Hu [49] investigated the nonlinear dynamics of a planetary gear system with back lash and time-varying mesh stiffness using a lumped-parameter model. Abousleiman and Velex [50] developed a hybrid three-dimensional finite element/lumped parameter model for quasi-static and dynamic analyses for planetary/epicyclic gear systems. Ambarisha and Parker [51] investigated the nonlinear dynamics of planetary gears using a lumped-parameter model. The analytical results are compared with a computational model. Shyyab and Kahraman [52] developed a lumped-parameter model for planetary gears. The model includes all possible power flow configurations. Eritenel and Parker [53] investigated

the modal properties of helical planetary gear system with equally spaced planet using a three-dimensional lumped-parameter model that allows for six degrees of freedom per gear-shaft body. Guo and Parker [54, 55] investigated the nonlinear vibrations in spur planetary gear systems. The tooth wedging and bearing clearance nonlinearities are included. Bahk and Parker [56, 57] gave closed-form solutions for the planetary gear systems near primary, sub- and super-harmonic resonances using a perturbation analysis. The analytical results are validated with finite element, numerical integration, and harmonic balance solutions. Ericson and Parker [58] systematically studied the planetary gear modal vibrations using a lumped-parameter model. The results are correlated against computational results and experimental measurements.

The dynamic response in planetary gear systems is highly affected by the phase relationship between the planet gears, there are studies about the planet phase using lumped-parameter models. Seager [59] analytically shows that the potentially troublesome harmonic components can be neutralized by choosing the proper tooth numbers, by which the planet phase is changed. August and Kasuba [60] and Velex and Flammand [61] analytically observed the dramatic impact of mesh phasing on the dynamic response of planetary gear systems. Kahraman [62] investigated the effects of the planet mesh phasing on the dynamic response of a four-planet system using a lumped-parameter model excited by fluctuating static transmission error. Parker [63] gave a physical explanation for the effectiveness of planet phasing to suppress planetary gear vibration. Lin and Parker [64] provided the necessary relationships to properly incorporate mesh phasing in analytical models. Ambarisha and Parker [65] analytically derived design rules for planetary gears in the purpose of suppress

certain harmonics of planet mode response through mesh phasing.

There are other works on planetary gears using lumped-parameter models and focusing on other topics. Lin and Parker [66] investigated the planetary gear parametric instability caused by mesh stiffness variation. Canchi and Parker [67] investigated the effect of ring-planet mesh phasing and contact ratio on the parametric instabilities of a planetary gear ring. The load sharing in planetary gears are investigated in Refs. [68, 69, 70, 71, 72, 73, 74, 75]. Inalpolat and Kahraman [76] investigated the dynamic response of multi-stage planetary gears. Inalpolat and Kahraman [77, 78] developed a lumped-parameter model to predict dynamic response of planetary gears with manufacturing errors. The results are compared with experimental measurements. Cooley and Parker [79] investigated the vibration properties of high speed planetary gears. The gyroscopic effects and centrifugal forces are included. The critical speed properties and stability findings of the same system is identified and proved in Ref. [80]. An unusual gyroscopic system eigenvalue behavior in these high speed planetary gears are observed and explained in their following work [81]. In Refs. [50, 82, 83, 84, 85], the planetary gears with continuum ring gear is studied. The compound gear system are studied in Refs. [86, 87, 88, 89, 90]. Sondkar and Kahraman [91] developed an analytical model for double-helical planetary gear sets. Ericson and Parker [92] investigated the natural frequency clusters in planetary gear systems.

Lumped parameter models are also used in commercial codes for gear dynamics, like ADAMS, Simpack, Romax, RecurDyn, etc.

1.2.2 Conventional Finite Element Models

Conventional finite element methods are also used for analyzing gear systems [93, 94, 95, 96, 97, 98, 99, 100, 101, 102, 103]. These works focus static conditions as conventional finite element methods are usually not designed for gear dynamic analysis. Because the elastic deformations in the contact zones is orders of magnitude smaller than the gear body, a highly refined finite element mesh is required in the tooth contact zone. As the gears are rotating kinematically, the contact location moves along the gear teeth. Therefore, re-meshing is needed or the entire tooth surfaces need to have a highly refined mesh. Either option is computationally inefficient. As a result, most conventional finite element codes for gear systems are built for only static analyses.

1.2.3 Finite Element/Contact Mechanics Model

A finite element/contact mechanics (FE/CM) model has been developed by Dr. Vijayakar and co-workers for contact problems in multi-body dynamics [104, 105, 106]. The formulation is summarized for gear dynamics applications in Refs. [107, 108, 109]. The gear body is divided into two parts: an inner region near the tooth contact, and an outer region for the elastic gear body away from tooth contact. Near the tooth contact, an analytical solution for a point force on an elastic half space is used to calculate the tooth contact pressure. Away from the tooth contact, the deformations in the gear bodies are calculated using conventional finite element method. The two solutions are matched along an interface near the tooth contact. The interface is chosen carefully so that both the analytical and finite ele-

ment solutions remain valid. Using this method, only a relatively coarse finite element mesh is required for the gear body. Additionally, the same finite element mesh can be used as the gears rotate kinematically: no re-meshing is necessary. Dynamic analyses are possible using the finite element/contact mechanics model because of its high computationally efficiency.

There are studies about gear static and dynamic analyses using the FE/CM model. Parker et al. [107] presented comprehensive dynamic response results for in-plane motions of a planetary gear system using the FE/CM model. Parker et al. [108] investigated the nonlinear dynamic response of two-dimensional spur gear pairs using the FE/CM model. Classical softening type nonlinearities, including the jump-up and jump-down frequencies are accurately captured, and validated against experiments. Kahraman and Vijayakar [110] studied the effect of internal gear flexibility on the quasi-static behavior of a planetary gear set. Kahraman et al. [111] analyzed a planetary gear system with thin rim. Bodas and Kahraman [112] studied the effect of manufacturing and assembly errors on the static load sharing in planetary gears. Cheon and Parker [113] investigated the influence of manufacturing errors on the dynamic response of planetary gears. The effect of bearing stiffness on the static properties of planetary gear systems with manufacturing errors are studied in the following work [114]. Yuksel and Kahraman [115] investigated the dynamic tooth loads of planetary gears having tooth wear. Singh [116] investigated the load sharing in three-dimensional planetary gear systems. The influence of planetary needle bearings on the performance of single and double pinion planetary systems are studied in Ref. [117]. Ambarisha and Parker [51] validated the strong nonlinear behavior that observed from analytical results using the FE/CM model. Tamminana et al. [118] studied the relationship

between the dynamic factors and the dynamic transmission error of spur gear pairs using the same FE/CM formulation. The dynamic factors defined by transmission error, mesh force, tooth load, and bending stresses over a wide speed range are calculated and compared with experiments. Cooley et al. [109] developed a frequency domain finite element approach for three-dimensional gear dynamics. Ericson and Parker [58] studied the modal vibrations in planetary gears, and correlated against experimental measurements.

The finite element/contact mechanics model is also used for contact problems in rolling element bearings. Guo and Parker [119] investigated the features of stiffnesses in rolling element bearings. They focused on obtaining accurate bearing stiffness for a wide range of bearing types and parameters. The computational model includes all the important detailed geometry features of rolling element bearings.

1.2.4 Experiments

The gears are studied statically and dynamically in experiments. In early works, the gear rotational vibrations are measured in Refs. [5, 7]. Kahraman and Blankenship [2, 120, 121] studied the nonlinear behavior in gears through a series of experiments. The effects of clearance, gear involute contact ratio, and involute tip relief on the nonlinear dynamic response of spur gear pairs are studied. Inalpolat and Kahraman [77] measured the modulation sidebands of planetary gears, and compared with analytical predictions. Ericson and Parker [58] investigated the modal vibrations of planetary gears using analytical, computational, and experimental methods, and compared the results with each other. The natural frequency, mode shape, and dynamic response of planetary gears are experimentally

obtained.

Tooth root stresses have been studied experimentally using photo-elastic methods for spur gear pairs in Refs. [122, 123] and planetary gears in Ref. [124]. Photo-elastic methods show stress distributions and locations of the maximum stress. Strain gages are used to measure tooth root strains for gear pairs in Refs. [1, 22, 97, 125, 126, 127] and planetary gears in Refs. [128, 129, 130, 131, 132, 133, 134]. The dynamic tooth contact stresses in gears are not directly measured in experiments.

1.3 Research Objectives

In Chapter 2 the gears are analyzed using the FE/CM model. The dynamic transmission error and static and dynamic tooth root strains are predicted for individual unity-ratio spur gear pairs. Extensive comparisons against available experimental data validated the FE/CM model, including near resonant gear speeds when high amplitude vibrations are excited and contact loss occurs. The validated model is then used to investigate the features of the static and dynamic strain curves. The static strain curves are explained using instantaneous tooth contact conditions for both modified and unmodified gears. The dynamic strain curves are explained using phase and amplitude of dynamic transmission error. The dynamic strain curves and tooth contact conditions for the three types of contact loss nonlinearities, that is, incomplete tooth contact, total contact loss, and tooth skipping, are given and explained.

Chapter 3 developed a hybrid analytical-computational (HAC) model for fast and accurate gear dynamic analyses. The model is based on an underlying finite element model,

which is chosen to be the FE/CM model that used in Chap. 2. The force-deflection function for the system is calculated through a serious of static analyses using the FE/CM model. The static contact configuration at each nominal gear mesh position and applied torque is saved, and used for post-processing. The gears are analyzed dynamically using an analytical model, where the crucial dynamic mesh force is calculated using the force-deflection function. The dynamic response of other quantities, including the tooth root strains and contact stresses, are post-processed from the static FE/CM results and analytical dynamic results. The model is validated against the FE/CM results and available experimental data at multiple speed and torque combinations, including near resonant gear speeds when high amplitude vibrations are excited and contact loss occurs. Both the gear translational and rotational vibrations, and tooth root strains and stresses are compared. The simulation time for the HAC method is five orders of magnitude faster than the FE/CM model with almost no loss of accuracy.

The HAC model is then extended to in plane motions of multi-mesh systems in Chap. 4. The details of how to implement the HAC method to multi-mesh systems is introduced and explained. The force-deflection function for each tooth mesh is generated individually through static FE analyses, and used for the analytical dynamic calculations. A three-gear idler train system and a planetary gear system is used as an example. The gears are analyzed using the HAC method, and validated against FE/CM results. The HAC model is shown to be able to predict load sharing in planetary gears, including those with planet pin position errors.

Chapter 5 investigated the three-dimensional vibrations in helical gear pairs. Similarly,

the force-deflection function is generated statically using the FE/CM model prior to analytical dynamic analysis. The contact configuration at each nominal gear mesh position, applied torque, and twisting angle is calculated, and saved. The generalized force due to contact along each one of the six degree of freedom of the gears are saved. The gears are then analyzed dynamically using a lumped-parameter model. The dynamic results are validated by comparing with the FE/CM calculations. Good agreement is shown between the two models for both the translational and rotational vibrations. The dynamic tooth root strains at different positions along the face-width direction are calculated, and validated against the FE/CM results.

The works in Chaps. 4 and 5 completes the theoretical studies and validations of the HAC model that introduced in Chap. 3. The HAC model can be implemented into any types of gear systems, including compound gear systems, multi-stage planetary gear systems, and system level gear boxes.

Chapter 2

Dynamic Tooth Root Strains and Experimental Correlations in Spur Gear Pairs

2.1 Motivation and Objectives

Gear teeth can fail as a result of dynamic loads causing large tooth root stresses and strains. Understanding and predicting these stresses and strains remains a challenging task for engineers trying to avoid structural failure.

Gear dynamics has been studied for decades using lumped-parameter models, that is, when the gears are modeled as discrete masses and moments of inertia connected by stiffness elements. Özgüven and Houser [4] reviewed mathematical models for gear dynamics prior to 1988. Gear dynamics studies prior to 1996 can be found in the comprehensive bibliography of Ref. [5]. Wang et al. [6] reviewed gear dynamics and vibration with a focus on nonlinear behavior. In an early work, Gregory et al. [7] investigated the vibration of spur gear pairs analytically and experimentally. Blankenship and Singh [8, 9] developed a three-dimensional gear mesh model to study the vibration of helical gears. Velex and Maatar [5] derived a gear

mesh interface model by discretizing the instantaneous lines of tooth contact. Their model includes the effects of tooth surface modifications and errors. Eritenel and Parker [11, 12] investigated nonlinear vibration in helical gears using a three-dimensional lumped-parameter model. Their tooth mesh interface is modeled as a discretized network of stiffnesses that captures total and partial contact loss (where portions of the nominal lines of contact lose contact). Palermo et al. [13] derived a three-dimensional mesh interface model intended for multibody dynamics simulations. Eritenel and Parker [14] derived closed-form solutions for the nonlinear vibration of gear pairs with total and partial contact loss using a perturbation method. Lumped-parameter models, like those cited above, assume the gears are rigid bodies. Tooth root strains are not directly calculated using these models. Dynamic tooth root stresses are calculated in Refs. [22, 23, 24] using analytical expressions for tooth root stresses that depend on dynamic tooth forces from the lumped-parameter model.

A finite element/contact mechanics formulation for the elastic contact between gear teeth has been developed by Vijayakar and co-workers [104, 105, 106]. This formulation can also be used to model the elastic contact of the roller/race interface in rolling element bearings [119]. Parker et al. [107] determined the dynamic response for two-dimensional planetary gears using this formulation. Parker et al. [108] showed the finite element/contact mechanics formulation accurately predicts the vibration in gear pairs compared with experiments, including tooth contact loss and the nonlinear jump-up and jump-down frequencies near resonance. Tamminana et al. [118] used the finite element/contact mechanics model to study the relationship between the dynamic factor and dynamic transmission error for spur gear pairs. Cooley et al. [109] developed a frequency domain finite element method for the

dynamic analysis of three-dimensional gear systems. These works focus on rigid body gear deflections, especially dynamic transmission error and dynamic tooth forces. In contrast, tooth root strains are a focus of the current work.

Tooth root stresses have been studied experimentally using photo-elastic methods for spur gear pairs in Refs. [122, 123] and planetary gears in Ref. [124]. Photo-elastic methods show stress distributions and locations of the maximum stress. Strain gages are used to measure tooth root strains for gear pairs in Refs. [22, 125, 97, 126, 127, 1] and planetary gears in Refs. [132, 133, 130, 128, 129].

Regarding calculation of tooth root stresses and strains, numerous models have been used. Ichimaru and Hirano [22] calculated the static and dynamic tooth root strains in spur gears using an analytical model. Chabert et al. [93] calculated spur gear tooth root stresses using a two-dimensional finite element model of a single tooth with a concentrated load applied to its surface. Oda et al. [94] investigated the static tooth root stresses in thin-rimmed spur gears using a finite element model of only a few teeth with a concentrated load at the tooth surface. Oda et al. [95] used a boundary element method to calculate tooth stresses in thin-rimmed spur gears. Lee et al. [23] investigated the effects of profile modifications on gear tooth root stresses by substituting the dynamic tooth forces calculated from an analytical model into an analytical formula (the Heywood formula) for tooth root stresses. Lin et al. [24] discussed the design of profile modifications to reduce vibration, tooth loads, and root stresses. Bibel et al. [96] calculated the root stresses for thin-rimmed spur gears using a finite element model. They investigated the sensitivity of the stress calculations to the boundary conditions of the model. Baud and Velex [97] analytically

investigated static and dynamic tooth root stresses in gear pairs. Their model agreed with measurements. Wang and Howard [98] calculated the static stresses for high contact ratio spur gears using a conventional finite element method. Kawalec et al. [99] compared the tooth root stresses from a finite element model to ISO and AGMA standards. Thirumurugan and Murthuveerappan [100] investigated the effects of gear parameters on the static tooth stresses in spur gears using a finite element model. Palmer and Fish [101] compared analytical and finite element models for tooth root stresses. The effect of tip relief and involute contact ratio on static tooth root stresses is investigated. Kahraman and Vijayakar [110] calculated the tooth root stresses in planetary gears using a finite element/contact mechanics model. Singh et al. [132] correlated static tooth root and hoop strains calculated from the finite element/contact mechanics formulation with experiments for the ring gears of planetary gears. The finite element/contact mechanics model is used to investigate the effect of ring gear rim thickness on static tooth root and hoop strains in Ref. [133]. None of these studies have focused on the shape of the static and dynamic strain curves, which is a focus of this work.

In this work, we investigate the static and dynamic gear tooth root strains using a finite element/contact mechanics model. Two different unity-ratio gear pairs are studied: a 28-tooth gear pair with asymmetric teeth and a 50-tooth gear pair. The finite element calculations of static and dynamic strains are correlated to experiments for both gear pairs. The correlated finite element models are used to investigate the features of the static and dynamic strain curves. The shapes of the static strain curves are explained using the changing contact conditions on the gear teeth. The effects of tooth profile modifications and strain

gage location on the static strain curves are investigated. The shapes of the dynamic strain curves with three types of contact loss nonlinearities are explained using dynamic contact conditions and dynamic tooth loads. The effects of incomplete tooth contact, defined as one of the two tooth pairs normally in contact losing contact, and total contact loss due to large amplitude vibrations are explained. Even without any form of contact loss, different speeds that have the same amplitude of dynamic transmission error (DTE) can have much different amplitudes of dynamic tooth strain.

2.2 Finite Element/Contact Mechanics Formulation

We use a finite element/contact mechanics formulation to calculate the static and dynamic tooth root strains in spur gear pairs. The formulation is described by Vijayakar and co-workers in Refs. [104, 105, 106] and summarized for gear dynamics applications in Refs. [108, 109]. A concise overview of the contact mechanics model can be found in Ref. [107]. We briefly describe the formulation below.

The finite element/contact mechanics model is built on an underlying multibody dynamics formulation that captures the nominal gear rotation at an operating speed. Each gear body has a finite element mesh for elastic deformations and six rigid body degrees of freedom. Because the gears rotate during the analysis, finite element models of the complete gears are necessary; we do not model only the contacting teeth and a few adjacent teeth, as in Refs. [94, 95, 96, 99, 100]. The tooth surface geometry is defined using special finite elements that precisely define the tooth contact surface with high resolution. These elements

have continuous displacements and slopes due to the use of Hermite polynomial shape functions. Prescribed tooth micro-geometry changes (i.e., tooth profile and lead modifications) are accurately modeled.

The gears rotate kinematically and the contact condition changes continuously. The elastic contact at the gear teeth is captured using a semi-analytical formulation. The contact area on the gear teeth is typically two orders of magnitude less than the tooth dimensions. This allows us to separate the tooth into two regions: an "inner" region near the contact, and an "outer" region away from contact. Near the contact, an analytical solution for a point load on a elastic half-space is used to calculate relative deformations. In the outer region, deformations due to tooth bending and gear blank deformations are calculated using the finite element method. The two solutions are matched along an interface that is sufficiently near the tooth contact surface that the analytical solution remains valid and sufficiently far that the finite element solution is accurate. The near-field analytical contact solution eliminates the need for a highly refined finite element mesh near the tooth surfaces. Only relatively coarse finite element meshes for the gear teeth are necessary. Additionally, the same finite element mesh can be used as the gears move kinematically and the contact moves along the tooth surface. No re-meshing is necessary. Dynamic analyses are possible using this formulation because of its high computational efficiency. Partial contact loss (portions of nominal lines of contact separating), incomplete contact loss (one of two nominal contacting tooth pairs losing contact), and total contact loss that occur for high amplitude vibrations near resonant gear speeds are modeled naturally.

2.3 Experiments

2.3.1 28-Tooth Gear Pair

The static and dynamic tooth root strains for the 28-tooth unity-ratio spur gear pair are measured using a power re-circulating test rig. The input and output gears are identical. A test gear is shown in Fig. 2.1. The teeth have asymmetric profiles. One side has a 20° pressure angle and 1.63 involute contact ratio. The other side has a 25° pressure angle and 1.45 involute contact ratio. The gears have 5 mm module. The outer and root diameters are 149.9 and 126.4 mm, respectively. The circular tooth thickness is 7.64 mm. The root fillet geometry is determined by specifying the edge radius of the tool (hob) that cuts the teeth. The hob tip radius is 0.4 mm. The gears have 9 mm facewidth with 15 μm of lead crowning. The gears have parabolic tooth profile modifications. The 20° pressure angle side has 52 μm of tip relief starting at 22.9° roll angle. The 25° pressure angle side has 47 μm of tip relief starting at 28.54° roll angle. The gears are made of steel with 7.85×10^3 kg/m^3 density and 201.5 GPa Young's modulus. Both gears are mounted on stiff shafts and bearings so that translational and tilting motions of the gears are small compared with the torsional vibrations. Compliant couplings isolate the test gears from the rest of the test rig.

The gear teeth are instrumented with strain gages, as seen in Fig. 2.1. A total of five consecutive teeth are instrumented on each gear of the pair. Strains are measured on both sides of the teeth. The strain gages are placed near the tooth root at 64.465 mm and 64.051 mm from the gear center on the 20° pressure angle and 25° pressure angle sides, respectively. The gear tooth root strains are measured under static and dynamic conditions. For static

(a)

(b)

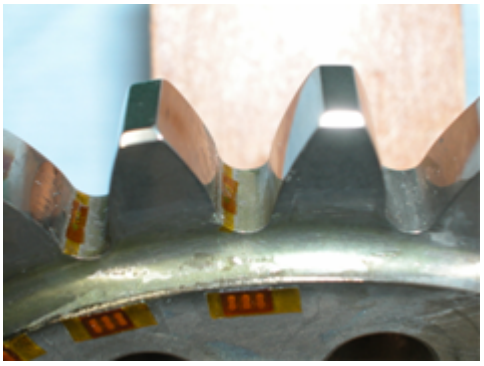

Figure 2.1: Photographs of (a) one 28-tooth spur gear of the gear pair and (b) the tooth root region showing the locations of the strain gages used in the experiments.

conditions the gears rotate at constant torque and a low speed of 70 Hz mesh frequency where dynamics are negligible. To capture dynamic strain measurements the gears are rotated at a number of torque and speed combinations. Steady state dynamic strains are recorded after the transient response has diminished.

2.3.2 50-Tooth Gear Pair

We also correlate our model against dynamic measurements [1] on a 50-tooth unity-ratio spur gear pair mounted in a power-recirculating test rig under static and dynamic conditions. The gears from Ref. [1] have 50 teeth, 20° pressure angle, 3 mm module, and 20 mm facewidth. The input and output gears have 156.06 mm and 156.08 mm outer diameters, respectively. The gear root diameters are 140.95 mm. The involute contact ratio

is 1.8. The circular tooth thickness is 4.64 mm. Experimental results are presented for spur gear pairs with and without tooth profile modifications. The modified gears have 10 μm of linear tip relief starting at 20.9° roll angle. Several teeth are instrumented with strain gages. The strain gages are placed at the facewidth center in the tooth root on the drive side. A Wheatstone bridge was formed by four of the strain gages to minimize system noise. High frequency noise is removed by a low-pass filter. The test stand and gears in Ref. [1] have been used to measure spur gear pair rotational vibrations in Refs. [120, 2, 121] and helical gear pair static strains in Ref. [127].

2.4 Results

2.4.1 Static Tooth Root Strains

Figure 2.2(a) shows the finite element model for the 28-tooth unity-ratio spur gear pair described in Section 2.3.1. The finite element mesh and contact grid resolution are chosen so that the convergence error of the static transmission error is less than 1%. Figure 2.2(b) shows the finite element mesh of a single tooth. The locations of the strain gages in the experiments are shown using thick lines. They are in the tooth root below the start of active profile. Subsequent finite element strain calculations are shown at points along the tooth profile defined by the coordinate S.

Figure 2.3 shows the static tooth root strain for the 28-tooth gear pair at 100 N-m torque with the 25° pressure angle tooth side in contact on the drive (Fig. 2.3(a)) and coast (Fig.

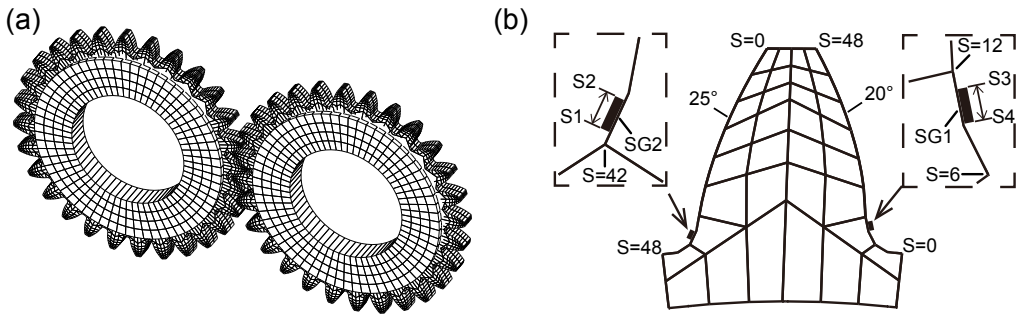

Figure 2.2: (a) Finite element model for the 28-tooth unity-ratio spur gear pair. (b) The finite element mesh of a single asymmetric tooth and the location of the strain gages ($SG1$ and $SG2$). The tooth profile coordinate is defined by S.

2.3(b)) sides. Figure 2.4 shows the static strain on the drive side for the 50-tooth gear pair at 200 N-m torque. The solid red and dashed blue lines denote the experiments and finite element calculations, respectively. Two lines are shown for each finite element calculation, where these correspond to nodal points at the beginning and the end of the strain gage (e.g., $S1$ and $S2$ in Fig. 2.2(b)). The finite element calculation of strain at any location between these two points lies within the grayed region defined by the strains at the top and bottom of the strain gage. The finite element/contact mechanics approach accurately predicts the amplitude and shape of the static strains compared with experiments on both the drive and coast sides, as shown in Figs. 2.3(a) and (b). The drive and coast side strain amplitudes differ, although they have the same general shape. This is due to the different dimensions of the asymmetric gear teeth. For symmetric teeth the strain curves are nearly identical. Excellent correlation is also seen in Fig. 2.4 for the 50-tooth gear pair tooth root strains calculated from the finite element/contact mechanics formulation compared with published experiments [1]. Similar agreement has been observed at other applied torques for both the 28-tooth and 50-tooth gear pairs, which is not shown.

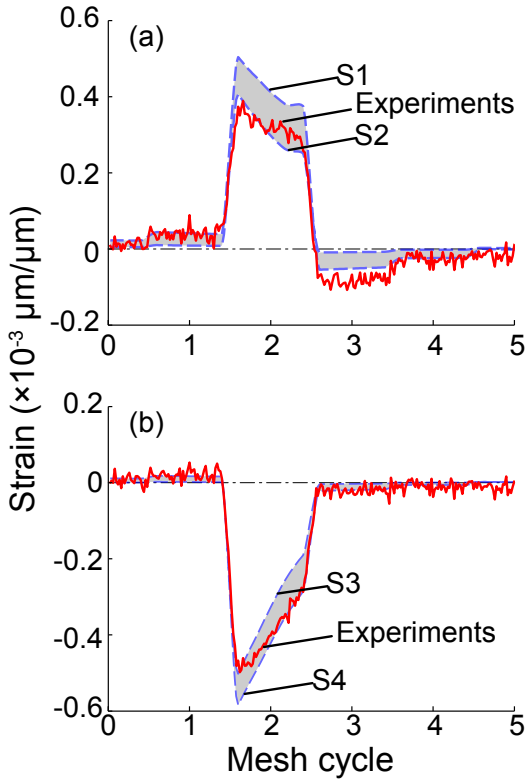

Figure 2.3: Finite element calculation of static strain compared with experiments for the 28-tooth gear pair at 100 N-m torque with the 25° pressure angle tooth side in contact on the (a) drive and (b) coast side. The solid red and dashed blue lines denote the experiments and finite element calculations, respectively. $S1 - S4$ denote points along the tooth profile as shown in Fig. 2.2(b).

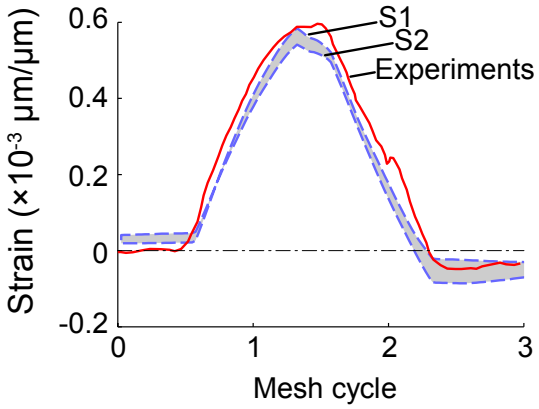

Figure 2.4: Finite element calculation of static strain compared with experiments [1] for the 50-tooth gear pair at 200 N-m torque on the drive side. The solid red and dashed blue lines denote the experiments and finite element calculations, respectively. $S1$ and $S2$ denote the endpoints of the strain gage along the tooth profile.

With these successful experimental correlations, the finite element model can now be used to investigate the features of the static strain curves. Figures 2.5(a,b,c) show the calculated static strain, tooth loads, and average contact locations (S_a) on the tooth surface (in the profile coordinate S shown in Fig. 2.2(b)) for the 28-tooth gear pair with no tooth profile modifications. The same quantities are shown in Figs. 2.5(d,e,f) for modified gear teeth with 47 μm of parabolic tip relief starting at 25° roll angle. For both the unmodified and modified teeth in Fig. 2.5, the applied torque is 300 N-m and the 25° pressure angle tooth side is in contact. The strains are calculated at a point that corresponds to the center of the strain gage SG2 in Fig. 2.2(b). The solid lines in Fig. 2.5 denote the strains calculated on tooth i, and the dashed lines denote the results calculated on the adjacent teeth $i-1$ and $i+1$. The strains for the gear teeth adjacent to those (teeth $i-2$ and $i+2$) and those for all remaining teeth are not shown. The pitch point of each tooth corresponds to the integer values of mesh cycle. The vertical dotted lines denote the following roll angles calculated from the geometry of the corresponding rigid gears: start of active profile (SAP), highest point of single tooth contact (HPSTC), lowest point of single tooth contact (LPSTC), and end of active profile (EAP). These roll angles divide the mesh cycle into regions of single and double tooth contact. The strains in each of these regions differ due to the changing contact conditions on the gear teeth, and these differences are explained subsequently.

Instantaneous static contact conditions for the unmodified 28-tooth gear pair are shown in Fig. 2.6. In region A (Fig. 2.5(a)) the tooth i root strain is small and positive. Tooth i carries no load, as shown in Figs. 2.5(b) and 2.6(a). The adjacent tooth $i-1$ is the only loaded tooth in this region. The elastic deformations of tooth $i-1$ in the direction

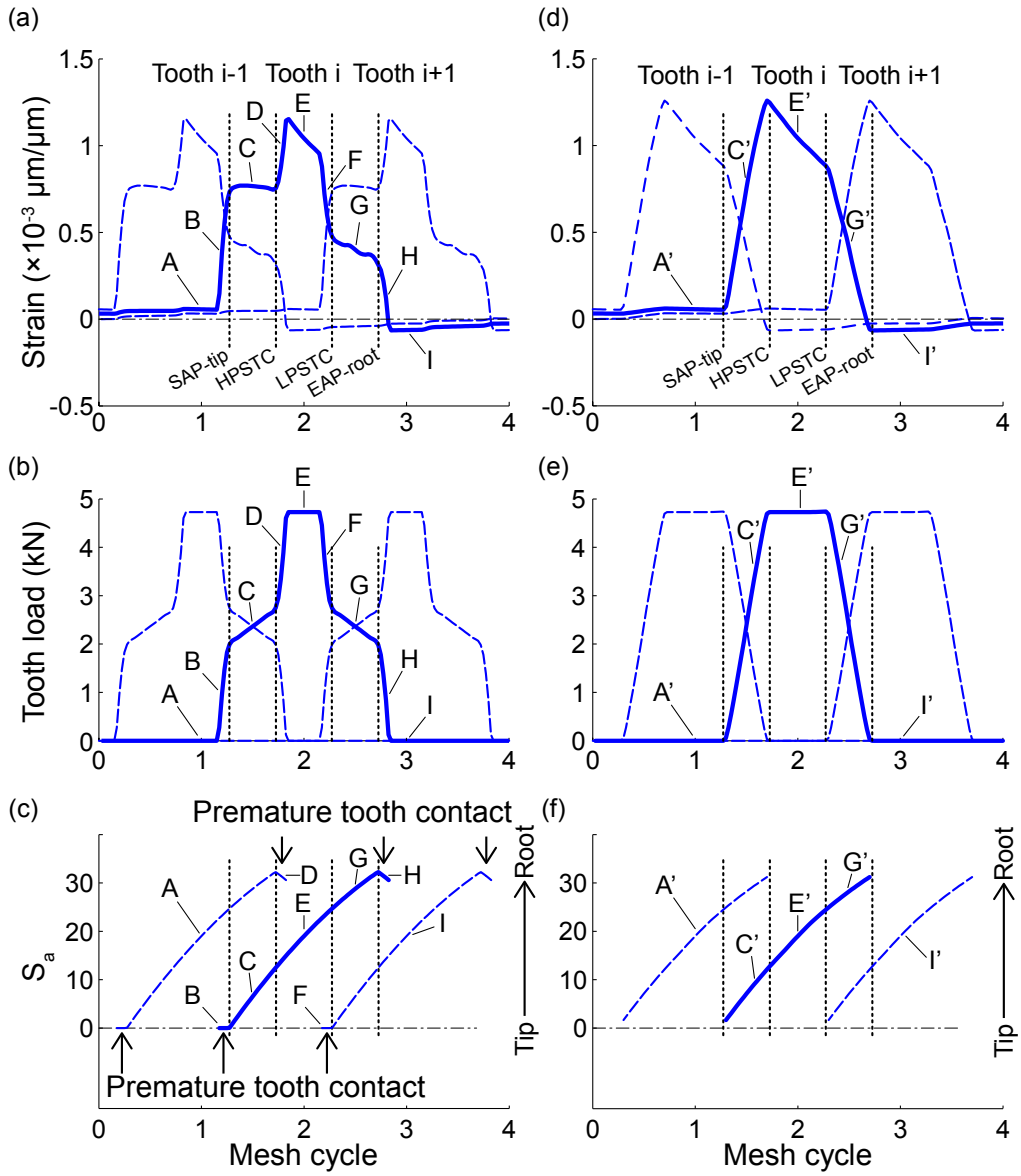

Figure 2.5: Finite element calculation of (a,b) static strain for $S = 40.2$, (c,d) tooth loads, and (e,f) average contact location on the tooth surface (in the profile coordinate S shown in Fig. 2.2(b)) for the 28-tooth gear pair without tooth profile modification (a,c,e) and with 47 μm of parabolic tip relief starting at 28.54° roll angle (b,d,f). The torque is 300 N-m and the 25° pressure angle tooth side is in contact. Only the drive side strains are shown. The vertical lines indicate contact conditions on the output gear.

of gear rotation and the gear blank cause the small tensile strain on tooth i. In region B (Fig. 2.5(a)) immediately prior to the SAP, the strain curve increases rapidly with mesh position. This is due to premature tooth contact of the edge of tooth i on the surface of the mating tooth caused by elastic tooth and gear blank deformations under load, as seen in Fig. 2.6(b). The strain curve in Fig. 2.5(a) is nearly constant in region C. In this region, tooth $i-1$ and tooth i both take load, as seen in Figs. 2.5(b) and 2.6(c). The load on tooth i increases as the mesh cycle increases (Fig. 2.5(b)), and the contact moves from the tooth tip towards the tooth root (Fig. 2.5(c)). The strain is nearly constant due to the interaction of two effects, namely, the increase in tooth load acts to increase strain while the decrease in the distance between the strain gage and the tooth load, which is like a decrease in the bending moment arm, acts to decrease strain. In region D (Fig. 2.5(a)) immediately after the HPSTC, the strain curve has another sudden increase with mesh position. This is due to premature tooth contact on tooth $i-1$ as it leaves the mesh, as seen in Fig. 2.6(d). In region E (Fig. 2.5(a)) the tooth root strain decreases with mesh cycle. The maximum strain occurs at the mesh position immediately after tooth $i-1$ leaves contact. At this point tooth i takes the entire load and the contact location is the farthest away from the strain gage (for single tooth contact). Only tooth i is loaded in region E, as seen in Fig. 2.6(e). The tooth load is constant in this region (Fig. 2.5(b)). The tooth root strain in Fig. 2.5(a) decreases in region E because the contact location moves from the tip toward the tooth root as the mesh cycle increases (Fig. 2.5(c)). In region F (Fig. 2.5(a)) immediately before the LPSTC, the strain curve decreases suddenly with mesh position. Similar to regions B and D, this is due to premature tooth contact, now on tooth $i+1$ as it comes into mesh, as seen in Fig. 2.6(f). In region G (Fig. 2.5(a)) the root strain decreases with mesh position. There are two teeth

in contact, as seen in Figs. 2.5(c) and 2.6(g). The strain curve decreases in region G because the tooth load decreases (Fig. 2.5(b)) and the contact location moves further toward the tooth root (Fig. 2.5(c)) as the gears rotate. The strain in region G is smaller in amplitude than that in region C, which is also a region of double tooth contact. This is mainly due to the contact location in region G being closer to the tooth root (and the strain gage) than that in region C, as shown in Figs. 2.5(c), 2.6(c), and 2.6(g). Loading on the adjacent teeth also contributes to the different strain amplitudes on tooth i in regions C and G, although to a lesser extent. In region C, the load on tooth $i-1$ causes small tensile strains on tooth i. In region G, the load on tooth $i+1$ causes small compressive strains on tooth i. In region H (Fig. 2.5(a)) immediately after the EAP, the strain curve has another sudden decrease with mesh position due to premature tooth contact on tooth i as it exits the mesh (Fig. 2.6(h)). In region I (Fig. 2.5(a)) the root strain is small and negative due to load on tooth $i+1$ causing tooth i to deform in the direction of rotation, as seen in Fig. 2.6(i).

The correlation of tooth root strains to tooth forces and the contact location discussed above occurs for both gear pairs investigated in this study, and likely all gears with contact ratio between one and two provided the strain gage is in the root of the tooth. For contact ratios larger than 1.45 as shown in Fig. 2.5, regions C and G will widen and region A will narrow (with opposite behavior for contact ratios smaller than 1.45). Their shapes will remain unchanged. For high contact ratio gears (contact ratios greater than two) the shape of the strain curve will differ due to the mesh load being distributed differently on the individual gear teeth over the mesh cycle. The relationship between the tooth load and the contact location described in this section remains, however.

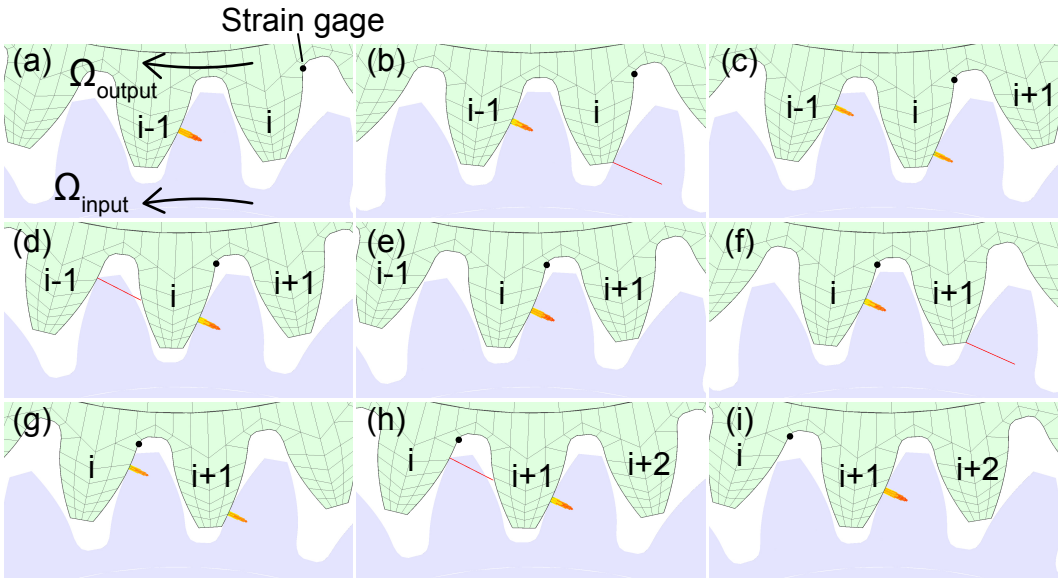

Figure 2.6: Instantaneous contact conditions labeled in Fig. 2.5(a) for the 28-tooth gear without tooth profile modification. The static strains for the sub-figures (a-i) are labeled as (A-I) in Fig. 2.5(a). The strain gage on tooth i of the output gear is labeled by a black circle.

The preceding discussion described the strain curve on the output (driven) gear. The strain on the input (driving) gear has nearly the same shape (because the gears are identical) except that it is reflected about a vertical axis at mesh cycle equal to one. For two non-identical gears in mesh the input and output strain curves will have the same A-I regions, but the amplitudes will differ because the gear tooth dimensions differ.

Figure 2.5(d) shows the static tooth root strains for the 28-tooth gear pair with tooth profile modifications. They differ sharply from the strains in Fig. 2.5(a) for unmodified gear teeth. This is due to the removal of premature tooth contact (regions B, D, F, and H in Fig. 2.5(a)) by tooth profile modifications. For tip relief of less than 47 μm the premature tooth contact may not be completely removed. There are no sudden changes in the strain or tooth load in Figs. 2.5(e) and (f). The static contact conditions for the remaining regions A', C', E', G', and I' in Fig. 2.5(d) are similar to that shown in Figs. 2.6(a,c,e,g,i) for

unmodified gears. Unlike the nearly constant strain in region C (Fig. 2.5(a)) for unmodified teeth, the strain in region C' (Fig. 2.5(d)) increases. This is because of the different way a tooth is loaded when the teeth have modifications. For unmodified teeth the load on the tooth is abrupt immediately before and after region C due to premature tooth contact. With modifications, premature contact does not occur. The tooth is more gradually loaded from no load to maximum load at a nearly constant rate. Therefore, the strain also gradually increases in this region. Similarly, the strains in region G' (Fig. 2.5(d)) decrease gradually as the tooth unloads. The difference in the maximum strain in regions C' and G', which have the same maximum tooth load, is due to the difference in where along the profile that the tooth load occurs (Fig. 2.5(f)). Because the premature tooth contact is removed, the maximum load now occurs higher along the tooth surface, so the maximum strain for the gears with tooth profile modifications is larger than when the teeth are unmodified, as seen by comparing Figs. 2.5(a) and (d) near the HPSTC. Although profile modifications increase tooth root strains, and hence root stresses, they are still essential to limiting the high contact stresses during premature contact that cause tooth surface wear and failure.

Figure 2.7(a) shows the finite element calculation of tooth root strain for the 28-tooth gear pair with tooth profile modifications over multiple mesh cycles for a wide range of strain gage locations. The tooth root strains in Fig. 2.5(d) are from $S = 40.2$ in Fig. 2.7(a). As seen in Fig. 2.7(a) the maximum strain occurs near mesh cycle 1.7 (immediately after the HPSTC when only one tooth carriers the load) near the middle of the tooth root region at $S = 41.6$. The tooth root strain varies sharply with root location S in the regions $34 < S < 41.6$ and $41.6 < S < 45$ immediately before and after the maximum strain location. This strain

sensitivity to the location S leads to meaningful changes in amplitude for small differences along the tooth profile. It explains the width of the strain gage as shown by the grayed region between the two dashed blue lines in Figs. 2.3 and 2.4. Although the strain curves at a given strain gage location S vary in amplitude throughout $34 < S < 45$, their general shape and features over a mesh cycle are the same as those discussed previously for $S = 40.2$ shown in Fig. 2.5(b). At strain gage locations of $S > 45$ in Fig. 2.7(a), however, some features change as a result of the strain being calculated in the tooth fillet region. As seen in the figure, the strain between the 1.7 and 2.3 mesh cycle configurations, when only one tooth is in contact and has constant load, is nearly constant. For $34 < S < 45$, the strain decreases in this region as a result of the contact location moving along the tooth surface toward the root. In the fillet region ($45 < S < 48$) the calculated strain is due to elastic gear blank deformation that depends on the total load on the tooth but only weakly on the location along the tooth surface where that load is applied. In contrast, the strain in the root region ($34 < S < 45$) is largely due to gear tooth bending deformation; it is highly dependent on the location of the tooth load, as mentioned previously. For $S > 44$ there are meaningful strains when the gear teeth are not loaded, that is, before mesh cycle 1.3 and after mesh cycle 2.3 in Fig. 2.7. Prior to tooth entering contact, the fillet strain is positive and increases monotonically with mesh cycle as the preceding teeth come into contact. After the tooth leaves the mesh the fillet strain is negative and increases monotonically as the subsequent teeth come into contact. These strains result from deformation of the gear blank. The strains further up the tooth past $S = 42$ nearly vanish when the tooth with the strain gage is unloaded.

The calculated tooth strain is shown in Fig. 2.7(b) for the maximum hob tip radius (1.8

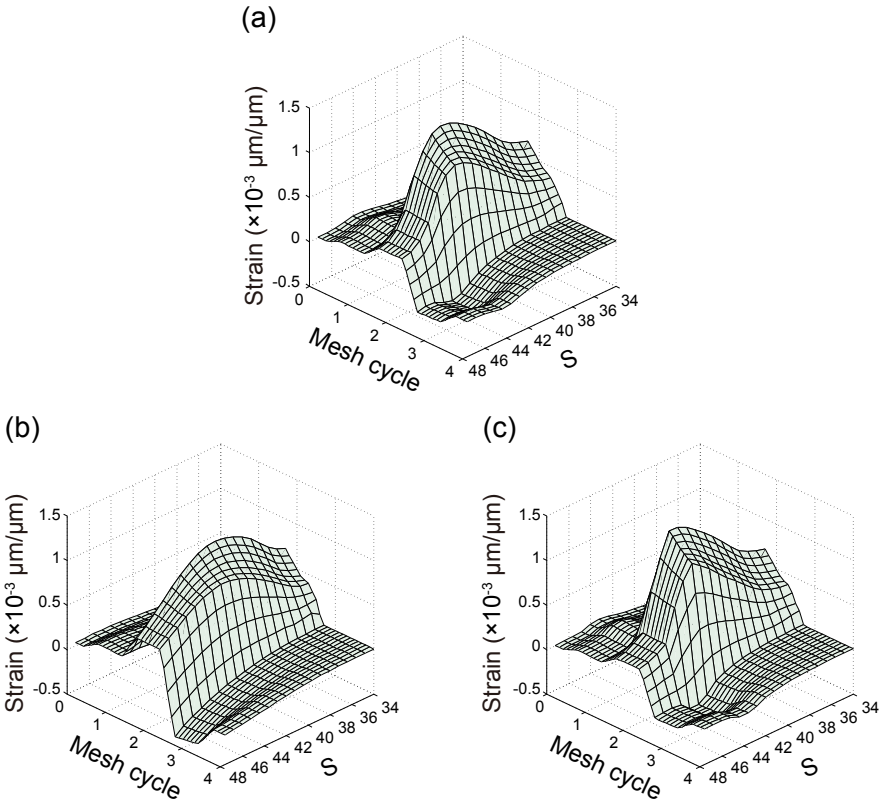

Figure 2.7: Finite element calculation of static strain for varying locations in the tooth root-fillet region for the 28-tooth gear pair with tooth profile modifications at 300 N-m torque with the 25° pressure angle tooth side in contact. The hob tip radius is (a) 0.4 mm (nominal), (b) 1.8 mm (maximum), and 0.01 mm (nearly vanishing), respectively. The tooth profile coordinate S for normal hob tip radius is shown in Fig. 2.2(b).

mm) allowed by geometry and Fig. 2.7(c) for nearly vanishing hob tip radius (0.01 mm). For the maximum hob tip radius in Fig. 2.7(b) the maximum tooth root strain decreases (13.2% smaller), as expected, and the strain sensitivity to root location decreases as compared to the nominal case in Fig. 2.7(a). For the nearly vanishing hob tip radius in Fig. 2.7(c) the maximum strain is 10.0% larger than for the nominal case in Fig. 2.7(a). Additionally, the sensitivity of the strain to the root location immediately before and after the maximum is larger than that for the nominal case in Fig. 2.7(a). The tooth fillet region is larger for this lower hob tip radius case compared with the nominal case, so there is an expanded region where the strain curves have the features of the fillet region.

2.4.2 Dynamic Tooth Root Strains

The finite element/contact mechanics models are applied below to predict dynamic tooth root strains, which are drastically different than that in static conditions due to resonances and contact loss nonlinearities. Correlations with experiments for strongly nonlinear vibrations are given.

The system natural frequencies are determined at nominal load and a chosen position in the mesh cycle by applying torque impulses to the gears and analyzing the resulting transients. For spur gears two such analyses are required: one for single tooth and one for double tooth contact. The natural frequency of the 50-tooth model of 170 N-m torque is 2900 Hz, within 5% of the experimentally reported natural frequency of 2750 Hz [2]. The natural frequencies of the 28-tooth gear pair at 150 N-m torque with the 25° pressure angle side in contact and 300 N-m torque with 20° pressure angle side are 2550 Hz and 2835 Hz,

respectively.

The gear pairs are dynamically analyzed at specified torque and speed combinations to validate the model with dynamic experiments. The gears are analyzed for a number of mesh cycles so that transient response diminishes and only steady state response is recorded. The dynamic tooth root strains for the 28-tooth gear pair (25° pressure angle side in contact) at $f_m/f_n = 1.098$ and 150 N-m torque are shown in Figs. 2.8(a) and (b) for the drive and coast sides, respectively. The model accurately predicts the amplitude and shape of the strain compared with experimental results for the entire duration shown, and this agreement is achieved at a speed close to resonance. Similar correlation is seen in Figs. 2.8(c) and (d) for the 20° pressure angle tooth side in contact at $f_m/f_n = 0.494$ and 300 N-m torque, which have much different amplitude and shape than Figs. 2.9(a) and (b). This is also near a resonant speed caused by the second harmonic of mesh frequency.

Excellent agreement also occurs for the 50-tooth gear pair at $f_m/f_n = 0.986$ and $f_m/f_n = 0.545$ at 200 N-m (Fig. 2.9), both of which are near-resonant speeds. Similar agreement between the finite element model and experiments has been observed at other torques and speeds for both gear pairs, which is not shown.

In addition to tooth root strains, we compare experimental and finite element calculations of dynamic transmission error $DTE = r_{b1}\theta_1 + r_{b2}\theta_2$, where $r_{b1,b2}$ are the gear base radii and $\theta_{1,2}$ are the gear body rotations. Figure 2.10 compares the finite element calculation of the root mean square (RMS) of oscillating dynamic transmission error for the 50-tooth gear pair at 200 N-m torque (circles) with experiments from Ref. [1] (squares). In addition to the usual resonance at $f_m/f_n = 1$, resonances near $f_m/f_n = 1/2$ and $f_m/f_n = 1/3$ occur in

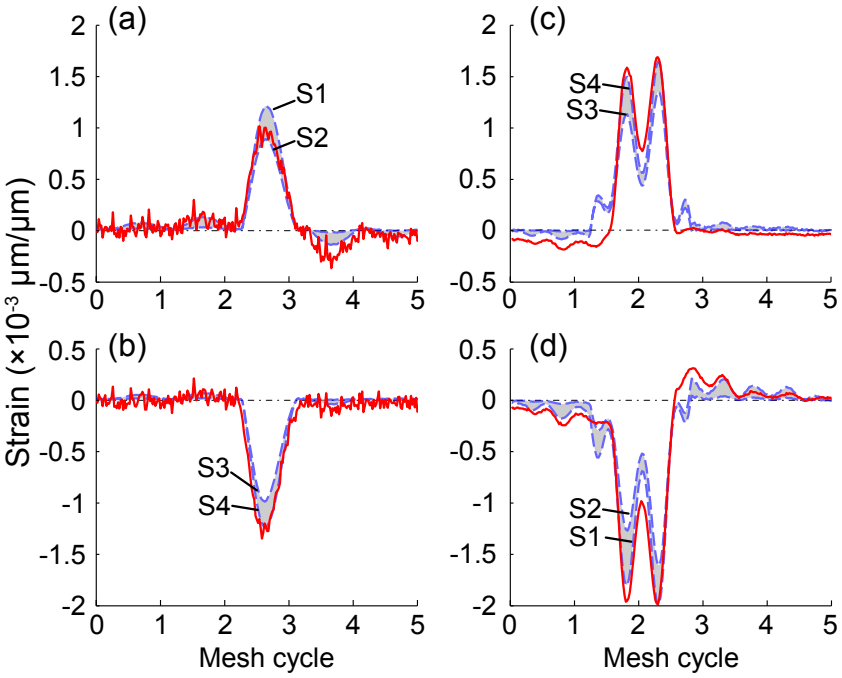

Figure 2.8: Finite element calculation of dynamic tooth root strain (dashed blue lines) compared with experiments (solid red lines) for the 28-tooth gear pair with tooth profile modifications at $f_m/f_n = 1.098$ with 150 N-m torque and the 25° pressure angle tooth side in contact on the (a) drive and (b) coast side, and at $f_m/f_n = 0.494$ with 300 N-m torque and the 20° pressure angle tooth side in contact on the (c) drive and (d) coast side.

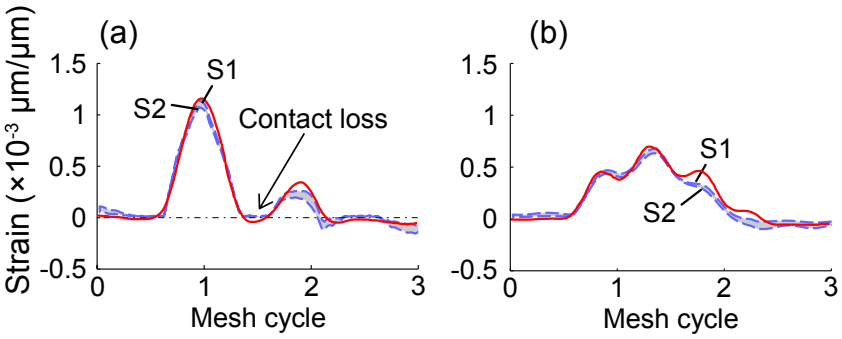

Figure 2.9: Finite element calculation of dynamic tooth root strain (dashed blue lines) compared with experiments (solid red lines) for the 50-tooth gear pair with tooth profile modifications at 200 N-m torque on the drive side. The gear speeds are (a) $f_m/f_n = 0.986$ and (b) $f_m/f_n = 0.545$.

the simulations and experiments due to higher harmonics of mesh excitation coinciding with the natural frequency. The RMS of dynamic transmission error at both resonant and non-resonant speeds are accurately predicted by the model. Similar agreement was found in Refs. [108, 118] for two-dimensional spur gear pair models and Ref. [109] for three-dimensional spur gear pair finite element models. The resonance at f_m/f_n=1 has obvious softening behavior due to large amplitude vibration causing gear teeth that are normally in contact to lose contact.

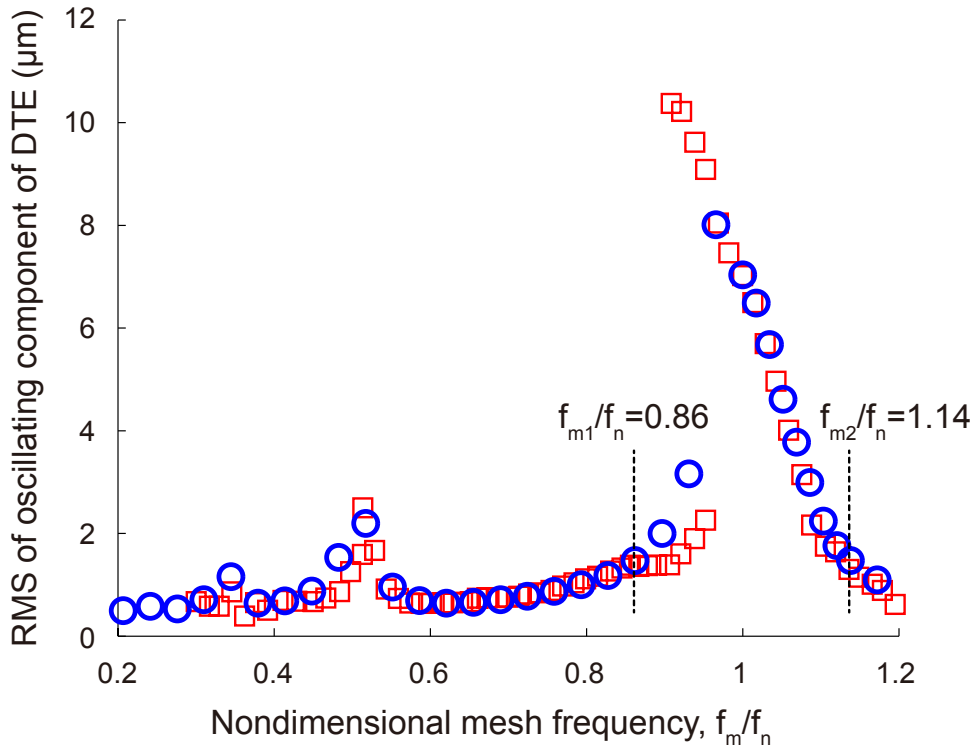

Figure 2.10: Finite element calculation of root mean square (RMS) of oscillating component of dynamic transmission error for the 50-tooth gear pair with tooth profile modifications at 200 N-m compared with experiments from Ref. [1]. The blue circles and red squares denote the finite element calculations and experiments, respectively.

The gears have smaller amplitude vibration at speeds away from resonance. The dynamic strain curves at these off-resonant gear speeds have similar shapes as those from static

calculations, like in Figs 2.3, 2.4, and 2.5(a) and (b). Of course, the dynamic strain curves generally have higher peak amplitudes, which is discussed in Refs. [22, 122, 125, 97, 1], for example. Near resonant gear speeds, however, the strain curves have sharp differences due to large amplitude vibration. At resonances due to higher harmonics of excitation (like near $f_m/f_n \approx 1/2$ in Fig. 2.10) the strain curves have multiple peaks during a mesh cycle, as described in [1]. For example, the strain curves in Figs. 2.8(c), (d), and 2.9 (b) have two peaks during an oscillation cycle because the mesh frequency is near one half of the system's natural frequency.

Some dynamic response amplitudes can be so large that tooth contact loss occurs. We have observed three types of contact loss nonlinearities: incomplete tooth contact, total contact loss, and tooth skipping. The shape of the dynamic strain curves for each type of contact loss are explained subsequently using the dynamic tooth forces and average contact locations.

Figure 2.11 shows the finite element calculation of dynamic tooth root strains, dynamic tooth loads, and average contact locations on the tooth surface (in the profile coordinate S) for the 50-tooth gear pair at 200 N-m torque. The vertical dotted lines denote the SAP, HPSTC, LPSTC, and EAP calculated from the geometry of the corresponding rigid gears, like in Fig. 2.5 for static conditions. Figure 2.11(a) shows the dynamic strain curve at $f_m/f_n = 1.069$ when incomplete tooth contact occurs, that is, one of the two tooth pairs normally in contact loses contact for part of its mesh cycle. Between mesh cycle 1.115 and 1.375, only tooth $i-1$ takes load while the load on tooth i vanishes (Fig. 2.11(b)). In static conditions (and dynamic conditions away from resonance, not shown) this region normally

has two pairs of teeth in contact, like that shown in Fig. 2.5(c). At this speed the vibration of the gears delays the start of contact for the second tooth pair until well after the SAP, leading to small strains in this region. Additionally, the contact begins at $S_a = 6$ (Fig. 2.11(c)), while it begins further up at the tooth tip ($S_a = 0$) for static conditions (Fig. 2.5(c)). Similarly, incomplete tooth contact occurs between mesh cycles 2.115 and 2.375. The tooth i root strain is relatively small in this region (Fig. 2.11(a)), which is due to a small tooth load (Fig. 2.11(b)). The maximum strain, however, is about 50% larger than the corresponding static value in Fig. 2.4.

Figure 2.11(d) shows the dynamic strain curve at $f_m/f_n = 1$ when total contact loss occurs, that is, when the vibration amplitude is so large the gear teeth completely separate. None of the gear teeth are taking load between mesh cycles 1.25 and 1.45, and mesh cycles 2.25 and 2.45, as shown in Fig. 2.11(e). As a result, the dynamic strain (Fig. 2.11(d)) nearly vanishes in these regions. This strongly nonlinear behavior at resonance is accurately captured by the finite element model correlation, as shown in Fig. 2.9(a). The maximum strain for total contact loss (Fig. 2.11(d)) is about twice as large as the corresponding static value.

Figure 2.12 shows the finite element dynamic tooth root strains for the 28-tooth gear pair at 100 N-m torque with 20° pressure angle tooth side in contact. The gear speeds are at $f_m/f_n = 1.7$ in the nonlinear resonance region near $2f_n$. The dynamic tooth root strains on teeth $i-1$ (solid blue line) and $i+1$ (solid black line) have similar shapes as each other with substantially larger peak amplitudes compared with the static strain curve at the same torque. The striking feature is that the dynamic root strain on tooth i (solid red

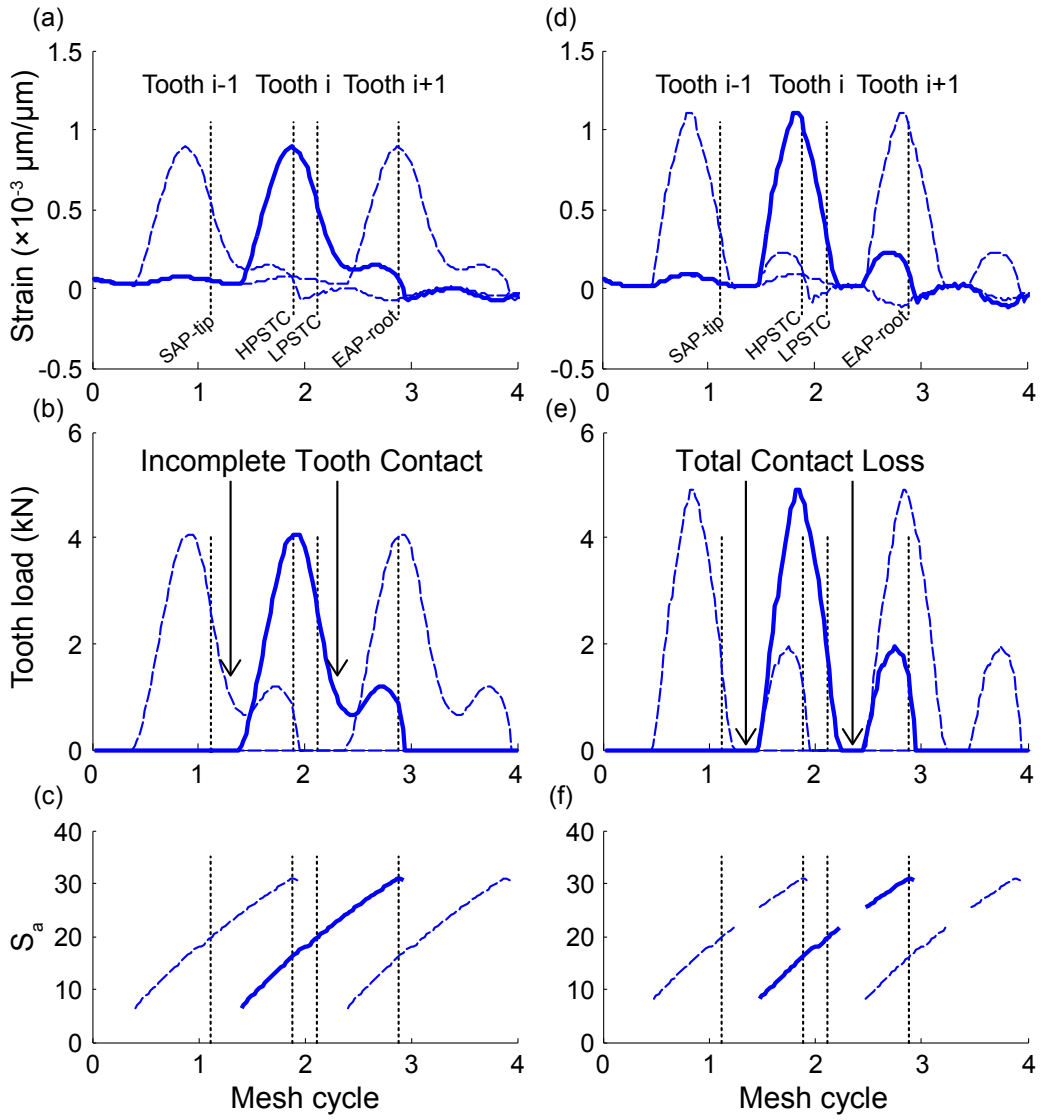

Figure 2.11: Finite element calculation of (a,d) dynamic strain, (b,e) tooth load, and (c,f) contact location on the tooth surface (in the profile coordinate S) for the 50-tooth gear pair with tooth profile modifications at 200 N-m torque. The gear speeds are (a,b,c) $f_m/f_n = 1.069$ and (d,e,f) $f_m/f_n = 1$. Only the drive side strains are shown. The vertical lines indicate contact conditions on the output gear.

line) nearly vanishes for the entire time duration shown. The absence of tooth strain near mesh cycle 2 is due to such large dynamic response that tooth i never takes load; this tooth is completely skipped during the mesh cycle. In static and off-resonant dynamic conditions tooth i normally comes into contact near mesh cycle 1.3. The dynamic strains occur for every other tooth rather than on every tooth, and the peak amplitude for the dynamic strain is almost three times larger than that for the static strain at the same torque.

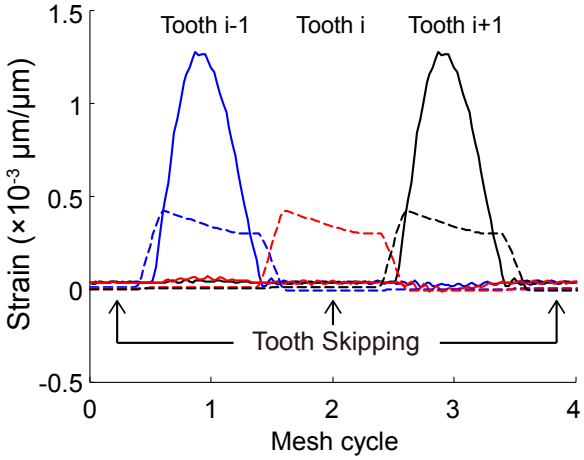

Figure 2.12: Finite element calculation of dynamic tooth root strains for the 28-tooth gear pair with tooth profile modifications at $f_m/f_n = 1.7$ and 100 N-m torque with 20° pressure angle tooth side in contact. The strains are calculated on the drive side of tooth $i-1$ (solid blue line), tooth i (solid red line), and tooth $i+1$ (solid black line). The dashed lines denote the corresponding static strain curves at the same torque.

The ratio of the maximum dynamic strain to the maximum static strain k_d, which could be used as a dynamic factor in practice, is large when any one of the three types of contact loss nonlinearities occurs. When incomplete tooth contact occurs, the value of k_d is around 1.5, as can be found by comparing Fig. 2.11(a) and Fig. 2.4. When total contact loss occurs, the value of k_d is around 2, as can be found by comparing Fig. 2.11(d) and Fig. 2.4. When tooth skipping occurs, k_d can be as high as 3, as shown in Fig. 2.12.

The dynamic transmission error and tooth root strains are not directly correlated. The

same system can have two operating conditions that give the same amplitude of dynamic transmission error but substantially different dynamic strains. This phenomenon is especially evident for two different speeds, one above a resonant gear speed and another below it. Figure 2.13(a) shows the finite element calculation of dynamic tooth root strains for the 50-tooth gear pair at 200 N-m torque at speeds $f_{m1}/f_n = 0.86$ and $f_{m2}/f_n = 1.14$ below and above the resonant speed $f_m/f_n = 1$. At these speeds the gears have nearly the same RMS of DTE, as shown in Fig. 2.10. The strains, however, differ substantially in both amplitude and shape (Fig. 2.13(a)). The dynamic strain curve for f_{m2} is narrower with a 34% larger peak amplitude compared with that for f_{m1}. The DTE for the same two speeds are shown in Fig. 2.13(b). The DTE amplitudes are nearly identical, but they differ by a phase shift. This phase shift causes the shape and amplitude differences between the two dynamic strain curves in Fig. 2.13(a). At f_{m2} above the natural frequency, large DTE occurs near mesh cycle 2 that corresponds to single tooth contact (Fig. 2.13(b)) . The gears experience large load due to large DTE, and there is only one gear tooth taking load (note vertical lines on Fig. 2.13(b)). The dynamic strain is therefore large (Fig. 2.13(a)). At the same gear speed, small DTE occurs near mesh cycles 1.5 and 2.5 that correspond to double tooth contact (Fig. 2.13(b)). The mesh force is small in these regions due to small deflections. Additionally, there are two gear teeth taking load. As a result, the dynamic tooth root strain is small, as shown in Fig. 2.13(a). The strain curve at f_{m2} is narrow with a large peak amplitude due to the effects discussed above. At f_{m1}, however, the DTE is out of phase with that for f_{m2} (Fig. 2.13(b)). Small DTE occurs near mesh cycle 2 for single tooth contact. The mesh force is small due to the small deflections. As a result, the dynamic strain is small even though the mesh force is taken by only one pair of contacting teeth (Fig. 2.13(a)). Large DTE occurs

near mesh cycle 1.5 and 2.5 for double tooth contact. Although the gears have large mesh force due to large deflections, the load is taken by two pairs of teeth. Thus, the dynamic strain is small in these regions. As a result,the strain curve at f_{m1} is wider with a smaller peak amplitude compared with that for f_{m2}.

2.5 Conclusions

This work investigates the static and dynamic tooth root strains in spur gear pairs using a finite element/contact mechanics approach. Two different unity-ratio gear pairs are analyzed. The finite element model is first validated against experimental data for both gear pairs, including both tooth strain and dynamic transmission error comparisons. Excellent agreement is shown for both gear pairs over a range of torques and speeds, including resonant conditions. The shapes and amplitudes of the static and dynamic strain curves for the drive and coast sides closely match the experiments.

Explanations are provided for how the shape of the static strain curve depends on the instantaneous tooth contact conditions. Tooth profile modifications can drastically affect the shape of the static strain curve due to the removal of premature tooth contact. Nevertheless, the maximum tooth root strain is larger for modified teeth. The static strain is sensitive to the strain gage location near the tooth root, and this effect is quantified. Additionally, the static strain curve is affected by the hob tip radius, which controls the geometry of the tooth root.

The shape of the dynamic strain curve depends on the dynamic contact conditions and dynamic tooth loads, especially near resonances when high amplitude vibrations are excited and the gear teeth lose contact. Distinct dynamic strain curves for three types of contact loss nonlinearity are observed: incomplete tooth contact (only one pair of teeth losing contact when two pairs are nominally in contact), total contact loss for a portion of the mesh cycle, and tooth skipping. The gears experience a much larger maximum dynamic strain

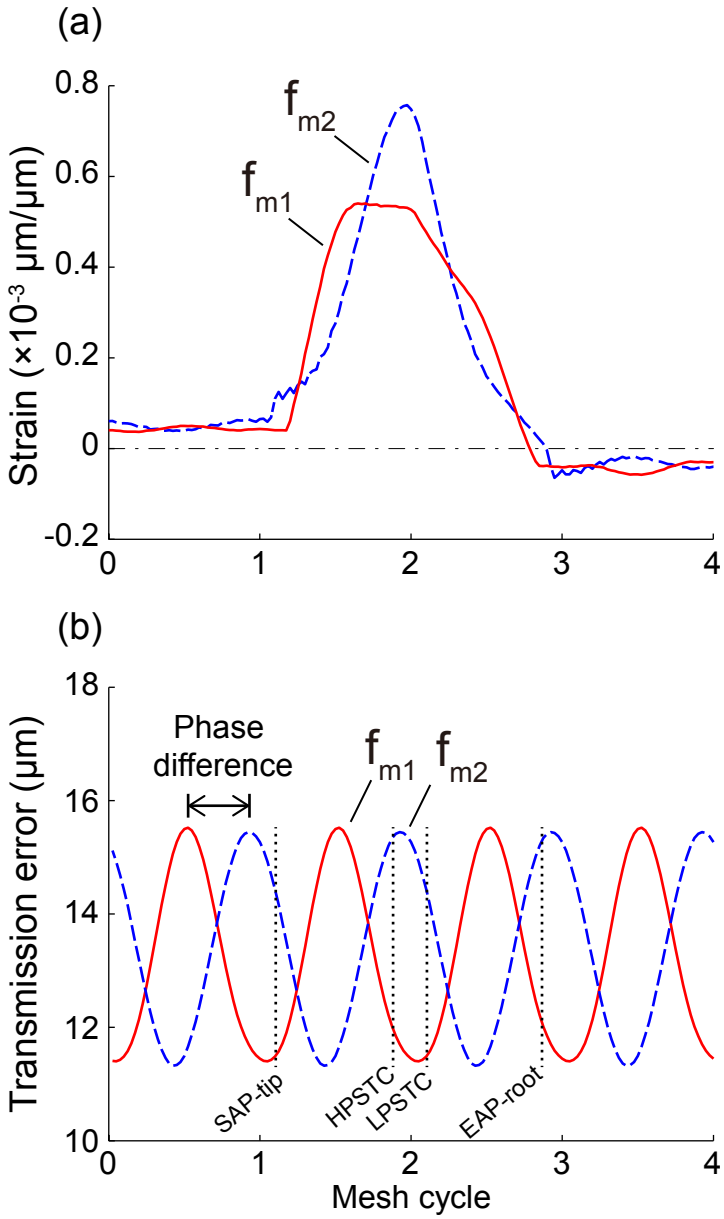

Figure 2.13: Finite element calculation of (a) dynamic tooth root strains ($S = 42.77$) and (b) DTE for the 50-tooth gear pair with tooth profile modifications at 200 N-m torque, $f_{m1}/f_n = 0.86$ (solid red lines) and $f_{m2}/f_n = 1.14$ (dashed blue lines). The vertical lines indicate contact conditions on the output gear.

compared with the corresponding static value when any one of the three types of contact loss nonlinearities occurs.

The dynamic transmission error and tooth root strains are not directly correlated. The shape and peak amplitude of the dynamic strain curves at speeds above and below resonances having the same RMS of DTE may differ. This is due to the phase shift of DTE across resonances.

Chapter 3

An Efficient Hybrid Analytical-Computational Method for Nonlinear Spur Gear Dynamics

3.1 Motivation and Objectives

Gear vibrations are directly related to noise in power transmission systems. System failures result from dynamic loads causing large stresses and strains in the elastic gear teeth. These effects are especially significant near resonant gear speeds when high amplitude vibrations are excited and contact loss nonlinearities occur. Reliable, fast, and accurate models for nonlinear gear dynamics are necessary.

Although gears have been studied for decades, few models can accurately and efficiently predict their nonlinear dynamic response. Conventional finite element models are usually not built for gear dynamic analyses as they are computationally inefficient when solving contact problems. Lumped-parameter models represent the elastic gear tooth mesh using stiffness elements, and this idealization sacrifices accuracy. Lumped-parameter models also have limited ability to model micrometer-level tooth surface modifications that are used in

virtually all gears. Because these models assume the gear bodies to be rigid, the elastic deformations and stresses in the gear teeth are not calculated.

The hybrid analytical-computational (HAC) method merges features of analytical and computational models to accurately and efficiently predict the nonlinear dynamic response in spur gear pairs, including elastic deformations of the gear teeth, stresses, and tooth surface modifications. The proposed method dynamically analyzes a lumped-parameter model where the tooth contact forces at each instant of numerical integration are obtained from a force-deflection function built in advance using static analyses of a computational model. The force-deflection function, defined as the relationship between the gear mesh force and its corresponding mesh deflection at each nominal gear mesh position, is generated through a series of static analyses using a finite element/contact mechanics (FE/CM) model. Other finite element or computational methods could be used for these static analyses. The effects of tooth profile and lead modifications are included in the force-deflection function; there is no additional procedure to incorporate them during the dynamic analysis. In addition to the gear translational and rotational vibrations, elastic deformations in the gear teeth, including the tooth root strains and contact stresses, are accurately predicted. The calculated dynamic response outputs correlate well to finite element calculations and available experiments, including near resonant gear speeds when high amplitude vibrations are excited and contact loss occurs. The simulation time for the HAC model is five orders of magnitude lower than the FE/CM model.

Lumped-parameter models are widely used in gear dynamic analyses. These models assume that the gear bodies are rigid and connected by discrete stiffness elements that rep-

resent the gear teeth. Mathematical models for gear dynamics prior to 1995 can be found in Refs. [4, 5]. More recent studies are found in Ref. [6], which is focused on nonlinear vibration in gears. In an early work, Gregory et al. [7] investigated the vibration of spur gear pairs using a lumped-parameter model. Blankenship and Singh [8, 9] studied the vibration in helical gears using a linear, three-dimensional gear mesh model. Velex and Maatar [5] developed a gear mesh interface model by including distributed mesh stiffnesses along the instantaneous lines of tooth contact. Velex and Ajmi [10] modeled excitations in geared systems using transmission errors. Their model includes the effects of tooth surface deviations caused by tooth modifications and errors. Eritenel and Parker [11, 12] developed a three-dimensional nonlinear tooth contact model using a discretized stiffness network. They examined the nonlinear vibration in gear pairs that result of partial contact loss (where portions of the nominal lines of contact lose contact) and total contact loss. Eritenel and Parker [14] derived closed-form solutions for the nonlinear rotational vibrations in spur gear pairs near their primary resonance using a perturbation method. Liu and Parker [35] investigated the nonlinear dynamics in idler gear systems. The mesh stiffnesses of adjacent teeth are calculated individually in that work. Lumped-parameter models that calculate gear translational and rotational vibrations are also used in commercial codes for gear dynamics. The elastic deformations in the gear teeth, including tooth root strains and contact stresses, are not directly calculated from these models. Those quantities are calculated in Refs. [22, 23, 24] using analytical formulations that depend on dynamic tooth loads from the lumped-parameter models.

Conventional finite element methods are used to calculate gear tooth root stresses and

strains in Refs. [93, 94, 95, 96, 97, 98, 99, 100, 101] and tooth contact stresses in Refs. [102, 103], for example. These studies focus on static conditions. Because of the small contact zone and necessary high precision defining the tooth geometry, a highly refined finite element mesh is required near the tooth contact region for conventional finite element models. Additionally, the contact location moves along the tooth surface as the gears rotate kinematically. Therefore, the finite element mesh needs to be regenerated for each time step or the entire tooth surface requires a highly refined mesh. Either option is computationally inefficient. As a result, most conventional finite element codes are not built for gear dynamic analyses. Furthermore, they normally lack multibody dynamics capability, which is necessary to capture kinematic gear motion.

A finite element/contact mechanics (FE/CM) formulation for contact problems in multibody dynamics is developed by Vijayakar and co-workers [104, 105, 106] and implemented in the software Calyx. Parker et al. [108] investigated the nonlinear dynamic response in spur gear pairs using this FE/CM model. The model accurately predicted the vibration compared with published experiments, including the tooth contact loss and nonlinear jump-up and jump-down frequencies near resonances. Tamminana et al. [118] investigated the relationship between dynamic factors defined by transmission error, mesh force, and tooth root strains calculated from the same finite element code. Cooley et al. [109] calculated the three-dimensional vibration in spur and helical gear pairs using a frequency domain method based on the FE/CM formulation. Dai et al. [135] investigated features of the static and dynamic tooth root strains in spur gear pairs using the FE/CM model. The model is shown to accurately predict gear tooth root strains compared with available experiments, including

near resonant gear speeds when high amplitude vibrations are excited and contact loss occurs. The FE/CM model is also used in studies of planetary gears [107, 110, 132, 65, 51, 133] and rolling element bearings [119].

Gears have been studied for decades in static and dynamic experiments. Gear rotational vibrations are investigated experimentally in Refs. [5, 7, 120, 2, 121]. Gear tooth root stresses and strains are studied using photo-elastic [122, 124, 123] and strain gage measurements [22, 97, 132, 133, 125, 128, 129, 130, 126, 127, 1]. The dynamic tooth contact stresses in gears are not directly measured in experiments.

3.2 Hybrid Analytical-Computational Method

3.2.1 System Parameters and Mathematical Modeling

Three pairs of spur gears are studied in this work: two 50-tooth gear pairs with different involute contact ratios (ICRs) and one 28-tooth gear pair. The 50-tooth gears are studied experimentally in Refs. [120, 2, 121, 1]. The same gears are studied using a finite element/contact mechanics model in Refs. [108, 109, 135]. The static and dynamic tooth root strains for the 28-tooth gears are studied in Ref. [135]. The 28-tooth gears have asymmetric teeth due to the use of different pressure angles on each side. The 50-tooth gears have symmetric teeth. The gear parameters are shown in Tables 3.1, 3.2, and 3.3. More details about the gears can be found in the references.

Figure 3.1 shows a schematic of the 28-tooth gear pair system. The system has four

Table 3.1: Parameters for the 50-tooth gear pair with ICR 1.37

Number of Teeth	50
Module (mm)	3
Pressure Angle (deg)	20
Outer Diameter (mm)	154.41/154.71
Root Diameter (mm)	140.68
Circular Tooth Thickness (mm)	4.64
Face Width (mm)	20
Tooth Profile Modification	None
Density (kg/m^3)	7.595×10^3
Young's Modulus (GPa)	201.17

Table 3.2: Parameters for the 50-tooth gear pair with ICR 1.8

Number of Teeth	50
Module (mm)	3
Pressure Angle (deg)	20
Outer Diameter (mm)	156.06/156.08
Root Diameter (mm)	140.68
Circular Tooth Thickness (mm)	4.64
Face Width (mm)	20
Tooth Profile Modification	Linear
Tip Relief (μm)	10
Start Roll Angle (deg)	22.9
Density (kg/m^3)	7.595×10^3
Young's Modulus (GPa)	201.17

Table 3.3: Parameters for the 28-tooth gear pair with asymmetric teeth

Number of Teeth	28	
Module (mm)	5	
Outer Diameter (mm)	149.9	
Root Diameter (mm)	126.4	
Circular Tooth Thickness (mm)	7.64	
Face Width (mm)	15	
Lead Crowning (μm)	15	
Density (kg/m^3)	7.85×10^3	
Young's Modulus (GPa)	201.5	
Contact Ratio	1.63	1.45
Pressure Angle (deg)	20	25
Tooth Profile Modification	Parabolic	Parabolic
Tip Relief (μm)	52	47
Start Roll Angle (deg)	22.90	28.54

degrees of freedom: two translational motions y_1 and y_2 along the line of action, and two rotational motions θ_1 and θ_2. The deflections perpendicular to the line of action are not modeled because they are negligible for most applications of spur gear pairs. The gears have base radii r_{bi}, masses m_i, and moments of inertia I_i for $i = 1, 2$. The gears are supported by translational (k_{yi}) and rotational ($k_{\theta i}$) stiffnesses that represent the compliance in the supporting bearings and shaft structures. The translational and rotational damping elements are c_{yi} and $c_{\theta i}$, respectively. T_1 and T_2 are the applied torques satisfying $T_1/r_{b1} = T_2/r_{b2} = F_s$, where F_s denotes the mean mesh force (i.e., the total tooth load). F denotes the periodically changing dynamic mesh force along the line of action. The matrix equation of motion is

$$\mathbf{M}\ddot{\mathbf{q}} + \mathbf{C}\dot{\mathbf{q}} + \mathbf{K}\mathbf{q} + \mathbf{f}_d = \mathbf{f}_{ext}, \tag{3.1a}$$

$$\mathbf{q} = [y_1, \theta_1, y_2, \theta_2]^T. \tag{3.1b}$$

The mass matrix $\mathbf{M}$, damping matrix $\mathbf{C}$, and stiffness matrix $\mathbf{K}$ are

$$\mathbf{M} = \mathrm{diag}(m_1, I_1, m_2, I_2), \tag{3.2a}$$

$$\mathbf{C} = \mathrm{diag}(c_{y1}, c_{\theta 1}, c_{y2}, c_{\theta 2}), \tag{3.2b}$$

$$\mathbf{K} = \mathrm{diag}(k_{y1}, k_{\theta 1}, k_{y2}, k_{\theta 2}). \tag{3.2c}$$

The vector $\mathbf{f}_d$ contains the forces and torques from the dynamically changing mesh force F.

The vector $\mathbf{f}_{ext}$ represents forcing due to the applied torque. They are given by

$$\mathbf{f}_d = F\mathbf{v}, \tag{3.3a}$$

$$\mathbf{v} = [1, r_{b1}, -1, r_{b2}]^T. \tag{3.3b}$$

$$\mathbf{f}_{ext} = F_s\mathbf{u}, \tag{3.3c}$$

$$\mathbf{u} = [0, r_{b1}, 0, r_{b2}]^T. \tag{3.3d}$$

The mesh deflection is

$$x = \mathbf{v}^T\mathbf{q}. \tag{3.4}$$

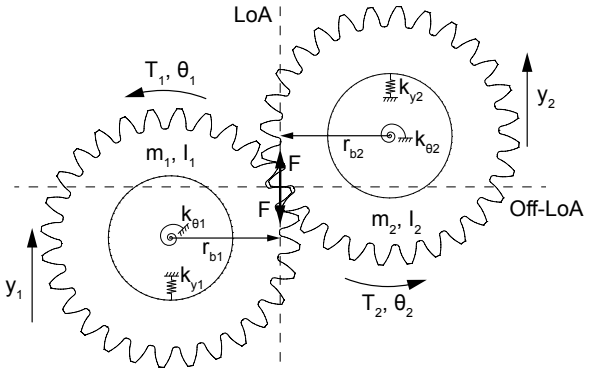

Figure 3.1: Schematic of the 28-tooth gear pair system. The vertical and horizontal dashed lines denote the line of action (LoA) and off-line of action (off-LoA), respectively.

3.2.2 Dynamic Mesh Force Modeling

The dynamic mesh force F in Eq. (5.1) is the key quantity driving the vibration. The accuracy of the model depends on the accuracy of this dynamic mesh force, which depends on the gear motions and changes as the gears rotate kinematically. The dynamic mesh force

is affected by tooth modifications, applied torque, and contact loss nonlinearities near resonances. It is calculated using a force-deflection function, as will be discussed subsequently. In contrast with usual gear dynamic models, this mesh force is not approximated by any mesh stiffness nor any static loaded or unloaded transmission error.

The dynamic motions of each gear are classified into two types: the translational and rotational vibrations of the gear as a rigid body as defined in Eq. (5.1b), and the elastic deformations of the gear teeth and blank as shown in Fig. 5.2. The translational and rotational vibrations are excited mainly by the periodically changing tooth contact conditions when the gears rotate. These vibrations are at the mesh frequency and its first several harmonics. The elastic vibrations in the gear teeth and blank (dashed arrows in Fig. 5.2) occur at free vibration natural frequencies that are generally much higher than the gear mesh frequency and the natural frequencies for the translational and rotational vibration modes associated with $\mathbf{q} = [y_1, \theta_1, y_2, \theta_2]^T$. Additionally, these high frequency vibrations have much smaller amplitude compared with the translational and rotational vibrations. Because of their high frequency, the elastic vibrations reach steady state very rapidly compared to the frequency of vibrations of the rigid body gear motions, motivating the main assumption of the current model as discussed below.

Based on this situation we make the assumption that, under dynamic conditions, the elastic, high frequency gear tooth and blank vibrations (but not the gear rigid body vibrations) achieve an "instantaneous steady state" so rapidly that there is negligible distinction between this "instantaneous steady state" and the state of elastic tooth and gear blank deformations that would occur if the mating gear teeth were loaded statically with the same

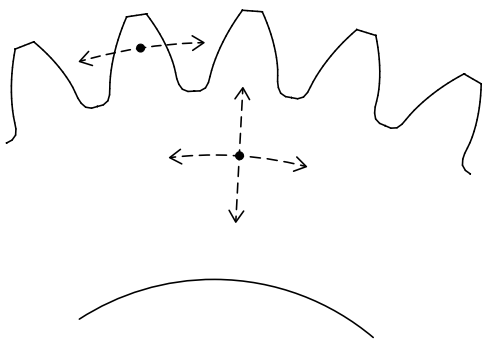

Figure 3.2: Schematic of the elastic deformation in the gear teeth and blank. The black circles represent arbitrary material points on the elastic gear body.

contact force at the same point in a mesh cycle. Essentially, we ignore the high frequency vibrations of the local tooth and gear blank deformations. The elastic tooth and gear blank deformations under dynamic conditions are then approximated by what these quantities would be for the corresponding static configuration at the same nominal gear mesh position with the same mesh deflection. Thus, the mesh force calculated in advance under static conditions for a given mesh deflection and position within a mesh cycle can be used in dynamic analyses to calculate the gear rigid body vibrations. The details of this assumption and its validity are demonstrated in results that follow. With this assumption, the dynamic contact stress, tooth root strains, and other parameters are also uniquely determined from the statically deformed configuration, as shown subsequently.

3.2.3 Force-Deflection Function

The force-deflection function (FDF) is the crucial quantity to implement the foregoing assumption. The FDF is defined as the relationship between the mesh force and mesh deflection at each nominal gear mesh position during a mesh cycle. It is calculated statically

using computational methods, as shown in Fig. 5.4 for the 28-tooth gear pair with the 25° pressure angle tooth side in contact. Although Fig. 5.4 shows two mesh cycles for better graphic presentation, the second mesh cycle is identical to the first; only one mesh cycle is needed for dynamic analyses.

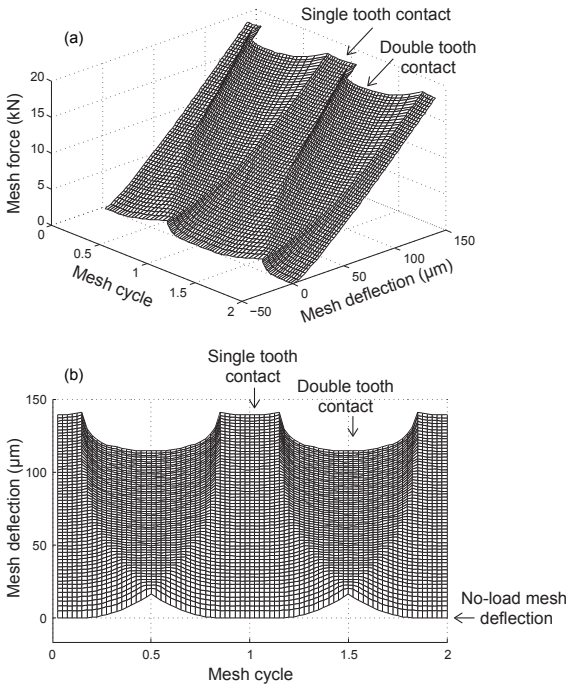

Figure 3.3: Finite element calculation of the force-deflection function for the 28-tooth gear pair with the 25° pressure angle tooth side in contact.

The FDF is assembled by statically calculating, for many statically applied torques (i.e., mesh forces) across the range of interest, the mesh deflection at many points throughout a mesh cycle. The integer mesh cycle values in Fig. 5.4 correspond to pitch point contact. The FDF is generated prior to dynamic analysis and is calculated with tooth profile and lead modifications included. The FDF is then used in the numerical integration of Eq. (5.1) to calculate the instantaneous dynamic mesh force $F(\mathbf{q}, \mathrm{t})$ based on the instantaneous mesh cycle position and mesh deflection.

Notice that during the static finite element analyses, the input quantities are the position in a mesh cycle and the mesh force (applied torque divided by base radius), and the mesh deflection is one of the output quantities. In the dynamic analytical calculations, however, the position in a mesh cycle and the mesh deflection become the inputs and the mesh force $F(\mathbf{q}, \mathrm{t})$ required in Eq. (5.1) is the output. A highlight of the proposed method is that these static finite element calculations need to be done only once for a specified gear geometry that includes the tooth modification.

The accuracy of the analytical model depends on the accuracy of the dynamic mesh force calculations, which is further determined by the underlying computational model used to compute the FDF. In this work, we use the finite element/contact mechanics software Calyx for the FDF calculations. Alternatively, the FDF can be calculated statically using other finite element formulations or commercial software.

The FE/CM model developed by Vijayakar and implemented in Calyx combines an analytical solution for the tooth contact and conventional finite element solutions for the elastic gear teeth and blank. The micro-geometry on the tooth contact surface due to tooth profile and lead modifications is precisely modeled. This model has been shown to accurately and efficiently predict gear rotational vibrations [108, 109, 107] and tooth root stresses/strains [118, 135] when compared to experiments. The technical details of the formulation can be found in Refs. [104, 105, 106]. Its essential features are summarized in Refs. [108, 107].

Although only the mesh deflection and mesh force used in the FDF are required for the dynamic simulation to obtain the rigid body gear vibrations, engineers want to know the dynamic response of many other output quantities such as the tooth fillet stresses and

strains, gear blank deformations, and contact pressures. Thus, in the static analyses, all of these desired quantities for the whole system at each nominal gear mesh position and torque are saved for later post-processing, as discussed later.

The FDF is highly sensitive to small changes on the tooth's surface due to profile and lead modifications, which are precisely modeled using the FE/CM formulation. No additional procedure beyond including them in the FDF calculation is required to deal with tooth modifications. The non-zero mesh deflections for vanishing mesh force, defined as the no-load mesh deflections (NLMD), are due to tooth profile modifications. The gears are engaged for the points where the mesh deflection exceeds the corresponding NLMD at the same mesh cycle. At any points where the mesh deflection is smaller than the NLMD, the gear teeth separate. The single- and double-tooth contact regions are labeled in Fig. 5.4. The double-tooth contact regions are wider with increasing mesh force (deflection). This is due to more tooth bending at the high load regions causing more gear teeth to be engaged. The resolution for the static analyses should be high enough so that the boundaries between single- and double-tooth contact regions are accurately captured. A similar force-deflection function is used in Ref. [14] for gear rotational vibrations near the main resonance.

Although the HAC model does not use any mesh stiffness to calculate the dynamic mesh force, the force can be represented by the mesh stiffness, that is

$$F(x,t) = F(x,t) - F(\epsilon,t) = \int_{\epsilon}^{x} [\frac{\partial}{\partial \xi} F(\xi,t)] d\xi = \int_{\epsilon}^{x} k(\xi,t) d\xi \tag{3.5}$$

where ϵ denotes the no load mesh deflection and the mesh deflection x is defined in Eq. (3.4).

We have not seen any gear dynamics model that implements mesh stiffness in this same way, that is, according to the last equality in Eq. (3.5). For the reasons discussed below, we do not recommend it. Instead, the purpose of equating the HAC method (represented by the left-hand side of Eq. (3.5)) to the last equality in Eq. (3.5) is to distinguish the HAC method from the various existing gear dynamics models that almost universally involve use of mesh stiffness in some form. It would be inconvenient to develop an approach based on the last equality in Eq. (3.5) because of the integration involved. Furthermore, one must know the mesh stiffness for each value of mesh deflection (the ξ dependence in Eq. (3.5)) and for each position in a mesh cycle (the time dependence in Eq. (3.5)). This requires performing the same set of static analyses used in the HAC method to calculate the FDF, so there is no computational savings. In fact, there is some loss of accuracy to obtain stiffness from the static analyses because it involves numerical differentiation of the force vs. deflection curve. The FDF is, however, much simpler to implement. It accepts mesh deflection and position in a mesh cycle as inputs and produces the mesh force directly (i.e., according to the left-hand side of Eq. (3.5)) with no use of mesh stiffness.

3.2.4 Calculations of Gear Translational and Rotational Vibrations

The gear translational and rotational vibrations are calculated using the analytical formulation in Eq. (5.1). At each instant, the dynamic mesh force F is calculated using the force-deflection function. Two quantities are necessary to determine the instantaneous dynamic mesh force: the current point in the mesh cycle and the dynamic mesh deflection.

The position in the mesh cycle is determined by kinematics (i.e., time). The dynamic mesh deflection is calculated from the instantaneous gear translational and rotational deflections, as shown in Eq. (3.4). Using linear interpolation, the dynamic mesh force at the instantaneous mesh cycle and mesh deflection is calculated from the FDF. Numerical integration is performed for a single time step. The process repeats at the next instant of the numerical integration, which continues as long as desired (e.g., until steady state is achieved).

3.3 Calculation of Stresses, Strains, Deformations, and Contact Pressures

The HAC method can accurately calculate the dynamic tooth stresses, strains, elastic gear/tooth deformations, and contact pressure based on the same assumption that underlies the calculation of dynamic mesh force as discussed in Sec. 3.2. In short, we assume that the instantaneous mesh deflection and nominal position in the mesh cycle determine the elastic deformation of the system (based on neglecting the high frequency vibration modes associated with local tooth bending and elastic gear blank deformation). We take this to be true even if the mesh deflection occurs under dynamic conditions. This same assumption justified the determination of the dynamic mesh force in the HAC.

With the assumption to neglect the high frequency vibrations in the gear bodies, the elastic tooth and gear blank deformations under dynamic conditions are approximated by the corresponding static values at the same nominal gear mesh position with the same mesh deflection. Thus, if we know the mesh deflection and nominal position in the mesh cycle,

then we know the elastically deformed state of the system, even when the mesh deflection occurs under dynamic conditions. The dynamic mesh deflections and nominal position in the mesh cycle are known from the numerical integration of the HAC method, however. Thus, these known dynamic mesh deflections and the foregoing assumption determines the dynamic tooth stresses, strains, elastic gear/tooth deformations, and contact pressure.

No additional computation is needed to obtain these quantities. They are determined as desired during post-processing. All that is needed is to store these desired output quantities when performing the static simulations needed for the FDF. This yields a database of information giving the stresses, strains, and elastic deformations for any combination of mesh deflection and nominal mesh position (exactly as the FDF yields dynamic mesh force for given mesh deflection and mesh position). With the known dynamic mesh deflections obtained from numerical solution of the HAC formulation, it is only a post-processing task to obtain the corresponding stresses, strains, deformations, and contact pressure from the database. Conventional lumped-parameter models generally compute the rigid body gear vibrations and dynamic transmission error but do not typically yield these output quantities.

The high accuracy of this approach is demonstrated in subsequent strain and contact pressure comparisons to experiments and the benchmark FE/CM model.

This process extends the capability of computational methods and software suited to static analysis to yield dynamic results with little loss in accuracy. With accurate static analysis capability to generate the FDF and elastic tooth/gear deformations, the HAC method yields dynamic results with accuracy almost equal to that of the underlying static analysis method.

3.4 Computational Efficiency

The proposed HAC model is computationally efficient. Figure 3.4 shows the flowchart of the HAC method. There are three steps: static FE analyses, dynamic numerical integration, and post-processing. The simulation time for the static FE analyses depends on the underlying FE code. These static analyses at each torque are much faster than dynamic analyses. At each torque, the gears are analyzed statically for only one mesh cycle. Additionally, the static finite element analyses at different torques can be performed simultaneously. These static analyses are performed only once for given tooth modification. For each static analysis at given torque, all the necessary information of the system over one mesh cycle is saved, including the gear rotational deformations (i.e., mesh deflection), mesh force, stress and strain at each node on the gear teeth, and any other output quantities of interest. Of this data, only the FDF is used in the solution for the gear pair's dynamic response. All other static output data are for post-processing to get dynamic results, as described above for root strain.

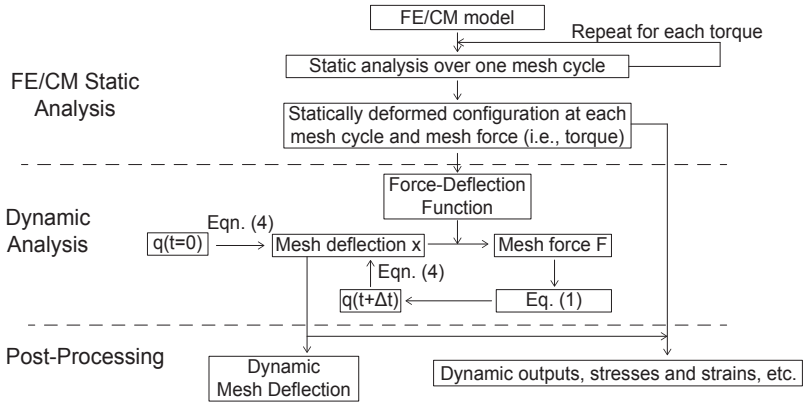

Figure 3.4: Flowchart of the hybrid analytical-computational method

The dynamic analytical calculations are as fast as numerically integrating conventional

lumped-parameter models. For the current gear pairs, it takes about 3×10^{-3} seconds on a conventional desktop computer to numerically integrate over one mesh cycle using the HAC method. This is almost five orders of magnitude faster than dynamic analysis with the FE/CM model. The gears are usually analyzed at multiple speeds over a speed range. In such cases, the total dynamic simulation time is reduced from about a month to a minute by the HAC method.

3.5 Contrast to Conventional Lumped-Parameter Models

In contrast to almost all conventional lumped-parameter models, the HAC method does not use any mesh stiffness or static transmission error calculated at a pre-selected torque as an excitation source when calculating the dynamic mesh force. Instead, this force is directly obtained from the force-deflection function based on gear kinematics and dynamic mesh deflection. In order to obtain the static mesh stiffness or transmission error, those conventional models also require finite element or similar simulations. Thus, both the HAC and conventional lumped-parameter models require equal access to finite element software and equal model development effort.

We briefly introduce the mesh force calculations in common conventional lumped-parameter models. Later we show numerical comparisons between these models, the HAC method, and benchmark FE/CM results.

In all of the models below, and in later numerical results using them, we include contact loss nonlinearity such that the tooth mesh force can never be negative (that is, only compressive tooth loads are permitted).

3.5.1 Static Transmission Error Models

The static transmission error model (STE Model) of the dynamic mesh force is [4, 7, 136, 137, 138, 139]

$$F(\tau) = \overline{k}_m[x(\tau) - x_s(\tau)] + F_s, \tag{3.6}$$

where x_s and x are the static and dynamic transmission errors, respectively. τ is the nominal gear mesh position within the mesh cycle. $\overline{k}_m$ is the mean mesh stiffness calculated from static analysis, and F_s is the static mesh force. A constant mesh stiffness is used in these STE models, and the system is excited by the periodically changing static transmission error x_s calculated at a single selected torque.

3.5.2 Mesh Stiffness Fluctuation Models

In some lumped-parameter models, the mesh force is modeled using a periodically changing mesh stiffness. The mesh stiffness is typically calculated statically using finite element analysis. There are multiple approaches to obtain the mesh stiffness [15], and the corresponding mesh force model changes based on the chosen approach.

The average slope approach is widely used [4, 5, 7, 9, 10, 136, 137, 138, 139, 15, 140,

17, 141, 142, 143, 144], and the mesh force is represented as

$$F(\tau) = k_a(\tau)[x(\tau) - \epsilon(\tau)], \tag{3.7}$$

where $k_a(\tau)$ is the average slope mesh stiffness calculated statically at the nominal load. $\epsilon(\tau)$ is the no load mesh deflection due to tooth profile modifications.

In contrast, Cooley et al. [15] conclude that the local slope approach is more appropriate for dynamic vibration analyses. The mesh force is represented as

$$F(\tau) = k_l(\tau)[x(\tau) - x_s(\tau)] + F_s, \tag{3.8}$$

where $k_l(\tau)$ is the local slope stiffness at the nominal load.

The two mesh force representations in Eqs. 3.7 and 3.8 are less accurate than Eq. 3.5 because they implicitly assume that the mesh stiffness is constant as the mesh deflection (i.e., tooth mesh force) changes, that is, it equals its value when the nominal torque is applied statically. The deviation of the instantaneous dynamic mesh stiffness due to incomplete tooth contact and partial contact loss is not captured. These models may give accurate results when the system vibrates around its equilibrium with small amplitude. When the gears are running near resonances, however, large amplitude vibrations are excited and these models are less accurate (see Ref. [11]).

3.5.3 Dynamic Mesh Stiffness Models

Eritenel and Parker [11] present gear vibration results showing that the mesh stiffness under dynamic conditions differs from the mesh stiffness under static conditions, with the differences arising because of the dynamically fluctuating tooth mesh force. Palermo et al. [145, 146, 147] analyzed nonlinear gear dynamics using a lumped-parameter model that addresses this issue. Prior to dynamic analysis, the gears are analyzed statically at varying torques to build a database. When the gears are analyzed dynamically, the dynamic mesh stiffness is obtained from the database. The mesh stiffness based approaches in all of these works differ from the HAC method that does not use mesh stiffness. Even when casting the HAC method in terms of mesh stiffness, as done in Eq. (3.5), it is evident that the HAC method involving integration of mesh stiffness as shown in Eq. (3.5) differs from [11, 145, 146, 147]. In addition, a crucial feature of the present method is its accurate calculation of stresses, strains, contact pressure, etc., which are not obtained in Refs. [145, 146, 147].

3.5.4 Force-Deflection Function Model

Eritenel and Parker [14] developed a lumped-parameter model for nonlinear gear pair dynamics. The dynamic mesh force is obtained using a force-deflection function, like in the HAC method. The gear rotational vibrations near the main resonance are obtained using a mathematical perturbation analysis. Their model is not able to predict gear elastic stresses and strains. The HAC formulation in the current work, however, reveals the relationship between the gear static and dynamic contact conditions and is able to predict these stresses

and strains that are often the most desired and practically important outputs of dynamic simulations.

3.6 Numerical Results

Results that follow compare the HAC model to experiments and to dynamic, time-domain numerical integration of the FE/CM model. The principal benchmark for the HAC model is the dynamic FE/CM model, more than the experiments. Because the HAC model relies on the FE/CM model for the static analyses to generate the FDF, it can not be more accurate. Comparisons of the HAC model to the dynamic FE/CM results illustrate how much or how little accuracy is lost with the HAC method. Comparisons to experiments are determined by the accuracy of the FE/CM model rather than the HAC model (because the HAC model can not yield better results than the FE/CM model).

3.6.1 Gear Pairs With Purely Rotational Deformations

For most experiments on gear pairs, the stiffnesses of the supporting structures are much larger than the gear mesh stiffness. Therefore, the gear translational vibrations are negligible compared with the rotational vibrations. We focus on the gear rotational vibrations for these systems.

50-tooth Gears

The natural frequencies for the gear pair systems are numerically predicted by time domain impulse tests. The gears are initially at rest in static equilibrium at the nominal load, and then a torque impulse is applied and the resulting transient response is analyzed. The natural frequencies are calculated for both single- and double-tooth contact states, and the mean natural frequency of the system is calculated according to the contact ratio.

Table 3.4 compares the natural frequencies predicted by the HAC model, FE/CM model, and experimental measurements for the 50-tooth gear pairs. The natural frequencies for both the ICR 1.37 unmodified gears and the ICR 1.8 modified gears are accurately predicted by the HAC and FE/CM models.

Table 3.4: Numerical calculation of the natural frequencies (Hz) for the 50-tooth gear pairs compared with experiments from Refs. [2, 1]. Percentages indicate differences with experiments.

	ICR 1.37, unmodified 170 N-m torque	ICR 1.8,modified 200 N-m torque
Experiments	2700	2750
HAC model	2600 (-3.8%)	2750 (<1%)
FE/CM model	2650 (-1.9%)	2938 (6.6%)

The gears are analyzed dynamically over a wide range of speed and torque combinations. At each speed, the gears are analyzed for a number of mesh cycles to diminish the transient response and only steady state response is recorded. Figure 3.5(a) shows the HAC calculation of the root mean square (RMS) of the oscillating component of dynamic mesh deflection compared with the FE/CM results and experiments [2]. The gears have ICR 1.37 without tooth profile modifications, and the applied torque is 170 N-m. The resonance locations are accurately predicted by both the HAC and FE/CM models compared with experiments,

including the main resonance near $f_m/f_n = 1$ and those near $f_m/f_n = 0.5$ and $f_m/f_n = 0.33$, where the second and third harmonics of mesh frequency cause resonance. Excellent agreement is seen between the calculated dynamic response amplitudes and experiments over a wide range of speeds, including resonant and off-resonant gear speeds. More importantly for HAC model validation, however, is that negligible differences occur between the HAC and FE/CM models. The classical softening nonlinearity that results from tooth contact loss is accurately captured by both the HAC and FE/CM models, as shown by the double-valued region at $0.7 < f_m/f_n < 0.9$ in Fig. 3.5(a). The jump-up and jump-down frequencies are accurately predicted.

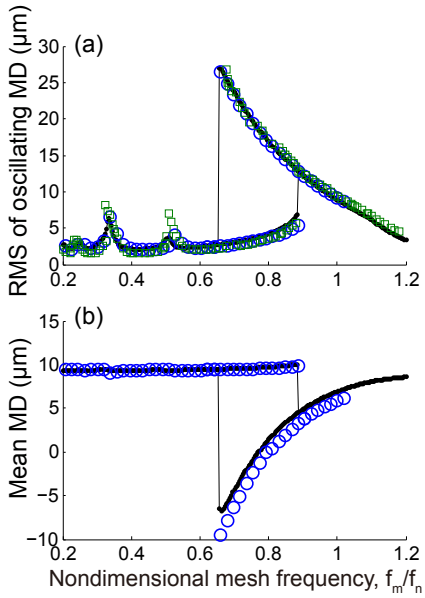

Figure 3.5: (a) Oscillating (RMS) and (b) mean components of the dynamic mesh deflections for the 50-tooth ICR 1.37 gear pair with unmodified teeth. The applied torque is 170 N-m. The black dots, blue circles, and green squares denote the HAC calculations, FE/CM calculations, and experiments from Ref. [2], respectively.

Figure 3.5(b) shows the comparison of the mean value of mesh deflection calculated from the same simulations as the results shown in Fig. 3.5(a). Only the results from HAC and FE/CM models are compared because there is no available experimental data. The

good agreement between the two models continues. The upper and lower branches for the double-valued region near the main resonance are switched for the mean mesh deflection. The dynamic response remains on the upper branch for increasing speed sweeps starting from the low speed region, and "jumps" to the lower branch near resonance, as shown near $f_m/f_n = 0.9$ in Fig. 3.5(b). Similarly, the dynamic response remains on the lower branch for decreasing speed sweeps, and "jumps" to the upper branch near $f_m/f_n = 0.65$.

Figure 3.6 shows the dynamic mesh deflections for an ICR 1.8 gear pair with tooth profile modifications at 200 N-m applied torque. The good agreement continues for these gears. The amplitude of the oscillating mesh deflection for the modified gears (Fig. 3.6(a)) is generally smaller than that for the unmodified gears (Fig. 3.5(a)), although the modified gears are at a higher applied torque. This is due to the tooth profile modifications.

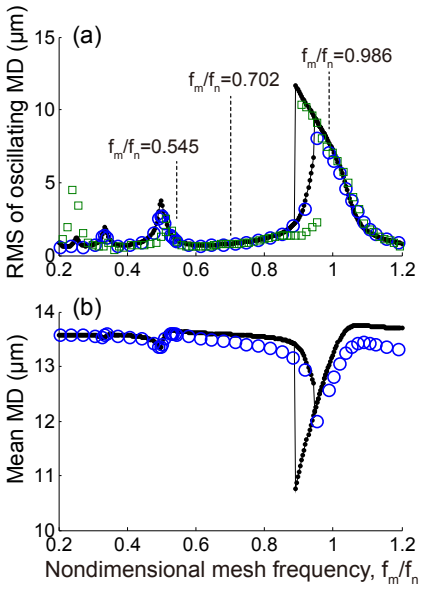

Figure 3.6: (a) Oscillating (RMS) and (b) mean components of the dynamic mesh deflections for the 50-tooth ICR 1.8 gear pair with tooth profile modifications. The applied torque is 200 N-m. The black dots, blue circles, and green squares denote the HAC calculations, FE/CM calculations, and experiments from Ref. [1], respectively.

Figure 3.7 shows the dynamic tooth root strains calculated from the HAC model compared with FE/CM results and experiments from Ref. [1] for the ICR 1.8 gears with tooth profile modifications at the three frequencies indicated by vertical lines in Fig. 3.6. Excellent agreement occurs at each speed, including near resonances when contact loss occurs (Fig. 3.7(c)). This strong nonlinearity is accurately captured by both the HAC and FE/CM models. The strain curves calculated by the HAC model are nearly identical to the FE/CM calculations for all three speeds. Similar agreement occurs at other speeds, which is not shown. Typical lumped-parameter gear models do not predict dynamic tooth root/fillet strains or other elastic tooth and gear blank deformations.

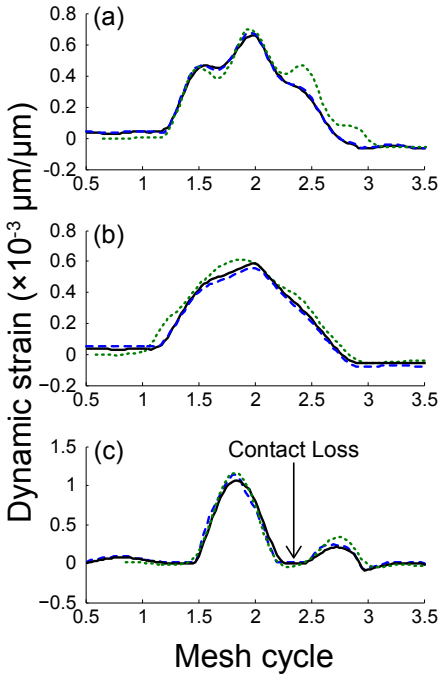

Figure 3.7: HAC calculation of dynamic tooth root strains compared with FE/CM results and experiments [1] for the 50-tooth spur gear pair. The gears have ICR 1.8 with tooth profile modifications. The strains are calculated at $R = 70.7mm$ where maximum strain occurs in the tooth root region. The gears are at (a) $f_m/f_n = 0.545$, (b) $f_m/f_n = 0.702$, and $f_m/f_n = 0.986$ and 200 N-m applied torque. The solid black lines, dashed blue lines, and dotted green lines denote the HAC calculations, FE/CM calculations, and experiments, respectively.

Figure 3.8 compares the mesh deflection, mesh force, and tooth contact pressure calculated by the HAC and FE/CM models for the ICR 1.8 gear pair with tooth profile modifications. The gears have 200 N-m of applied torque and the mesh frequency $f_m/f_n = 0.986$ is near the natural frequency where high amplitude vibrations are excited (Fig. 3.6(a)). Contact loss occurs, as seen by the vanishing mesh force and contact pressure near mesh cycle 2.4 in Figs. 3.8(b) and 3.8(c). Only the results from HAC and FE/CM models are compared because there is no available experimental data. All results agree well.

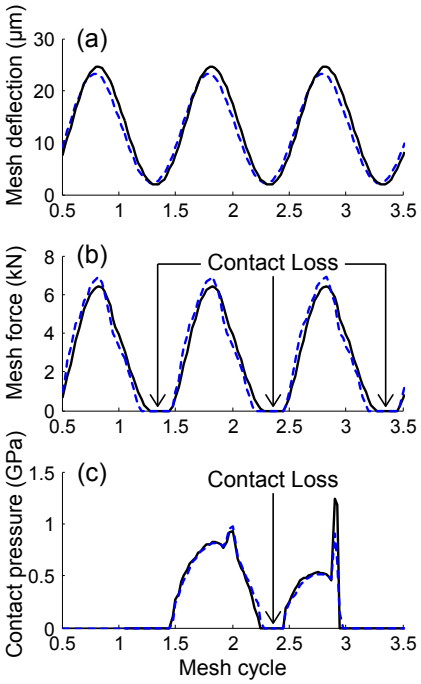

Figure 3.8: HAC calculation of (a) dynamic mesh deflection, (b) dynamic mesh force, and (c) dynamic contact pressure compared with FE/CM results for the 50-tooth spur gear pair at $f_m/f_n = 0.986$ and 200 N-m torque. The gears have ICR 1.8 with tooth profile modifications. The solid black lines and dashed blue lines denote the HAC calculations and FE/CM calculations, respectively.

28-tooth Gears

We investigate another pair of gears with entirely separate experiments to further validate the HAC model. The gear parameters are given in Table. 3.3.

The natural frequency for the 28-tooth gear pair at 300 N-m torque with the 25° pressure angle tooth side in contact is 2775 Hz from the HAC model. This is within 0.9% of the FE/CM calculation (2800 Hz) and 1.8% of the experiments (2825 Hz). The natural frequencies predicted by the STE model, average slope model, and local slope model are 2427 Hz, 2427 Hz, and 2749 Hz, respectively. For the three conventional lumped-parameter models, the natural frequency predicted by the local slope model is more accurate compared with FE/CM predictions and experiments. The natural frequencies from STE model and average slope model are more than 10 percent smaller compared with the local slope model. This is because the mesh stiffness is not appropriately calculated in these models.

Figure 3.9 shows the HAC calculation of dynamic tooth root strains compared with FE/CM results and experiments at two speeds ($f_m/f_n = 0.571$ and $f_m/f_n = 0.893$) and 300 N-m torque with the 25° pressure angle tooth side in contact. The strains are not available from the conventional lumped-parameter models. Excellent agreement continues for the 28-tooth gear pair. Both the shape and peak amplitude of the strain curves are accurately predicted. The HAC and FE/CM models give nearly identical dynamic strain curves, as shown by the solid black and dashed blue lines in Figs. 3.9(a) and 3.9(b). The deviation between the numerical calculations and experiments (dotted green line) are due to the sensitivity of the strain gage location, as discussed in Ref. [135]. Correlation between

the HAC and FE/CM models and between the numerical and experimental results occurs at other speeds and torques (not shown).

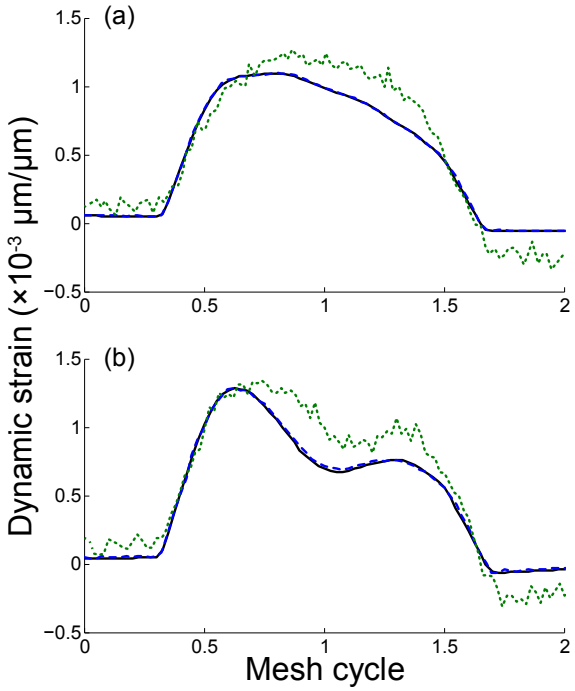

Figure 3.9: HAC calculation of dynamic tooth root strains compared with FE/CM results and experiments for the 28-tooth spur gear pair. The gears are at (a) $f_m/f_n = 0.571$ and (b) $f_m/f_n = 0.893$ and 300 N-m torque with the 25° pressure angle tooth side in contact. The solid black lines, dashed blue lines, and dotted green lines denote the HAC calculations, FE/CM calculations, and experiments, respectively.

We want to distinguish the current method from the conventional lumped-parameter models introduced earlier in Section 3.5. Figure 3.10(a) compares the HAC calculation of the RMS of the oscillating mesh deflection with FE/CM results and conventional lumped-parameter model results. The RMS values predicted by the HAC and FE/CM models are nearly identical over a wide range of speeds, including near the resonant gear speeds when high amplitude vibrations are excited and contact loss occurs. The resonance locations and nonlinear jump-up and jump-down frequencies are accurately predicted. Good agreement continues for the mean mesh deflections (Fig. 3.10(b)). The local slope model accurately

predicts the RMS value compared with the HAC and FE/CM calculations, as shown by the black triangles in Fig. 3.10(a). The accuracy for the mean mesh deflection is lower, as shown in Fig. 3.10(b). The accuracy for the STE model (plus signs) and average slope model (crosses) is much lower compared with the HAC model and local slope model, as shown in Fig. 3.10.

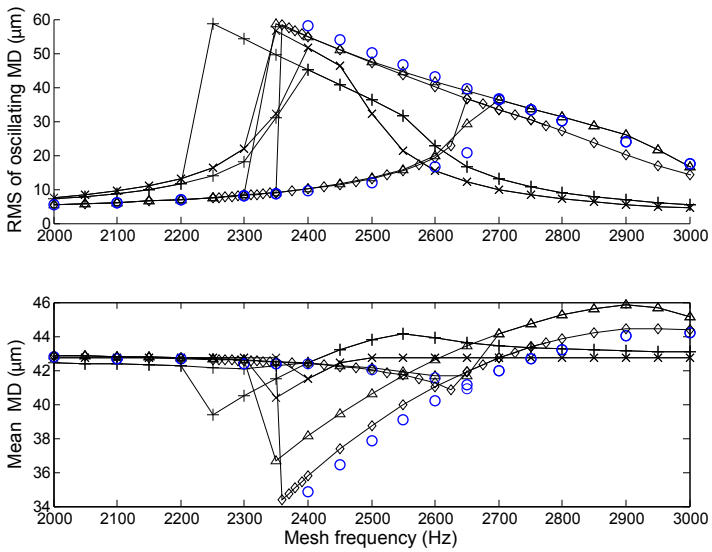

Figure 3.10: (a) Root mean square (RMS) of oscillating component and (b) mean value of the dynamic mesh deflection for the 28-tooth spur gear pair at 300 N-m torque with the 25° pressure angle tooth side in contact. The blue circles ○ and black diamonds ◇ denote the FE/CM and HAC calculations, respectively. The plus signs +, crosses ×, and triangles △ denote the STE model, average slope model, and local slope model results, respectively.

Figure 3.11 compares the mesh deflection, mesh force, and tooth contact pressure calculated by the HAC model, FE/CM model and the three conventional lumped-parameter models for the 28-tooth gear pair. The gears are at $f_m = 1600$ Hz. Nearly identical results are shown between the HAC and FE/CM predictions for each of the mesh deflection, mesh force, and tooth contact pressure curves. The local slope model also gives accurate results, as shown the triangles in Fig. 3.11(a) and (b). The STE model and average slope model give less accurate results. The contact pressure is not available for conventional lumped

parameter models, so only the HAC and FE/CM results are compared. Excellent agreement between the HAC and FE/CM predictions occurs at other speeds and torques as well, which is not shown.

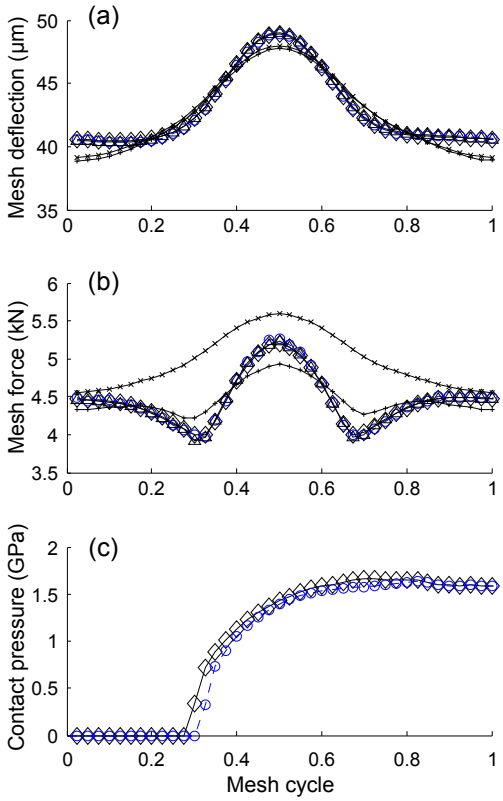

Figure 3.11: (a) Dynamic mesh deflection, (b) dynamic mesh force, and (c) dynamic tooth contact pressure for the 28-tooth spur gear pair at $f_m = 1600Hz$ and 300 N-m torque with the 25° pressure angle tooth side in contact. The blue circles ○ and black diamonds ◇ denote the FE/CM and HAC calculations, respectively. The plus signs +, crosses ×, and triangles △ denote the STE model, average slope model, and local slope model results, respectively.

Although the mesh stiffness is not used in the HAC dynamic calculations, they can be obtained from the force-deflection function. Figure 3.12 compares the HAC calculation of dynamic mesh stiffness for the 28-tooth gear pair near resonance ($f_m/f_n = 1.027$) with the static mesh stiffness calculated at the nominal load, as used in conventional lumped-parameter models. Substantial differences occur between the static and dynamic mesh stiff-

ness curves even though the gear teeth never totally separate during the mesh cycle. When the gears rotate dynamically, the deviation between static and dynamic mesh deflections changes the dynamic mesh stiffness, which further affects the gear dynamic response. The steady state dynamic response of the gears is a result of the interactions between the dynamic mesh stiffness and mesh deflection. Similar comparisons can be found in Ref. [11].

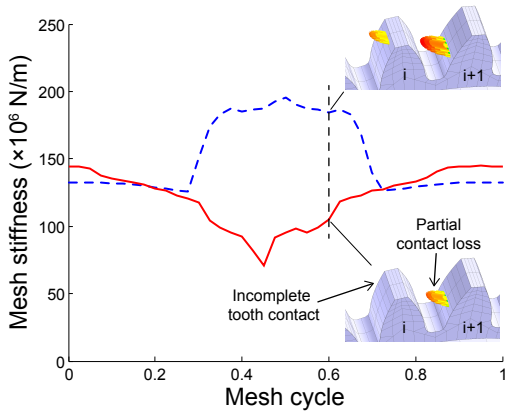

Figure 3.12: HAC calculation of dynamic mesh stiffness (solid red line) for the 28-tooth gear pair at 300 N-m torque with the 25° pressure angle tooth side in contact and $f_m/f_n = 1.027$. The dashed blue line denotes the static mesh stiffness calculated using the local slope method at the nominal load. The FE/CM calculation of instantaneous tooth contact pressure on the gear teeth at mesh cycle 0.6 is shown in the sub-figures.

The instantaneous tooth contact conditions at mesh cycle 0.6 are shown in the sub-figures of Fig. 3.12. There are two teeth taking load for the static condition, but incomplete tooth contact (one of the adjacent tooth pairs normally in contact losing contact [135]) occurs for the steady state dynamic solution: only tooth $i+1$ takes load while there is no contact pressure on tooth i. Additionally, partial contact loss (portions of gear teeth contact lines losing contact [12]) occurs on tooth $i+1$, as shown by the dynamic solution having a smaller contact region than the static case. The tooth contact conditions are directly related to the gear mesh stiffness. The changing mesh stiffness due to incomplete tooth contact and partial

contact loss is not captured by conventional lumped-parameter models that were introduced in Sec. 3.5. More details about incomplete tooth contact and partial contact loss can be found in Refs. [12, 135].

Among the STE-based and mesh stiffness fluctuation (local and average slope) lumped-parameter models, the local slope model gives the most accurate solutions, as shown in the comparisons on Figs. 3.10 and 3.11. This model and its reliance on a mesh stiffness fluctuation calculated at a specific torque is, however, still fundamentally less accurate than the HAC method. For example, Fig. 3.13 compares the RMS value of oscillating mesh deflection calculated from the HAC model, FE/CM model, and local slope model for the 28-tooth gear pair at 100 N-m torque. Good agreement is observed between the HAC and FE/CM results, including the resonance locations near 1600 Hz and 2200 Hz. The local slope model (triangles) predicts the resonance near 2200 Hz less accurately but still with minor error. The additional resonance near 1600 Hz, which is clearly evident in the FE/CM simulations, is completely missed by the local slope model (and the STE-based and average slope models) but accurately captured by the HAC method.

3.6.2 Gear Pairs With Meaningful Translational Deformations

The gear pair systems analyzed in Sec. 3.6.1 have negligible translational deformations because of the high stiffness of the bearings and supporting structures used in the experiments. In order to further validate the HAC model, the 28-tooth gears are analyzed with more compliant supports that introduce meaningful translational gear deflections. The translational stiffnesses are $k_{y1} = k_{y2} = 200 \times 10^6 N/m$, which is comparable to the mean

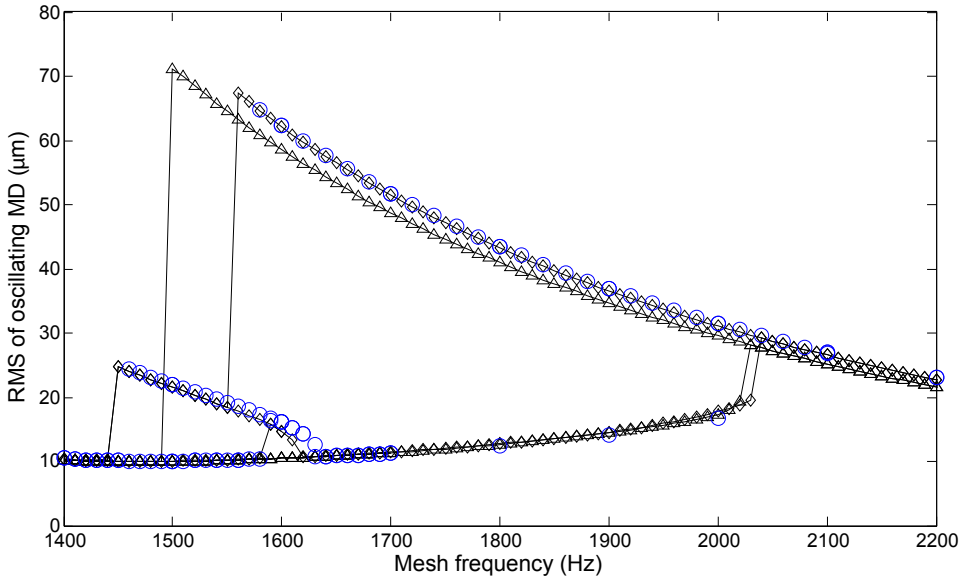

Figure 3.13: HAC calculation of root mean square (RMS) of oscillating component of the dynamic mesh deflection for the 28-tooth spur gear pair at 100 N-m torque with the 25° pressure angle tooth side in contact compared with FE/CM results and local slope model results. The blue circles ○, black diamonds ◇, and black triangles △ denote the results from FE/CM model, HAC model, and local slope model, respectively.

mesh stiffness for these gears ($150 \times 10^6 N/m$). No experimental results are available for this case.

The four degree-of-freedom system is analyzed at 300 N-m torque with the 25° pressure angle tooth side in contact. The natural frequency for the main resonance is predicted from time domain impulse tests. The HAC calculation of the highest natural frequency is 4150 Hz, within 3% of the FE/CM results of 4250 Hz. The natural frequencies with and without the compliant supporting structures differ substantially, and they are all accurately predicted by the HAC model compared with the FE/CM calculations.

Figure 3.14 shows the HAC calculation of translational deflections for the four-degree-of freedom system compared with FE/CM results. The translational vibrations for both gears are accurately predicted, including the amplitude and phase of the deflection curves. Good

agreement continues at other speeds and for other output quantities, which are not shown.

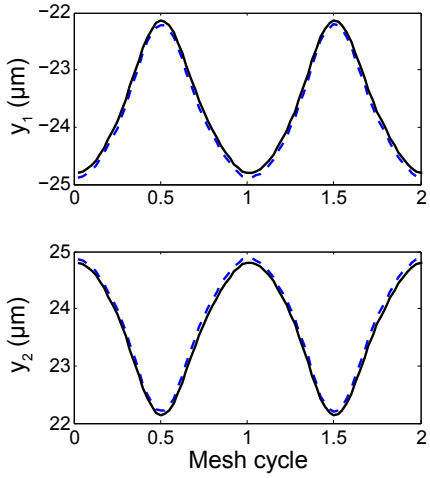

Figure 3.14: HAC calculation of translational deformations compared with FE/CM results for the 28-tooth spur gear pair at $f_m/f_n = 0.706$ and 300 N-m applied torque with the 25° pressure angle tooth side in contact. The gear translational bearing stiffnesses are $k_{y1} = k_{y2} = 200 \times 10^6 N/m$. The solid black lines and dashed blue lines denote the HAC calculations and FE/CM calculations, respectively.

Figure 3.15 compares the RMS of the oscillating component and the mean value of the dynamic mesh deflection for the four degree-of-freedom system. Excellent agreement continues even when the gears have meaningful translational deflections.

3.6.3 Restrictions

While the proposed HAC model is computationally efficient, its accuracy depends on the underlying finite element formulation. The crucial dynamic mesh force is calculated using the force-deflection function, which is generated from the static finite element analyses. Thus, the accuracy of the static analyses determines the accuracy of the dynamic analysis. The HAC method itself introduces minimal error compared to the same analysis tool executed dynamically for the gears considered in this paper, as shown by the negligible

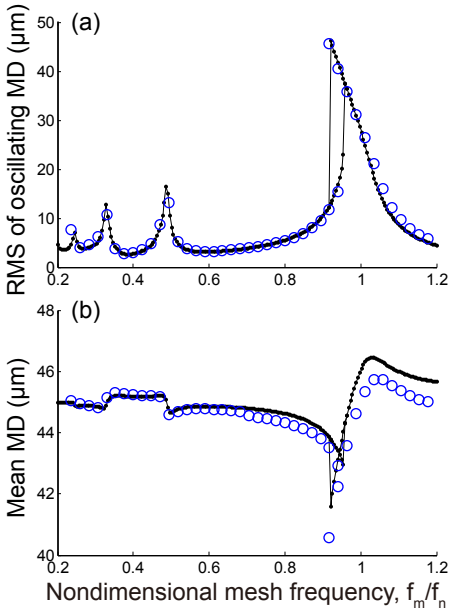

Figure 3.15: HAC calculation of (a) root mean square (RMS) of the oscillating component and (b) mean value of the dynamic mesh deflection compared with FE/CM results for the 28-tooth spur gear pair at 300 N-m torque with the 25° pressure angle tooth side in contact. The gear translational bearing stiffnesses are $k_{y1} = k_{y2} = 200 \times 10^6 N/m$. The black dots and blue circles denote the HAC calculations and FE/CM calculations, respectively.

differences between the HAC and FE/CM models in Sec. 3.6. Considering experiments, an accurately calculated force-deflection function with the HAC method successfully predicts gear translational and rotational vibrations, as shown by the comparisons in Sec. 3.6. The accuracy for other output quantities, for example, the dynamic tooth root strains and contact stresses, depends on the capability of the underlying finite element formulation to predict the corresponding static values.

The HAC model gives more accurate results when the gear blanks are stiff. The difference between the natural frequencies calculated by the HAC model and the FE/CM model is 0.9% for the purely rotational model of the 28-tooth gears, which is smaller than for the ICR 1.37 50-tooth gears without tooth modifications (1.9%) and the ICR 1.8 50-tooth gears with tooth modifications (6.6%). This is due to the elastic deformations being more concentrated

in the gear teeth for the 28-tooth gears. The high frequency vibrations in the gear blanks, which are neglected in the HAC model, have smaller effects on the 28-tooth gears. The larger natural frequency differences for the 50-tooth gears are due to more compliant gear blanks.

3.7 Conclusions

A hybrid analytical-computational (HAC) method to compute the nonlinear dynamic response in spur gear pairs is proposed. Neglecting the high frequency vibrations in the elastic gear teeth and gear bodies, the elastic tooth and gear blank deformations under dynamic conditions are approximated by the corresponding static configuration at the same nominal gear mesh position with the same mesh deflection. The gear translational and rotational vibrations are calculated numerically using lumped-parameter models where the crucial dynamic mesh force is determined from a force-deflection function that is generated in advance through a series of static finite element analyses. The accuracy of the HAC model for dynamic analyses essentially equals the accuracy of the underlying finite element formulation for static analyses provided the gears have typically stiff gear blanks.

The HAC model accurately predicts the nonlinear dynamic response of spur gear pairs compared with the FE/CM results and available experimental data, including near resonant gear speeds when high amplitude vibrations and contact loss occur. Classical softening type nonlinearities are captured, and the jump-up and jump-down frequencies are accurately predicted.

The HAC model is computationally efficient. The method requires a series of static finite

element analyses at a range of torques. These static analyses are performed only once for a specific tooth modification. Once the static analyses are finished, the dynamic analytical calculations are as fast as conventional lumped-parameter models.

The elastic deformations of the gear teeth, including any desired tooth root strains and contact stresses, are calculated using the static finite element results together with the dynamic analytical results. The accuracy of the elastic deformations and strains in the gear teeth depends primarily on the capability of the underlying finite element code to predict the corresponding static values.

The dynamic (as compared to static values at the nominal mesh force) mesh stiffness fluctuation due to incomplete tooth contact and partial contact loss is accurately captured by the HAC model. Because of its more accurate dynamic mesh force (or, equivalently, mesh stiffness) modeling, the HAC method more accurately represents the tooth contact compared with conventional lumped-parameter models when predicting the dynamic response.

Chapter 4

An Efficient Hybrid Analytical-Computational Method for Nonlinear Gear Dynamics in Multi-mesh Systems

4.1 Motivation and Objectives

Gears are important components in many industrial applications. They are widely used in power transmission systems in different types of combinations (like gear chains, planetary gears, etc.) in order to satisfy the requirement of the system. The gear vibrations are transmitted to the main structure through bearings, and are directed related to the noise in the system. The large gear tooth root stresses and strains are as a result of dynamic mesh force, which may cause system failure. These effects are especially near resonant gear speeds when high amplitude vibrations are excited and contact loss occurs. We want a fast and reliable tool to understanding and predicting these nonlinear behaviors in gear systems.

Among the many tools for gear dynamics, lumped-parameter models are the most commonly used. These models assume the gears to have rigid bodies, and connected by stiffness

elements. Early works on gear dynamics using lumped-parameter models can be found in Refs. [148, 5, 6] and their references. In an early work, Gregory et al. [7] studied the in-plane vibrations for spur gear pairs. Blankenship and Singh [8, 9] investigated the three-dimensional vibrations for helical gear pairs using a mesh interface model. Velex and Maatar [5] investigated the dynamic response for gear pairs with tooth modifications. Eritenel and Parker [11, 12] investigated the three-dimensional nonlinear vibrations in gear pairs using a lumped-parameter model with discretized stiffness network. Eritenel and Parker [14] derived closed-form solutions for spur gear pairs using a lumped-parameter model. The nonlinear dynamic response near the main resonance is given from a perturbation method. Cooley et al. [15] compared two approaches of calculating the gear tooth mesh stiffness, which is commonly used in lumped-parameter models.

Lumped-parameter models are also used for the systems with multiple tooth contact, including the idler gear systems and planetary gear systems. Lin and Parker [33, 34] investigated the parametric instability in three-gear systems. The effects from mesh stiffness, contact ratios, and mesh phasing are studied. Liu and Parker [35] developed a lumped-parameter model for multi-mesh gear vibrations. Their model includes time-varying mesh stiffnesses, profile modifications, and contact losses. The closed-form expressions for the three-gear systems are derived using perturbation methods [36, 37].

Studies on planetary gears using lumped-parameter models can be found in the review articles [38, 39]. Cunliffe et al. [40] investigated the dynamic tooth loads in epicyclic gears using a thirteen degree of freedom model. Botman [41] developed an eighteen degree-of-freedom model for planetary gears. The model includes the effect from carrier rotation and variation

of planet bearing stiffnesses. Frater et al. [42] extended Botman's model [41], and studied the vibration in planetary gear systems with unequal planet stiffnesses. Kahraman [43] investigated the natural modes of planetary gear systems. The planet translations are described in Cartesian coordinates. Saada and Velex [44] expressed the generalized displacements in the rotating frames in their model. Lin and Parker [45] derived the equation of motion for general planetary gear systems using a lumped parameter model, and investigated the modal properties at low speed. They summarized the three types of mode shapes in the systems with identical and equally spaced planet gears. Their following works investigated the natural frequency and vibration mode sensitivities to key planetary gear design parameters [46], structured vibration characteristics of planetary gears with unequally spaced planets [47], and eigenvalue veering phenomena in planetary gears [48] using the same lumped-parameter model. Sun and Hu [49] investigated the nonlinear dynamics of a planetary gear system with back lash and time-varying mesh stiffness using a lumped-parameter model. Abousleiman and Velex [50] developed a hybrid three-dimensional finite element/lumped parameter model for quasi-static and dynamic analyses for planetary/epicyclic gear systems. Ambarisha and Parker [51] investigated the nonlinear dynamics of planetary gears using a lumped-parameter model. Shyyab and Kahraman [52] developed a lumped-parameter model that includes all possible power flow configurations. Eritenel and Parker [53] investigated the modal properties of helical planetary gear system with equally spaced planet using a three-dimensional lumped-parameter model that allows for six degrees of freedom per gear-shaft body. Guo and Parker [54, 55] included the tooth wedging and bearing clearance nonlinearities in their model for planetary gears. Bahk and Parker [56, 57] gave closed-form solutions for the planetary gear systems near primary, sub- and super-harmonic resonances using a perturbation

analysis. Ericson and Parker [58, 92] investigated the planetary gear modal vibrations and natural frequency clusters using a lumped-parameter model.

Conventional finite element methods usually focus on static conditions for gear analyses [93, 94, 95, 96, 97, 98, 99, 100, 101, 102, 103]. When the gears are taking load, the elastic deformations in the tooth contact region is orders of magnitude smaller than the gear teeth and blank. A highly refined finite element mesh is required in the tooth contact region. Additionally, as the gears are rotating kinematically, the contact location moves along the tooth surface. As a result, re-meshing is required or the entire tooth surface need a highly refined finite element mesh. Either option is computationally efficient. The computational efficiency is much lower for multi-mesh systems, which usually have multiple tooth contact pairs. Therefore, dynamic analyses for multi-mesh systems are usually not available using conventional finite element methods.

A finite element/contact mechanics (FE/CM) formulation is developed for contact problems in multi-body dynamics [104, 105, 106]. Parker et al. [107] presented comprehensive dynamic response results for in-plane motions of a planetary gear system using the FE/CM model. Parker et al. [108] investigated the nonlinear dynamic response of two-dimensional spur gear pairs using the FE/CM model. Classical softening type nonlinearities, including the jump-up and jump-down frequencies are accurately captured, and validated against experiments. Kahraman et al. [111] analyzed a planetary gear system with thin rim. Cheon and Parker [113] investigated the influence of manufacturing errors on the dynamic response of planetary gears. The effect of bearing stiffness on the static properties of planetary gear systems with manufacturing errors are studied in the following work [114]. Yuksel and Kahra-

man [115] investigated the dynamic tooth loads of planetary gears having tooth wear. Singh [116] investigated the load sharing in three-dimensional planetary gear systems. The influence of planetary needle bearings on the performance of single and double pinion planetary systems are studied in Ref. [117]. Ambarisha and Parker [51] validated the strong nonlinear behavior that observed from analytical results using the FE/CM model. Tamminana et al. [118] studied the relationship between the dynamic factors and the dynamic transmission error of spur gear pairs using the same FE/CM formulation. The dynamic factors defined by transmission error, mesh force, tooth load, and bending stresses over a wide speed range are calculated and compared with experiments. Cooley et al. [109] developed a frequency domain finite element approach for three-dimensional gear dynamics. Ericson and Parker [58] studied the modal vibrations in planetary gears, and correlated against experimental measurements. Dai et al. [135] investigated the dynamic tooth root strains in spur gear pairs using the FE/CM model. The FE/CM model is computationally efficient compared with conventional finite element methods, dynamic analysis are feasible. For multi-mesh systems, especially the planetary gears, however, the FE/CM model is still lack of efficiency.

Dai et al. [3] developed a hybrid analytical-computational (HAC) method for nonlinear dynamics in spur gears. The model is based on an underlying finite element code. The gear translational and rotational vibrations are calculated using conventional lumped-parameter models, while the dynamic mesh force is calculated using a force-deflection function that is generated from static finite element analyses before the dynamic calculations. Elastic deformation of gear teeth, including the tooth root strains and contact stresses, are calculated through post processing. The HAC model is computationally efficient with almost no loss

of accuracy compared with the underlying finite element tool.

In this work, we extend the HAC method [3] to multi-mesh systems, including the idler gear systems and planetary gear systems. The system is analyzed dynamically using a lumped-parameter model where the tooth contact forces at each instant of numerical integration are obtained from a force-deflection function that generated in advance using static analyses. The force-deflection function, defined as the relationship between gear mesh force and mesh deflection at each nominal gear mesh position, is generated through a series of static analyses using a finite element/contact mechanics (FE/CM) model. The effects of tooth modifications are included in these force-deflection functions; there is no additional procedures to incorporate the tooth modifications during dynamic analyses. For multi-mesh systems, there are multiple force-deflection functions, one for each tooth engagement. The different approaches to generating these force-deflection functions are investigated. The phasing relationship of the force-deflection functions for each planet gear is explained. The gear translational and rotational vibrations are accurately calculated compared with the FE/CM results, for both the idler gear systems and planetary gear systems. The dynamic response of planetary gears are drastically different for different number of planets and tooth modifications, and they are all accurately predicted by the HAC method compared with the FE/CM results, including near resonant gear speeds when high amplitude vibrations are excited and contact loss occurs. Additionally, the elastic deformations in the gear teeth, including the tooth root strains and contact stresses, are also accurately calculated. The simulation time for the HAC model is more than three orders of magnitude lower than the FE/CM model.

4.2 Analytical Formulations

There are two multi-mesh systems studied in this work: an idler gear system with three gears, and a planetary gear system. These systems consists of only spur gears, the out-of-plane motions are negligible.

4.2.1 Idler Gear System

Figure 4.1 shows a schematic of the idler gear system. The system has three rotational degrees of freedom $\hat{\theta}_1$, $\hat{\theta}_2$ and $\hat{\theta}_3$. The translational deflections are not included. The gears have asymmetric teeth, and the base radii are r_{ij}, where i denotes the ith gear tooth mesh and j denotes the jth gear of the mesh. The tooth contact pressure angle for the first and second gears are α_1 and α_2. The moments of inertia of the gears are I_i for $i = 1$, 2, and 3, respectively. The torsional stiffness in the supporting shaft structures are $k_{\theta i}$. The damping elements are $c_{\theta i}$. T_1 and T_3 are the applied torques satisfying $\frac{T_1}{r_{11}} = F_{s1}$, $\frac{T_3}{r_{22}} = F_{s2}$, and $F_{s1} r_{12} = F_{s2} r_{21}$, where F_{si} denotes the static mesh force (total tooth load). $F_{1,2}$ denotes the periodically changing dynamic mesh force for the first and second mesh, respectively. The matrix equation of motion is

$$\hat{\mathbf{M}}\ddot{\hat{\mathbf{q}}} + \hat{\mathbf{C}}\dot{\hat{\mathbf{q}}} + \hat{\mathbf{K}}\hat{\mathbf{q}} + \hat{\mathbf{f}}_{\mathrm{d}} = \hat{\mathbf{f}}_{\mathrm{ext}}, \tag{4.1a}$$

$$\hat{\mathbf{q}} = [\hat{\theta}_1, \hat{\theta}_2, \hat{\theta}_3]^T. \tag{4.1b}$$

The mass matrix $\hat{\mathbf{M}}$, damping matrix $\hat{\mathbf{C}}$, and stiffness matrix $\hat{\mathbf{K}}$ are

$$\hat{\mathbf{M}} = \text{diag}(I_1, I_2, I_3), \tag{4.2a}$$

$$\hat{\mathbf{C}} = \text{diag}(c_{\hat{\theta}1}, c_{\hat{\theta}2}, c_{\hat{\theta}3}), \tag{4.2b}$$

$$\hat{\mathbf{K}} = \text{diag}(k_{\hat{\theta}1}, k_{\hat{\theta}2}, k_{\hat{\theta}3}). \tag{4.2c}$$

The vector $\hat{\mathbf{f}}_\text{d}$ contains the torques from the dynamically changing mesh force $F_{1,2}$. The vector $\hat{\mathbf{f}}_\text{ext}$ represents forcing due to the applied torque. They are given by

$$\hat{\mathbf{f}}_\text{d} = \hat{\mathbf{R}}^T \hat{\mathbf{f}}, \tag{4.3a}$$

$$\hat{\mathbf{R}} = \begin{bmatrix} r_{11} & r_{12} & 0 \\ 0 & -r_{21} & -r_{22} \end{bmatrix} \tag{4.3b}$$

$$\hat{\mathbf{f}} = [F_1, F_2]^T, \tag{4.3c}$$

$$\hat{\mathbf{f}}_\text{ext} = [T_1, 0, T_3]^T. \tag{4.3d}$$

The vector of mesh deflection is defined as $\hat{\mathbf{x}} = [\hat{x}_1, \hat{x}_2]^T$, where $\hat{x}_i$ denotes the mesh deflection for the ith mesh. It is given by

$$\hat{\mathbf{x}} = \hat{\mathbf{R}}\hat{\mathbf{q}}. \tag{4.4}$$

The system has three vibration modes. The first mode is a low frequency model. The first and third gear have in-phase vibrations, while the second gear vibrates out-of-phase. The strain energy is mainly concentrated in the torsional stiffness. The second mode is an

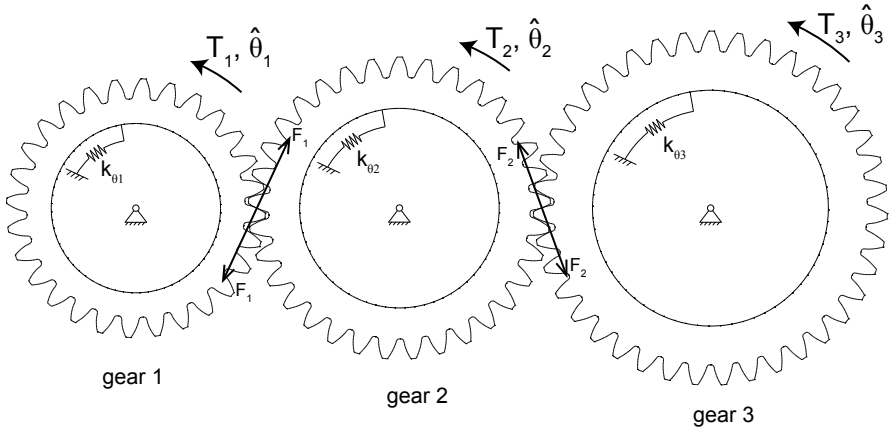

Figure 4.1: Schematic of the idler gear system

out-of-phase mode: the first and third gear have out-of-phase motions, while the second gear have small amplitude deflection. The third mode is a in-phase mode where all the three gears have in-phase motions.

4.2.2 Planetary Gear System

Figure 4.2 shows a schematic of the planetary gear system. The system has 3N+9 degrees of freedom, where N is the number of planets. The stationary (inertial) basis is $\{\mathbf{E}_1, \mathbf{E}_2, \mathbf{E}_3\}$. The rotating $\{\mathbf{e}_1, \mathbf{e}_2, \mathbf{e}_3\}$ basis is attached to the kinematics of the carrier, and rotates with constant carrier angular speed Ω_c. The translational deflections x_j and y_j $(j = c, r, s)$ for the central members are defined in the Cartesian coordinates . The planets are located at fixed angles ψ_i $(i = 1, 2, ..., N)$ where $\psi_1 = 0$. The rotating $\{\mathbf{e}_1^i, \mathbf{e}_2^i, \mathbf{e}_3^i\}$ bases defined by rotating $\{\mathbf{e}_1, \mathbf{e}_2, \mathbf{e}_3\}$ of angle ψ_i about $\mathbf{e}_3 = \mathbf{e}_3^i$ are used for the planets. The planet translations are defined using radial ζ_i and tangential η_i coordinates. The rotational coordinates are θ_n $(n = c, r, s, 1, 2, ..., N)$. The tooth contact pressure angle for the sun-planet mesh and ring-planet mesh are α_s and α_r, respectively. The ring gear and sun gear

have base radii r_r and r_s. The base radii for the planet gears is determined by which central component it is engaged with. They are r_{ps} for the contact with the sun gear, and r_{pr} for the contact with the ring gear. r_c is the radius for the circle passing through the planet centers. The gears have masses m_n and moment of inertia I_n. The central components are supported by translational (k_j) and rotational ($k_{j\theta}$) stiffnesses that represent the compliance in the supporting bearings and shaft structures. The planet gears are supported by translational stiffnesses k_{pi}. The corresponding damping elements are c_j, $c_{j\theta}$, and c_{pi}, respectively. T_j are the applied torques on the central components. F_{si} and F_{ri} denote the periodically changing dynamic mesh force for sun-planet mesh and ring-planet mesh, respectively. The matrix equation of motion is

$$\mathbf{M}\ddot{\mathbf{q}} + \mathbf{C}\dot{\mathbf{q}} + \Omega_c\mathbf{G}\dot{\mathbf{q}} + (\mathbf{K}_b - \Omega_c^2\mathbf{K}_\Omega)\mathbf{q} + \mathbf{f}_\mathrm{d} = \mathbf{f}_\mathrm{ext}, \tag{4.5a}$$

$$\hat{\mathbf{q}} = [x_c, y_c, \theta_c, x_r, y_r, \theta_r, x_s, y_s, \theta_s, \zeta_1, \eta_1, \theta_1, ..., \zeta_N, \eta_N, \theta_N]^T. \tag{4.5b}$$

The mass matrix $\mathbf{M}$, damping matrix $\mathbf{C}$, gyroscopic matrix $\mathbf{G}$, bearing stiffness matrix $\mathbf{K}_b$ and centripetal matrix $\mathbf{K}_\Omega$ are given in Appendix A. The vector $\mathbf{f}_\mathrm{d}$ contains the forces and torques from the dynamically changing mesh force F_{si} and F_{ri}. It is given by

$$\mathbf{f}_\mathrm{d} = \mathbf{R}^T\mathbf{f}, \tag{4.6a}$$

$$\mathbf{f} = [F_{s1}, F_{r1}, ..., F_{sN}, F_{rN}]^T. \tag{4.6b}$$

The transformation matrix $\mathbf{R}$ is given in Appendix B. The vector $\mathbf{f}_{\text{ext}}$ represents forcing due to the applied torque. It is given by

$$\mathbf{f}_{\text{ext}} = [\mathbf{T}_c, \mathbf{T}_r, \mathbf{T}_s, \mathbf{0}, ..., \mathbf{0}]^T, \tag{4.7a}$$

$$\mathbf{T}_j = [0, 0, T_j]^T. \tag{4.7b}$$

The vector of mesh deflection is defined as $\mathbf{x} = [x_{s1}, x_{r1}, ..., x_{sN}, x_{rN}]^T$. It is given by

$$\mathbf{x} = \mathbf{R}\mathbf{q}. \tag{4.8}$$

Planetary gear systems have three types of vibration modes [45]: translational modes, rotational modes and planet modes. Translational modes have purely translations (no rotations) of the central components. Rotational modes have purely rotations (no translations) of the central components. Planet modes have no motion of the central components; all planets have identical deflections. More details about the vibration modes of planetary gears can be found in the references.

For both the idler gear and planetary gear systems, the dynamic mesh forces are the key quantities driving the vibration. The accuracy of the model depends on the accuracy of these dynamic mesh forces, which depends on the gear motions and changes as the gears rotate. The dynamic mesh force is affected by tooth modifications, applied torque, and contact loss nonlinearities near resonances. For multi-mesh systems, the dynamic mesh force is also affected by the interactions between different tooth meshes. The dynamic mesh force

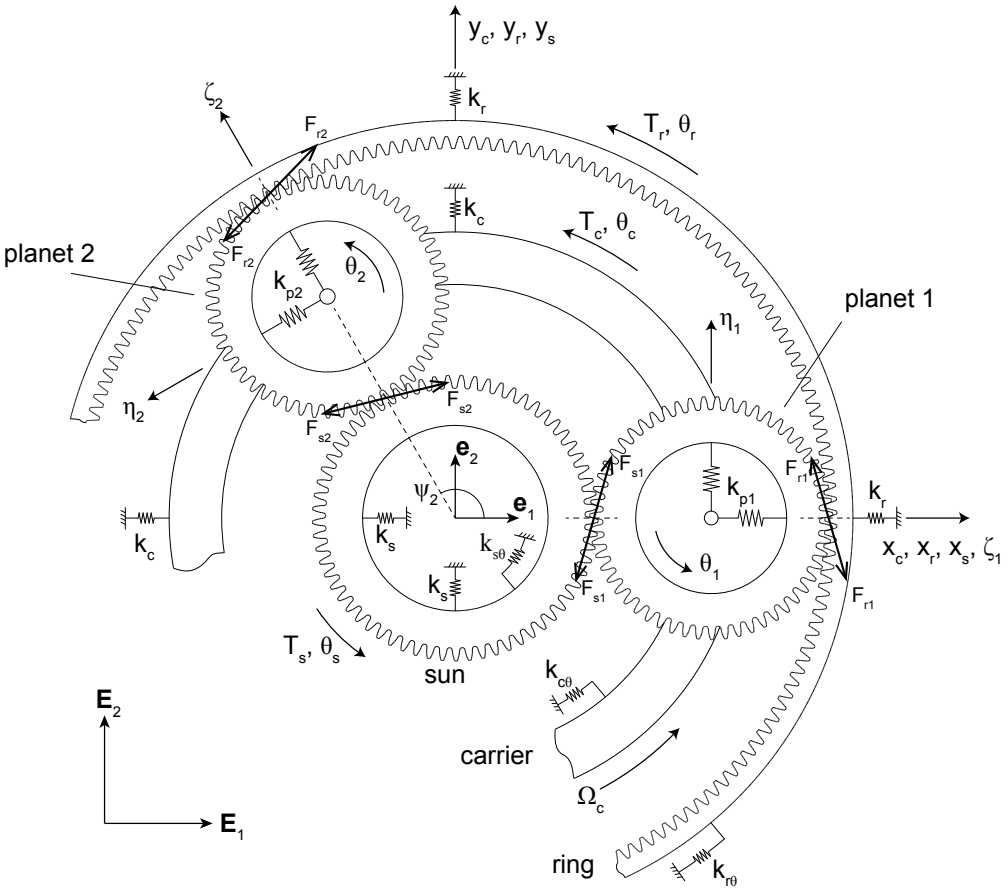

Figure 4.2: Schematic of the planetary gear system

for single-mesh spur gear pairs is calculated using a force-deflection function [14, 3]. In this work, the dynamic mesh forces for the tooth meshes are calculated using the corresponding force-deflection function, as will be discussed subsequently.

4.3 Finite Element Calculations of Force-Deflection Function

4.3.1 Key Assumption

The key assumption in this work is the same as in Ref. [3] for spur gear pairs. We briefly describe the assumption below.

The dynamic motions of a gear is classified into two types: the translational and rotational vibrations of the gear as a rigid body as define in Eqs. 4.1 and 4.5, and the elastic deformations in the gear teeth and blank as shown in Fig. 5.2. The translational and rotational vibrations are usually at the the gear mesh frequency and its first several harmonics. The vibrations in the elastic gear teeth and blank (Fig. 5.2) occur at frequencies that are generally much higher than the gear mesh frequency and the natural frequencies for translational and rotational vibrations associated with $\mathbf{q}$. We assume that under dynamic conditions, the elastic gear body achieve an "instantaneous steady state" so rapidly that there is negligible distinction between this "instantaneous steady state" and the state of elastic tooth and gear blank deformations that would occur if the mating gear teeth were loaded statically with the same contact force at the same point in a mesh cycle. More details

can be found in Ref. [3].

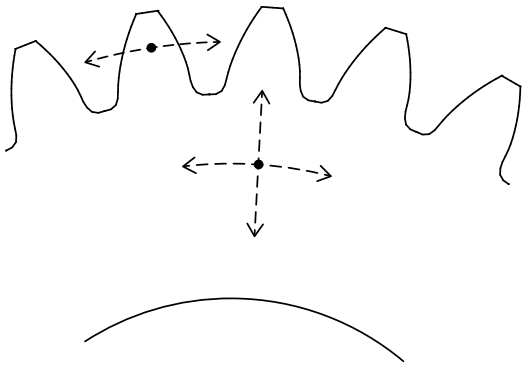

Figure 4.3: Schematic of the elastic deformation in the gear teeth and blank from Ref. [3]. The black circles represent arbitrary material points on the elastic gear body.

With this assumption, the mesh force calculated in advance under static condition for a given mesh deflection and position within a mesh cycle can be used in dynamic analysis. Additionally, the dynamic contact stress, tooth root strains, and other parameters are also uniquely determined from the static deformed configuration.

4.3.2 Force-Deflection Function

The force-deflection function (FDF) is the crucial quantity to implement the foregoing assumption. The FDF is defined as the relationship between mesh force and mesh deflection at each position within the mesh cycle. There are multiple FDFs for multi-mesh systems, one for each tooth mesh. They are calculated statically using computational methods. The FDFs are generated prior to dynamic analysis, and then used in the numerical integration of Eqs. 4.1 and 4.5 to calculate the instantaneous dynamic mesh force $\hat{\mathbf{f}}$ and $\mathbf{f}$ based on the corresponding instantaneous mesh cycle position and mesh deflection. The FDFs for multi-mesh systems does not necessarily need to be generated individually from gear pair

analyses, as will be discussed subsequently.

Figure 4.4 shows the two FDFs for the three gear idler system. The FDFs are generated by assembling a series of static results through a range of interesting of applied torque (i.e., mesh force) and many positions throughout a mesh cycle. The phase difference between the meshes is defined by the positions within a mesh cycle for which the contact location is at the pitch point, as shown in Fig. 4.4. For static gear chain analyses, this phase difference is naturally incorporated for given gear center positions. Alternatively, one can generate the FDF for each tooth mesh individually from a several gear pair analyses, and combine the FDFs together. In that case, the phase difference need to be included manually.

Similarly, the FDFs for the planetary gears are generated through static analyses. A one planet system is used in these static analyses, as shown in Fig. 4.5(a). The carrier, sun gear, ring translations, and planet translations are constrained. A torque is applied on the ring gear, and the rotational deflections for the ring and planet gears are calculated statically. The mesh deflections for the sun-planet and ring-planet meshes are calculated using Eq. 4.8. The mesh forces are also calculated from the static analyses. The FDFs are assembled by repeating this process, for many applied torques cross the range of interest, at many points throughout a mesh cycle. The FDFs for the sun-planet and ring-planet meshes associated with the planet are generate simultaneously. The phasing between these two meshes are incorporated naturally due to the geometry of the gears. The FDFs for the meshes with the remaining planets are generated by applying the proper phase, which is uniquely determined by the number of gear teeth and planet position ψ_i, to the FDF from the first planet.

The full-planet system (shown in Fig. 4.5(b)) is not used in these static analyses be-

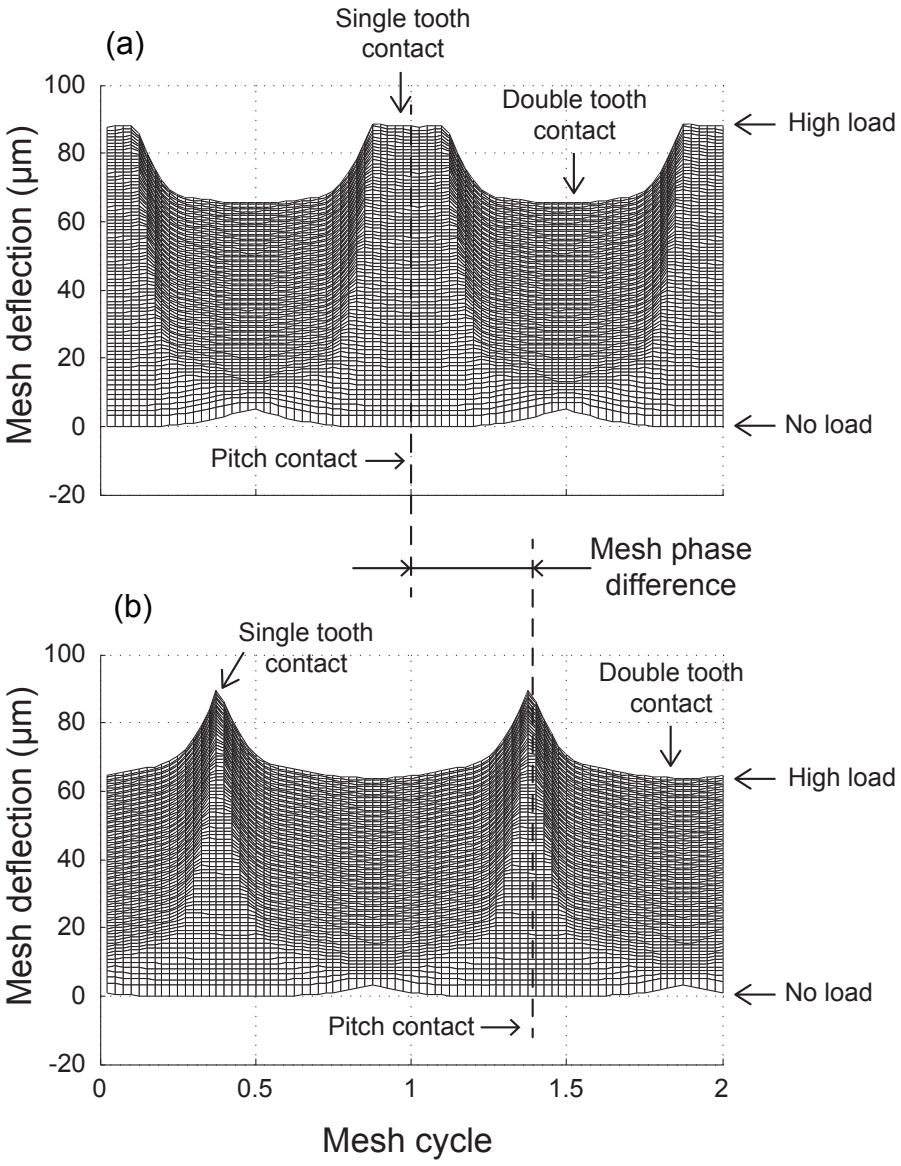

Figure 4.4: Finite element calculation of the force-deflection function for the (a) first and (b) second mesh of the idler gear system. The phase of the force-deflection function for the second mesh is shifted for better graphic presentation.

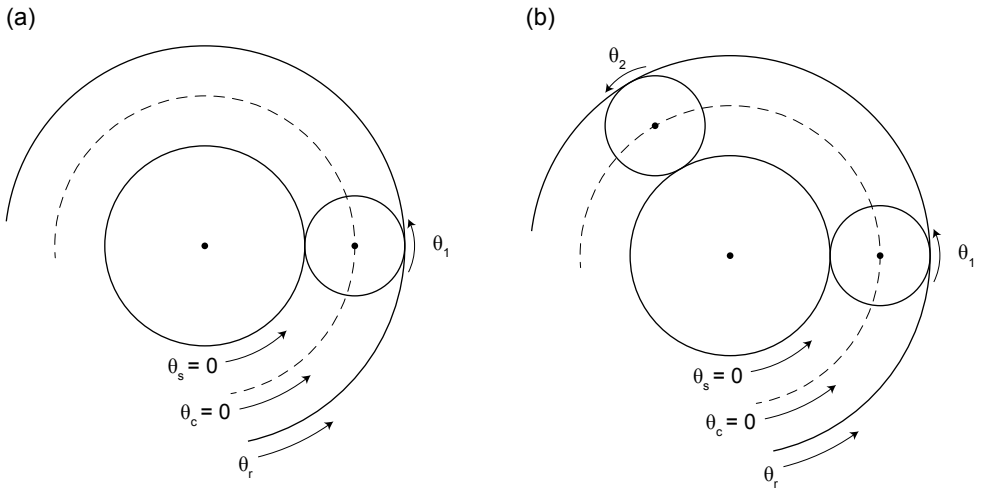

Figure 4.5: Schematic of the computational model with (a) single and (b) multiple planets that used in the static analyses for the planetary gear system.

cause it may not give accurate results at low torque regions when the gears have tooth profile modifications. The mesh deflections for the gear under nearly vanishing load is meaningfully large due to tooth profile modifications. For full planetary gears, the mesh deflections associated with different planets will have interactions. In order to better demonstrate the problem, we compare the quantities $\delta_i = \delta_{si} + \delta_{ri}$ $(i = 1, 2, ..., N)$, where δ_{si} and δ_{ri} are the no load mesh deflections at planet i due to tooth profile modifications. For different i, δ_i does not necessarily to be the same due planet phasing. When analyzing the full planetary gear system statically under a small load, only the planet with smallest δ_i will have tooth engagement; the rotational deflection for other planets can not be accurately captured. This inaccuracy is more significant with larger tooth profile modifications. The one planet system is also preferred for unmodified gears because it is more efficient. Additionally, it requires less storage resources.

The accuracy of the analytical model depends on the accuracy of the dynamic mesh

force calculation, which is further determined by the underlying computational model for static analyses. In this work, we use a finite element/contact mechanics (FE/CM) software Calyx for the static computational analyses to generate the FDFs. Alternatively, the FDFs can be generates using other finite element formulations or commercial softwares.

The FE/CM model developed by Vijayakar and implemented in Calyx is for contact problems in multi-body dynamics. This model combines an analytical solution for the tooth contact, and conventional finite element solutions for the elastic gear teeth and blank. The micro-geometry on the tooth contact surface due to tooth profile and lead modifications are precisely modeled using Hermite polynomial shape functions. The model has been shown to accurately and efficiently predict dynamic response in single-mesh gear pairs [108, 118, 109, 135] and planetary gears [107, 115, 116, 51]. The FDF generated using the FE/CM model is shown to work well for single-mesh spur gear pairs [3]. More details can be found in the references.

As discussed in Sec. 4.3.1, the total mesh force under dynamic condition is approximated to the corresponding static force at the same position within the mesh cycle with the same mesh deflection. The FDFs generated from static analyses are used in dynamic analyses to compute the instantaneous dynamic mesh force. When generating the FDFs, the input quantity is the applied torque (i.e., mesh force), and the mesh deflection is one of the output quantities. In the dynamic analytical calculations, however, the mesh deflection becomes the input and the mesh force is the output.

4.4 Calculation of Dynamic Response

4.4.1 Gear Translational and Rotational Vibrations

The gear translational and rotational vibrations are calculated using the analytical formulations in Eqs. 4.1 and 4.5. At each instant, the dynamic mesh force for each tooth contact pair is calculated using the corresponding FDF introduced in Sec. 5.3. Two quantities are required for each mesh force calculation: the point within a mesh cycle where the gears currently are and the dynamic mesh deflection. The mesh position for each tooth mesh is uniquely determined by kinematics and mesh phasing. The mesh deflections are calculated using the gear translational and rotational deflections, as shown in Eqs. 4.4 and 4.8. The dynamic mesh force is then calculated by applying linear interpolation to the FDF at the corresponding mesh cycle position and mesh deflection. Numerical integration is performed for a single time step. This process repeats at the next time instant, and continues as long as desired (i.e., steady state is reached).

4.4.2 Elastic Deformation and Stress in the Gear Teeth

The dynamic elastic deformation and stresses in the gear teeth and gear blank are calculated through post-processing. In this work, we calculate the dynamic tooth root strains for multi-mesh systems as an example.

The dynamic tooth root strains at a specific location in the tooth root region is calculated using the strain-deflection function (SDF), which is defined as the relationship between the

tooth root strain and mesh deflection over the mesh cycles. The SDF is analogous to the FDF. The SDF is generated through the same static results from which the FDFs are generated; there is no additional numerical simulations. Figure 5.6 shows the SDF for the planetary gears calculated at a point on the surface of the sun gear. The point is in the middle between two adjacent teeth. The dynamic tooth root strain is calculated using this SDF, together with the dynamic mesh deflection obtained from Sec. 4.4.1. For multi-mesh systems, the tooth root strain is caused by multiple mesh forces. The strain due to each mesh force is calculated individually using the corresponding dynamic mesh deflection and SDF. The position of the gear tooth mesh in the SDF is shifted based on the planet location ψ_i. The dynamic tooth tooth root strain is calculated by adding up the strains from each tooth mesh. This strain calculation is not part of the solution method. It can be processed entirely in post-processing based on the dynamic response from Sec. 4.4.1. We emphasize that there is no additional numerical simulations for the SDF calculation; it is generated from the same static results in Sec. 5.3. One only has to store the necessary outputs from the static results (to get the SDF, for example) and use the static results to obtain the corresponding dynamic values. Other dynamic quantities, tooth contact pressure, for example, can be calculated using the same method.

4.4.3 Computational Efficiency

The proposed HAC method is computationally efficient. There are three steps: static FE/CM simulations, analytical dynamic calculations, and post-processing. The simulation time for the static simulations depends on the underlying software. These static analysis at

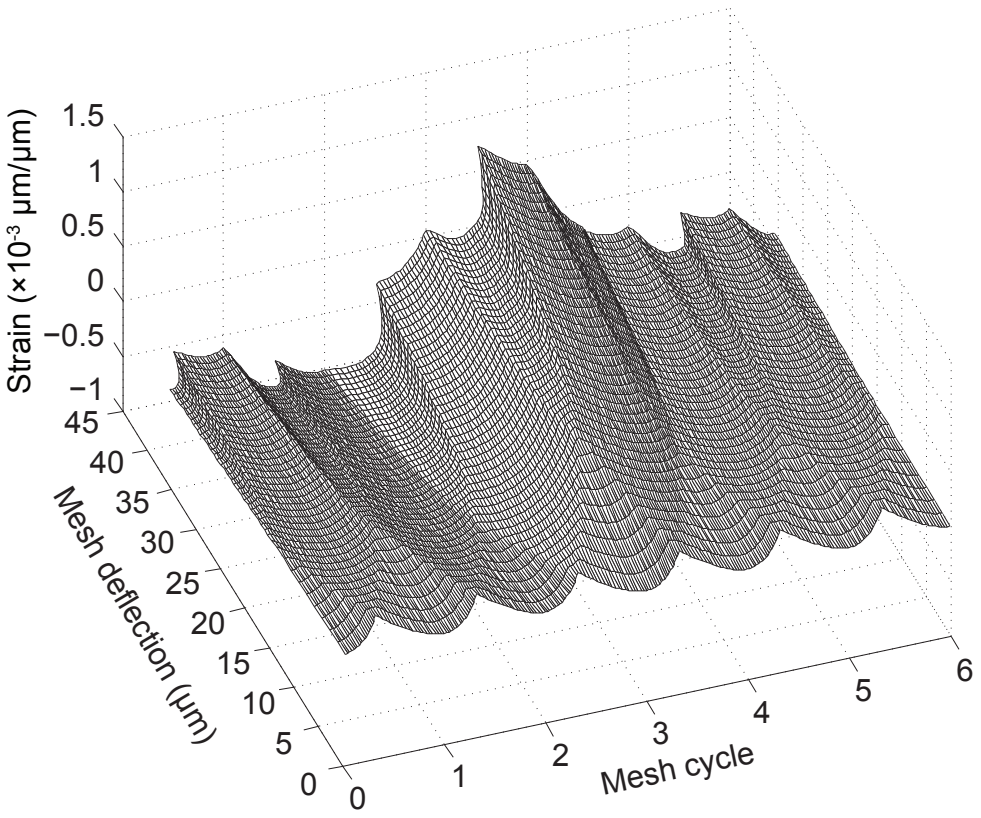

Figure 4.6: Finite element calculation of the strain-deflection function for the planetary gears. The strains are calculated in the middle between two adjacent teeth on the sun gear.

each torque are much faster than dynamic analysis. At each torque, the gears are analyzed for only one mesh cycle. For multi-mesh systems, the static simulations for each tooth mesh can be proceeded simultaneously. Additionally, these static analyses are performed only once for given tooth modifications. For the static results at each torque, all the necessary informations of the system over one mesh cycle are saved, including the gear rotational deflections, mesh forces, tooth root strains and stresses at each node, and any other quantity of interest. Of these static results, only the FDF is used for the dynamic solution. Other quantities are used to calculate the corresponding dynamic values in post-processing, like the tooth root strains discussed above.

The simulation time for analytical dynamic calculations are as fast as conventional lumped parameter models. For the idler gear system, it take about 7×10^{-3} seconds on a conventional desktop for a mesh cycle using the HAC method, which is about 5000 times faster than the FE/CM simulation using a three-dimensional model. For the planetary gears, it takes about 0.5 seconds for each mesh cycle using the HAC method, which is slower than the idler gear system. This is because planetary gear systems have more degrees of freedom. Additionally, there are more tooth meshes in the planetary gears, which requires more times using the FDF within each time step. The simulation time for the planetary gear system is about 100 times faster than the two-dimensional FE/CM model.

4.5 Numerical Results

The proceeding section compares the HAC prediction of dynamic response for multi-mesh systems with FE/CM calculations. Both the idler gear and planetary gear systems are studied to validate the HAC method.

4.5.1 Idler Gear Systems

The parameters for the idler gear system are given in Table. 4.1. The gears have asymmetric teeth. The pressure angles for the first and second meshes are 25° and 20°, respectively. The gears are analyzed dynamically over a wide range of speed and torque combinations. At each speed, the gears are analyzed over a number of mesh cycles so that the transient responses are diminished and the steady state solutions are recorded. Fig. 4.7 shows HAC calculation of oscillating root mean square (RMS) component of the dynamic mesh deflection for the idler gear system The applied torque is 300 N-m on gear 1. Good agreement is seen between between the HAC and FE/CM calculations over a wide range of speed, including resonant and off-resonant gear speeds. The resonance locations are accurately predicted by the HAC model, although these resonances have different types, as shown in Fig. 4.7. The resonances near $f_m/f_n = 1/2$ and $f_m/f_n = 1/3$ are super-harmonic resonances where the second and third harmonics of mesh frequency cause resonance. The resonances near $f_m/f_n = 2$ are sub-harmonic resonances. The classical softening type nonlinearities are accurately predicted by the HAC model, as seen the double-valued regions near 1800 Hz and 3400 Hz. The jump-up and jump-down frequencies are also accurately predicted.

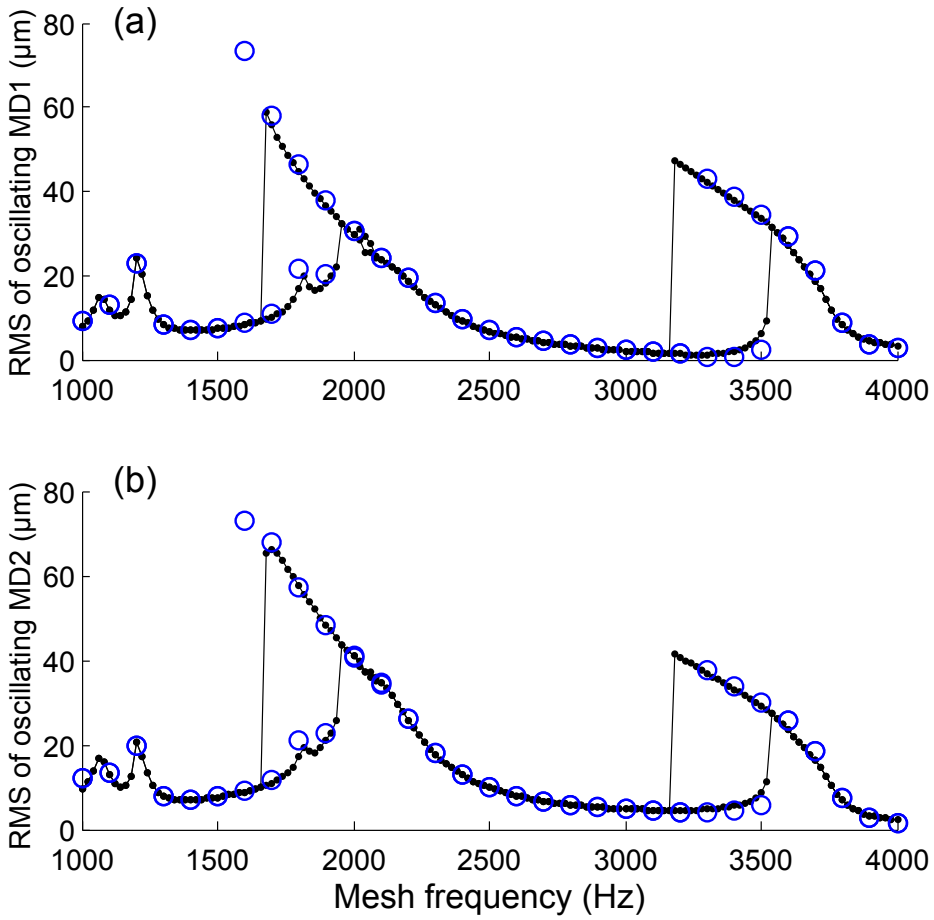

Figure 4.7: Oscillating (RMS) components of the dynamic mesh deflection for the (a) first and (b) second tooth mesh of the idler gear system. The applied torque is 300 N-m on gear 1. The black dots and blue circles denote the HAC calculations and FE/CM calculations, respectively.

Table 4.1: Parameters for the idler gear system.

	Gear 1	Gear 2	Gear 3
Number of Teeth	28	33	39
Outer Diameter (mm)	149.925	174.925	204.925
Root Diameter (mm)	126.4	151.4	181.4
Module (mm)	5		
Circular Tooth Thickness (mm)	7.6375		
Face Width (mm)	9		
Pressure Angle (deg)	20/25		
Tooth Profile Modification	Quadratic		
Tip Relief (μm)	15		
Start Roll Angle (deg)	22.9/28.54		
Lead crowning (μm)	12		
Density (kg/m^3)	7.85×10^3		
Young's Modulus (GPa)	201.5		

Figure 4.8 shows the HAC calculation of dynamic mesh deflection and mesh force for the idler gears compared with FE/CM calculations. The mesh frequency is 3400 Hz near resonance on the upper branch, as shown in Fig. 4.7. Excellent agreement is seen between the two results, including the amplitude and phase of the curves. At this speed, high amplitude vibrations are excited and contact loss occur, as shown the zero mesh force regions in Figs. 4.8 (c) and (d). The dynamic mesh deflection is smaller than the no load mesh deflections in these regions, as can be seen in Figs. 4.8 (a) and (b). This strong nonlinear behavior is accurately captured by the HAC method. Similar good agreements are seen at other speeds, which is not shown.

4.5.2 Planetary Gear Systems

The planetary gears are analyzed to further validate the HAC method. The parameters for the planetary gears are given in Table 4.2. Both the gears with or without tooth profile

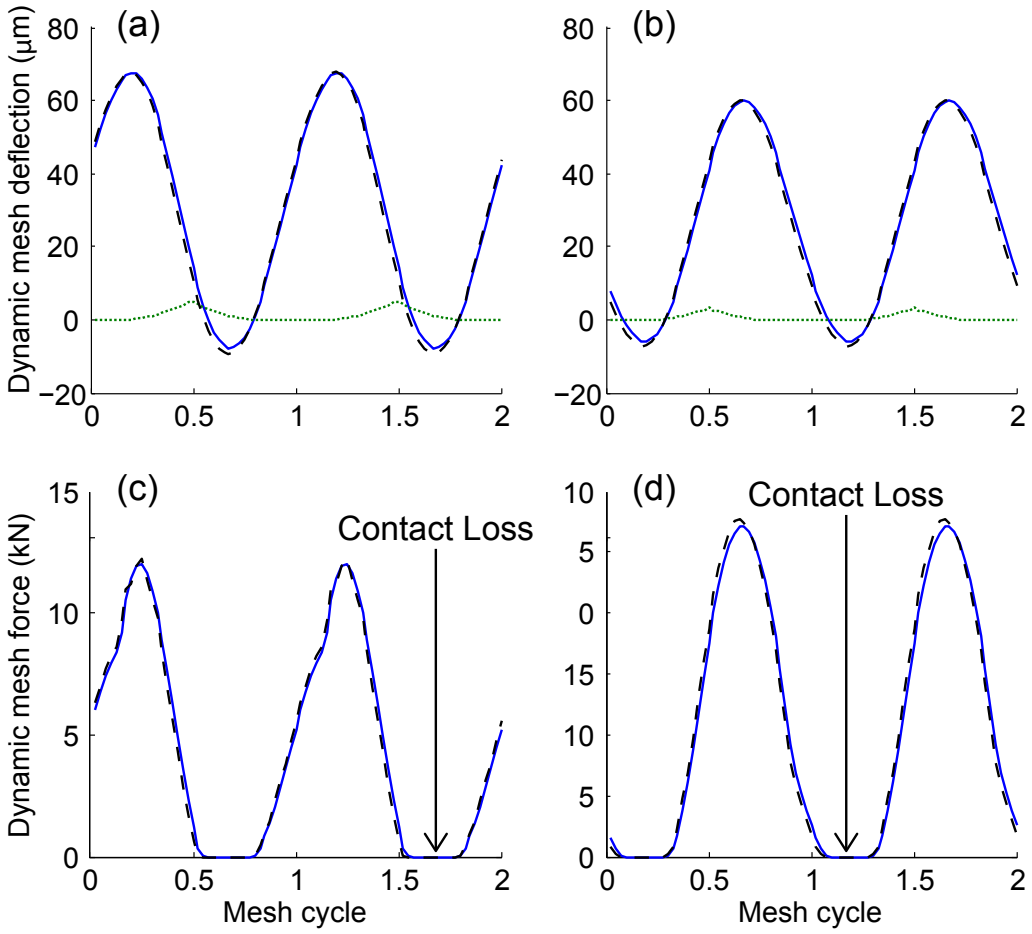

Figure 4.8: HAC calculation of (a,b) dynamic mesh deflection and (c,d) dynamic mesh force compared with FE/CM results for the idler gear system at 3400 Hz and 300 N-m torque at gear 1. The results for the first and second meshes are shown in Figs. (a,c) and (b,d), respectively. The solid blue lines and dashed black lines denote the HAC calculations and FE/CM calculations, respectively. The dotted green lines in Figs. (a) and (b) denote the no load mesh deflections.

modifications are analyzed. The ring gear has zero speed, and is fixed to the global reference frame. The carrier rotation is fixed to kinematics. The system can have either three, four, or five equally spaced planet gears, and these different cases are all studied. The phase difference between the planets are determined by the number of planets, as shown in Fig. 4.9. For the systems with three or four planets, there is a constant phase difference between adjacent two planets. For the five planet system, however, all the planets have the same phase. The dynamic response of the planetary gear system is highly affected by this phase difference between planets, as will be discussed in the proceeding section.

Table 4.2: Parameters for the planetary gear system.

	Ring gear	Sun gear	Planet gear
Number of Teeth	175	65	55
Tip Diameter (mm)	278.9	107.8	91.69
Root Diameter (mm)	288	97.91	81.78
Face Width (mm)	10	8	10
Lumped mass (kg)	0	1.8	0.9
Lumped inertia (kg$\times m^2$)	0	2.1×10^3	0.8×10^3
Module (mm)	1.609		
Circular Tooth Thickness (mm)	2		
Pressure Angle (deg)	15.97		
Tooth Profile Modification	Quadratic		
Tip Relief (μm)	15		
Start Roll Angle (deg)	16		
Density (kg/m^3)	7.595×10^3		
Young's Modulus (GPa)	207.17		

Figure 4.10 shows the HAC calculation of the oscillating (RMS) component of dynamic mesh deflection for the sun-planet mesh for the three-planet system compared with FE/CM results. Both the results with (Fig. 4.10(a)) and without (Fig. 4.10(b)) tooth profile modifications are compared. Good agreement between the two solutions continues. The resonance locations and peak amplitude are drastically different with/without tooth profile modifications, and they are all accurately captured by the HAC method. Unlike the three

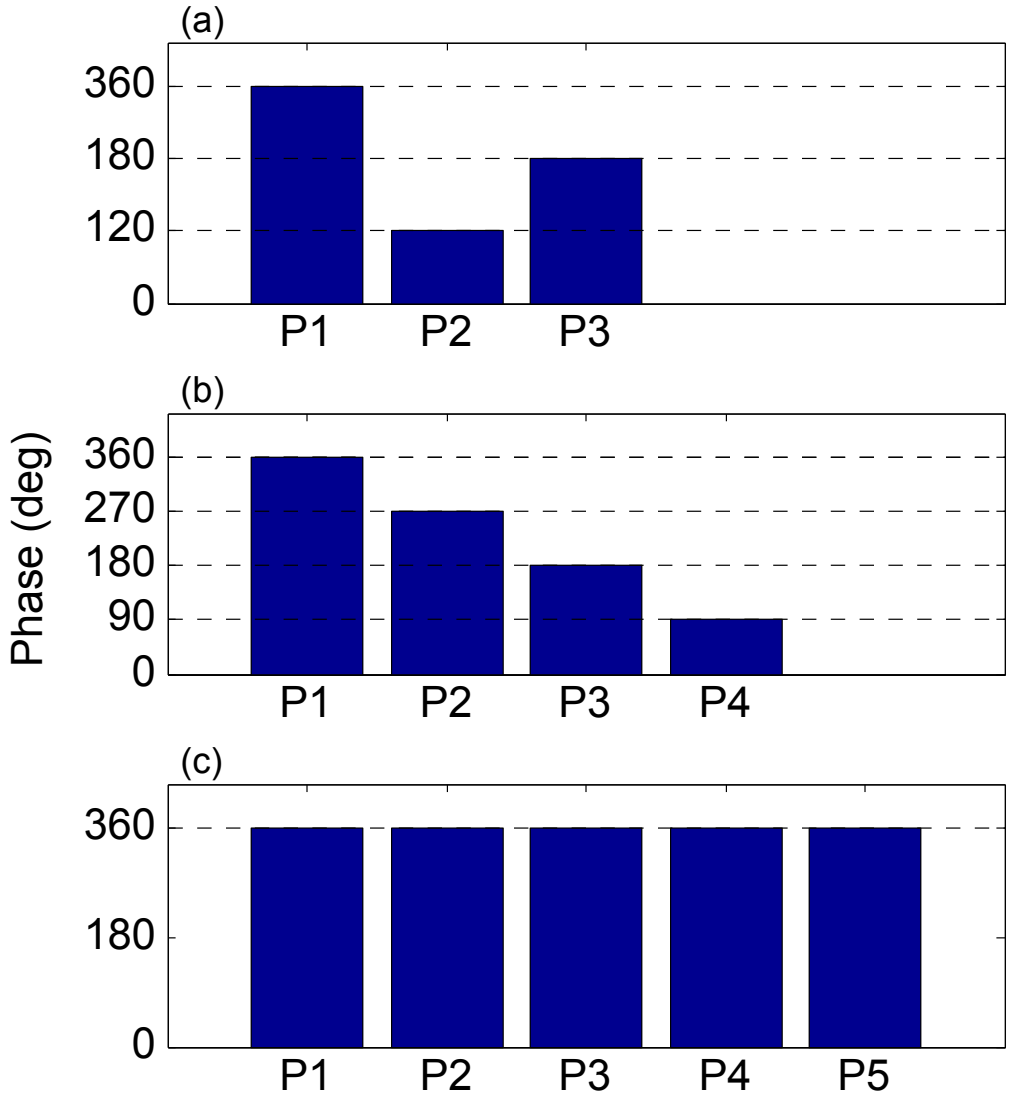

Figure 4.9: Planet phasing for the (a) three, (b) four, and (c) five planet systems.

gear system discussed in Sec. 4.5.1, the nonlinear behavior in this system is weak; same results are obtained from the increasing and decreasing speed sweeps. This is because there is a phase difference between the meshes for the planets (shown in Fig. 4.9(a)), and the vibration of the system is weakened. Good agreements are also observed for the ring-planet mesh, and all the components in $\mathbf{q}$, which are not shown. Similar good agreement is observed for the four degree-of-freedom system.

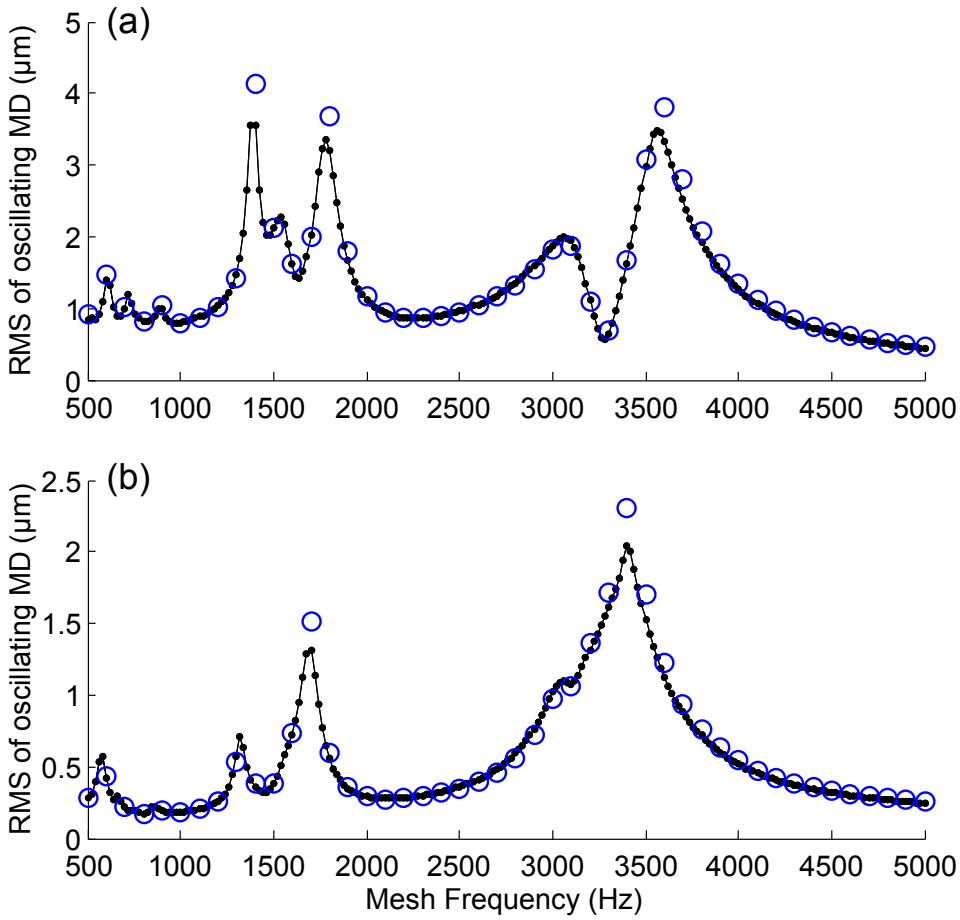

Figure 4.10: HAC calculation of oscillating (RMS) component of the dynamic mesh deflection of the sun-planet mesh for the three planet system compared with FE/CM results. The applied torque is 200 N-m on the sun gear. Both the gears (a) without and (b) with tooth profile modifications are compared. The black dots and blue circles denote the HAC calculations and FE/CM calculations, respectively.

Figure 4.11 shows the HAC calculation of mesh deflection for the three-planet system

compared with FE/CM calculations. Good agreement is observed between the two solutions. The mesh deflection for each planet have the same vibration amplitude, but they have a phase difference. This phase difference is the same as that shown in Fig. 4.9(a), as expected.

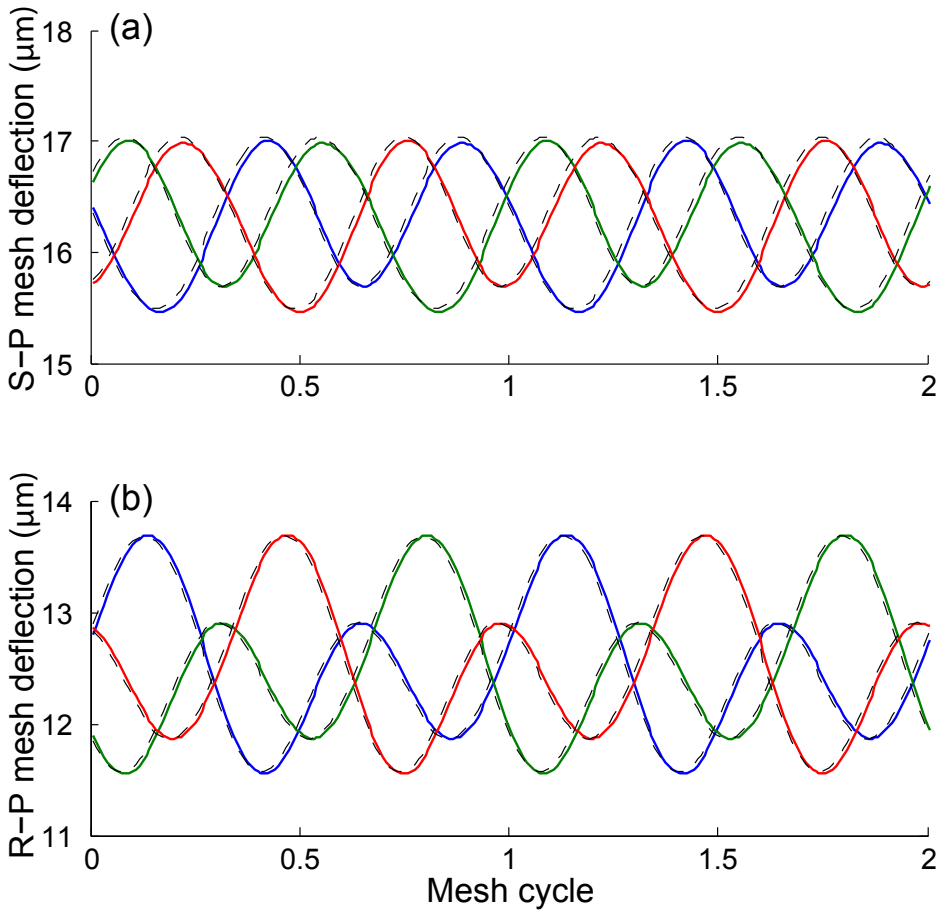

Figure 4.11: HAC calculation of dynamic mesh deflection for the (a) sun-planet and (b) ring-planet mesh for the three-planet system at 1600 Hz mesh frequency compared with FE/CM results. The applied torque is 200 N-m. The solid blue lines, solid green lines, and solid red lines denote the HAC calculations for the first, second and third planet, respectively. The corresponding FE/CM results are shown in dotted black lines.

Figure 4.12 compares the oscillating (RMS) component of dynamic mesh deflection for the sun-planet mesh for the five-planet system from the HAC and FE/CM calculations. Good agreement continues. In contrast to the systems with three (Fig. 4.10) or four (now shown) planets, strong nonlinear behavior is observed for the five planet system, as shown

the double-valued regions in Fig. 4.12. This is because the planets have the same phase (shown in Fig. 4.9), and they move simultaneously, causing large amplitude vibrations near resonances. The modified gears (Fig. 4.12(b)) have a smaller double-valued region. This is because the modified gears have smaller excitations. An additional resonance is observed near 2800 Hz for the modified gears, as shown in Fig. 4.12(b). The nonlinear behaviors with and without tooth modifications are drastically different, and they are all accurately predicted by the HAC method.

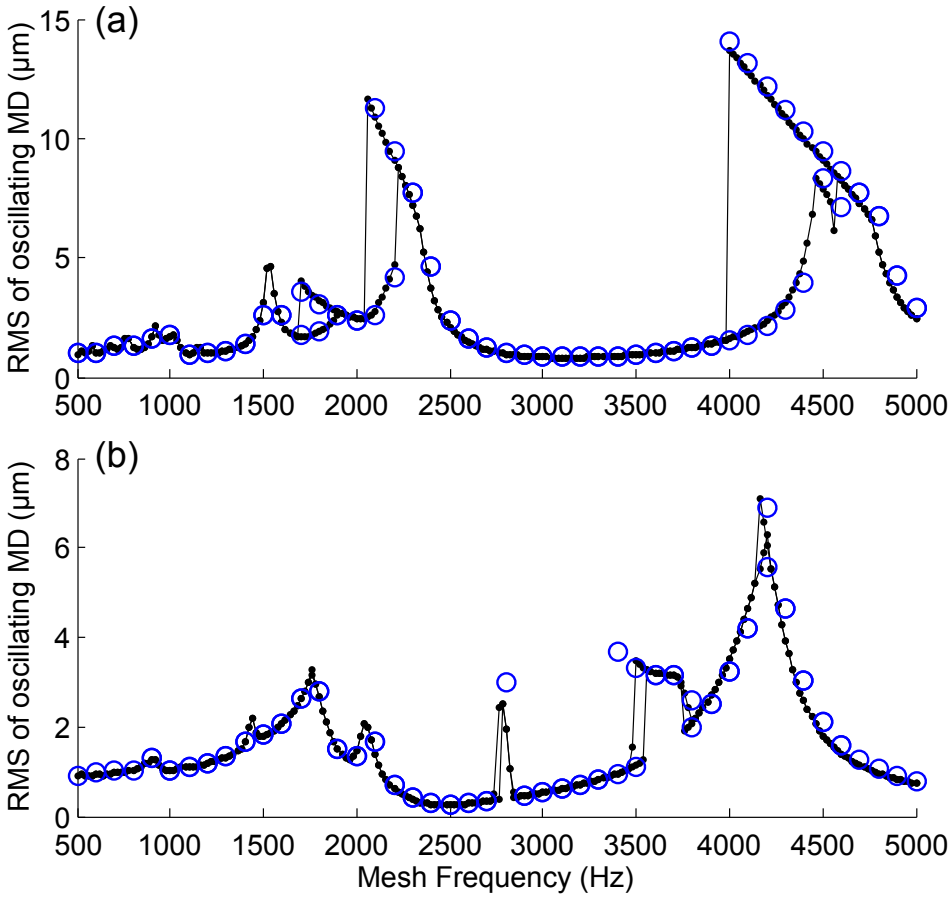

Figure 4.12: HAC calculation of oscillating (RMS) component of the dynamic mesh deflection of the sun-planet mesh for the five planet system compared with FE/CM results. The applied torque is 200 N-m on the sun gear. Both the gears (a) without and (b) with tooth profile modifications are compared. The black dots and blue circles denote the HAC calculations and FE/CM calculations, respectively.

Figure 4.13 compares the dynamic mesh deflection for the five-planet system calculated from the HAC and FE/CM models. In contrast to the solutions in Fig. 4.11 for the three gear systems, identical solutions for different planets are observed for the five-planet system. This is because the planets are equally spaced on the carrier, and they have in-phase excitations, so that they will have in-phase motions. Identical solutions for the planets are also obtained from the FE/CM model, as shown the dashed lines in Fig. 4.13. The results show good agreement between the two solutions from the HAC and FE/CM models.

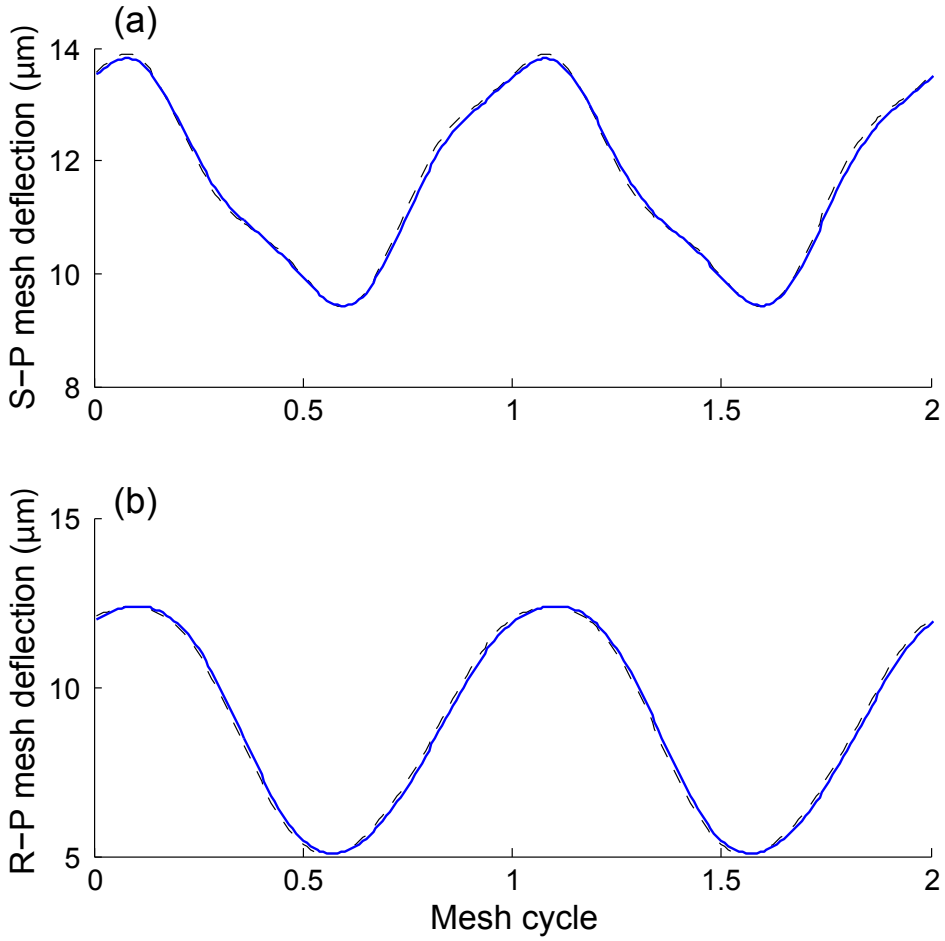

Figure 4.13: HAC calculation of dynamic mesh deflection for the (a) sun-planet and (b) ring-planet mesh for the five-planet system at 1600 Hz mesh frequency compared with FE/CM results. The applied torque is 200 N-m. The solid blue lines and dashed black lines denote denote the HAC calculations and FE/CM calculations, respectively.

Figure 4.14 shows the dominant mode of the planetary gears at 1600 Hz calculated from the HAC method compared with FE/CM results. Good agreement is observed for both the three-planet and five-planet systems. For the three-planet system, the central components only have pure translations. In other words, the carrier, ring, and sun gears do not have rotational vibrations. This mode shape is defined as the translational mode [45]. For the five planet system, as the planet gears are equally spaced on the carrier and they have in-phase motions, the total force on the central component diminishes; they only have rotational vibrations. This mode shape is defined as the rotational mode [45]. The dynamic response of the gears are highly affected by the phasing features of the system, and they are all accurately predicted by the HAC model.

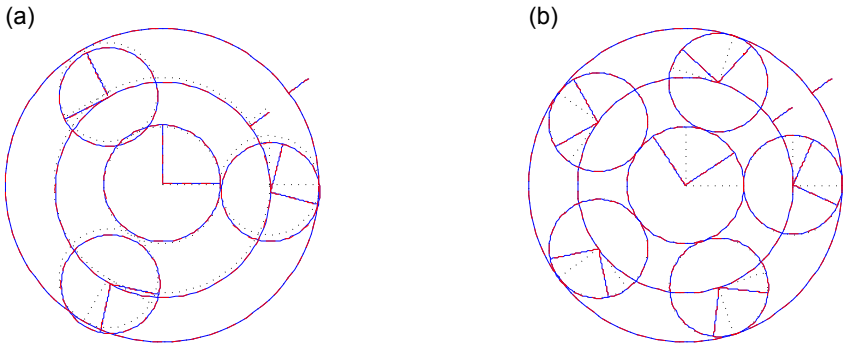

Figure 4.14: Dominate mode of the (a) three planet and (b) five planet system at 1600 Hz mesh frequency. The applied torque is 200 N-m on the sun gear. The solid blue lines, dashed red lines, and dotted black lines denote HAC calculations, FE/CM calculations, and undeformed position, respectively.

Figure 4.15 compares the dynamic tooth root strains calculated from the HAC and FE/CM models. The strain is calculate in the middle between the two adjacent teeth on the sun gear. The strain during the entire rotating cycle is calculated. Good agreement is observed between the two solutions for all the three-, four- and five-planet systems, including the shape and amplitude of the strain curves. The results validate the capability of the HAC

method in predicting elastic deformations in the gear teeth.

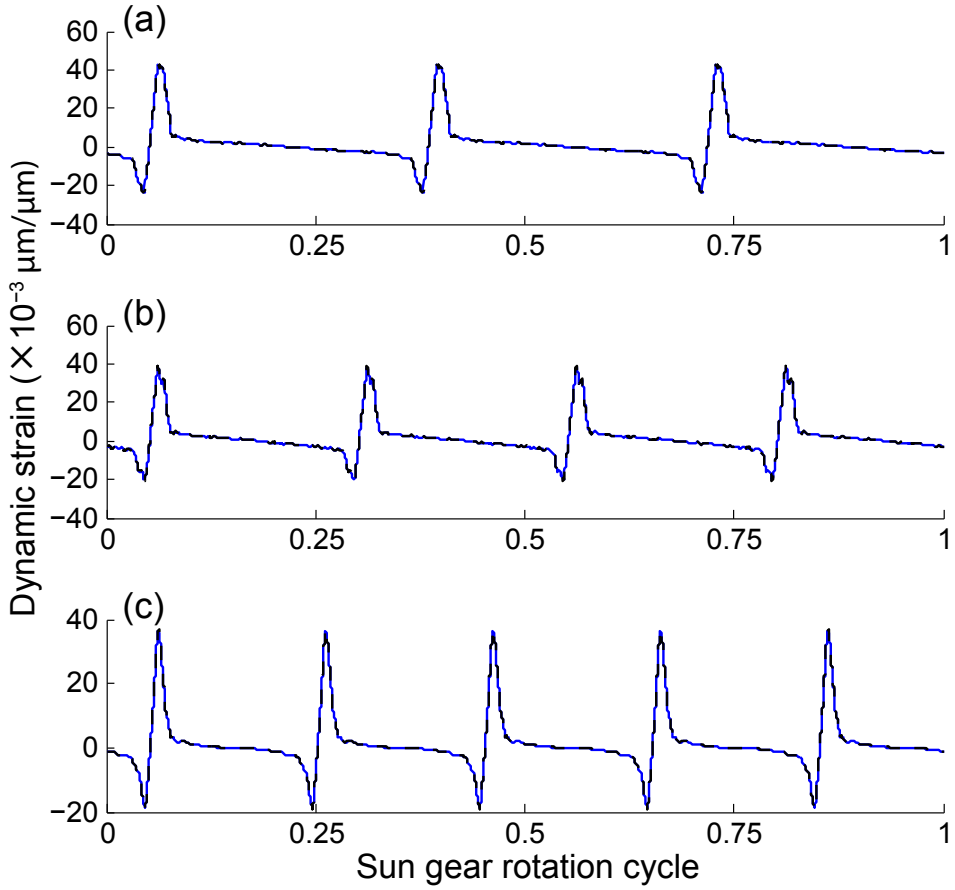

Figure 4.15: HAC calculation of dynamic tooth root strains for the (a) three planet, (b) four planet, and (c) five planet system at 1600 Hz mesh frequency compared with FE/CM results. The applied torque is 200 N-m on the sun gear. The strains are calculated in the middle between two adjacent teeth on the sun gear. The solid blue lines and dashed black lines denote HAC calculations and FE/CM calculations, respectively.

4.6 Conclusions

This work develops a hybrid analytical-computational method for nonlinear gear dynamics in multi-mesh systems. The high frequency vibrations in the gear bodies are neglected and the dynamic contact condition is approximated to the corresponding static condition at

the same mesh position with the same mesh deflection. The gear translational and rotational vibrations are calculated using a lumped-parameter model, and the dynamic mesh force for each tooth mesh is calculated from the corresponding force-deflection function. The force-deflection functions (FDFs) are generated statically using a finite element/contact mechanics model prior to the analytical dynamic analysis.

The HAC method is shown to accurately predict the dynamic response for multi-mesh systems, including near resonant gear speeds when high amplitude vibrations are excited and contact loss occurs. Drastically different dynamic responses are observed for the gears with and without tooth profile modifications, and they are all accurately predicted by the HAC method. The dynamic responses for the planetary gears with different number of planets and mesh phasing are accurately predicted.

The HAC method is computationally efficient. The method requires a series of static finite element simulations to generate the force-deflection functions prior to dynamic analysis. These static analyses need to be performed for only one time. The dynamic analysis is as fast as conventional lumped-parameter models. The elastic deformations in the gear body are calculated through post-processing.

The FDFs for idler gear systems can be generated statically from either a gear chain analysis, or several gear pair analyses for each tooth mesh. For planetary gear systems, the FDFs are generated by analyzing a sun-planet-ring gear chain system. The FDFs for the tooth meshes engaged by other planets are calculated by incorporating the mesh phasing to the first FDF.

The elastic gear tooth root strains for planetary gears are calculated using the strain-

deflection function (SDF) through post-processing. The total strain is calculated by combining the strains due to each tooth contact.

4.7 Appendix

4.7.1 System Matrices in Eq. 4.5

$$\mathbf{M} = \text{diag}(\mathbf{M}_c, \mathbf{M}_r, \mathbf{M}_s, \mathbf{M}_1, ..., \mathbf{M}_N)$$

$$\mathbf{M}_n = \text{diag}(m_n, m_n, I_n),\ n = c, r, s, 1, ...N$$

$$\mathbf{C} = \begin{bmatrix} \mathbf{C}_c + \sum \mathbf{C}_{cc}^i & \mathbf{0} & \mathbf{0} & \mathbf{C}_{cp}^1 & \mathbf{C}_{cp}^2 & \dots & \mathbf{C}_{cp}^N \\ & \mathbf{C}_r & \mathbf{0} & \mathbf{0} & \mathbf{0} & \dots & \mathbf{0} \\ & & \mathbf{C}_s & \mathbf{0} & \mathbf{0} & \dots & \mathbf{0} \\ & & & \mathbf{C}_{pp}^1 & \mathbf{0} & \dots & \mathbf{0} \\ & & & & \mathbf{C}_{pp}^2 & \dots & \mathbf{0} \\ & & & & & \ddots & \vdots \\ \text{symmetric} & & & & & & \mathbf{C}_{pp}^N \end{bmatrix}$$

$$\mathbf{C}_j = \text{diag}(c_j, c_j, c_{j\theta}),\ j = c, r, s$$

$$\mathbf{C}_{cc}^i = c_{pi} \begin{bmatrix} 1 & 0 & -r_c sin\psi_i \\ & 1 & r_c cos\psi_i \\ \text{symmetric} & & r_c^2 \end{bmatrix}$$

$$\mathbf{C}_{cp}^{i} = c_{pi} \begin{bmatrix} -cos\psi_i & sin\psi_i & 0 \\ -sin\psi_i & -cos\psi_i & 0 \\ 0 & -r_c & 0 \end{bmatrix}$$

$$\mathbf{C}_{pp}^{i} = \mathrm{diag}(c_i, c_i, c_{i\theta})$$

$$\mathbf{G} = \mathrm{diag}(\mathbf{G}_c, \mathbf{G}_r, \mathbf{G}_s, \mathbf{G}_1, ..., \mathbf{G}_N)$$

$$\mathbf{G}_n = \begin{bmatrix} 0 & -2m_n & 0 \\ 2m_n & 0 & 0 \\ 0 & 0 & 0 \end{bmatrix}$$

$$\mathbf{K}_b = \begin{bmatrix} \mathbf{K}_c + \sum \mathbf{K}_{cc}^{i} & \mathbf{0} & \mathbf{0} & \mathbf{K}_{cp}^{1} & \mathbf{K}_{cp}^{2} & \dots & \mathbf{K}_{cp}^{N} \\ & \mathbf{K}_r & \mathbf{0} & \mathbf{0} & \mathbf{0} & \dots & \mathbf{0} \\ & & \mathbf{K}_s & \mathbf{0} & \mathbf{0} & \dots & \mathbf{0} \\ & & & \mathbf{K}_{pp}^{1} & \mathbf{0} & \dots & \mathbf{0} \\ & & & & \mathbf{K}_{pp}^{2} & \dots & \mathbf{0} \\ & & & & & \ddots & \vdots \\ \text{symmetric} & & & & & & \mathbf{K}_{pp}^{N} \end{bmatrix}$$

$$\mathbf{K}_j = \mathrm{diag}(k_j, k_j, k_{j\theta}),\ j = c, r, s$$

$$\mathbf{K}_{cc}^{i} = k_{pi} \begin{bmatrix} 1 & 0 & -r_c sin\psi_i \\ & 1 & r_c cos\psi_i \\ \text{symmetric} & & r_c^2 \end{bmatrix}$$

$$\mathbf{K}_{cp}^{i} = k_{pi} \begin{bmatrix} -cos\psi_i & sin\psi_i & 0 \\ -sin\psi_i & -cos\psi_i & 0 \\ 0 & -r_c & 0 \end{bmatrix}$$

$$\mathbf{K}_{pp}^{i} = \text{diag}(k_i, k_i, k_{i\theta})$$

$$\mathbf{K}_{\Omega} = \text{diag}(\mathbf{K}_{\Omega}^{c}, \mathbf{K}_{\Omega}^{r}, \mathbf{M}_{\Omega}^{s}, \mathbf{M}_{\Omega}^{1}, ..., \mathbf{M}_{\Omega}^{N})$$

$$\mathbf{K}_{\Omega}^{n} = \text{diag}(m_n, m_n, 0)$$

4.7.2 Transformation matrix in Eq. 4.6

$$\mathbf{R} = \begin{bmatrix} \mathbf{0} & \mathbf{R}_{r1} & \mathbf{R}_{s1} & \mathbf{R}_p & \mathbf{0} & \dots & \mathbf{0} \\ \mathbf{0} & \mathbf{R}_{r2} & \mathbf{R}_{s2} & \mathbf{0} & \mathbf{R}_p & \dots & \mathbf{0} \\ \vdots & \vdots & \vdots & \vdots & \vdots & \ddots & \vdots \\ \mathbf{0} & \mathbf{R}_{rN} & \mathbf{R}_{sN} & \mathbf{0} & \mathbf{0} & \dots & \mathbf{R}_p \end{bmatrix}$$

$$\mathbf{R}_{ri} = \begin{bmatrix} 0 & 0 & 0 \\ -sin(\psi_{ri}) & cos(\psi_{ri}) & r_r \end{bmatrix}, i = 1, 2, ..., N$$

$$\mathbf{R}_{si} = \begin{bmatrix} -sin(\psi_{si}) & cos(\psi_{si}) & r_s \\ 0 & 0 & 0 \end{bmatrix}$$

$$\psi_{ri} = \psi_i - \alpha_r$$

$$\psi_{si} = \psi_i + \alpha_s$$

$$\mathbf{R}_p = \begin{bmatrix} -sin(\alpha_s) & -cos(\alpha_s) & r_{ps} \\ sin(\alpha_r) & -cos(\alpha_r) & -r_{pr} \end{bmatrix}$$

Chapter 5

Nonlinear Vibrations in Three-Dimensional Helical Gear Pairs

5.1 Motivation and Objectives

Helical gears are widely used in modern power transmission systems of many applications because of the advantages of helical gears. The translational and rotational vibrations in helical gears are transmitted to the main structure through shaft and bearing components, which causes system noise. The dynamic loads on the gears are directly relate to the durability and failure of the structure. These effect are especially significant near resonant gear speeds when high amplitude vibrations are excited and contact loss nonlinearities occur. We want a fast, accurate and reliable model to analyze the three-dimensional nonlinear vibrations in helical gears.

There are many models for gear dynamic analyses, among which the lumped-parameter models are the most commonly used. Lumped-parameter models assume the gears to have rigid bodies, and the elastic tooth contact is modeled as stiffness elements. The works for gear dynamic analyses using lumped parameter models can be found in Refs. [4, 5, 6].

In an early work, Gregory et al. [7] investigated the in-plane motions of spur gear pairs using a two-dimensional lumped-parameter model. Blankenship and Singh [8, 9] developed a linear mesh interface model for three-dimensional vibrations in helical gear pairs. Velex and Maatar [5] studied the dynamic response for gear pairs using a lumped-parameter model. Their model includes the effect of tooth profile and lead modifications. Eritenel and Parker [11, 12] investigated the tooth mesh nonlinearities and partial contact loss in helical gear pairs using a lumped-parameter model, in which the tooth contact surface is modeled as a discretized stiffness network. The works discussed above focus on gear translational and rotational vibrations, the gear tooth root strains are not directly calculated from the lumped-parameter models. In recent years, the spur gear pairs are modeled using lumped-parameter models, in which the gear dynamic mesh force is calculated using a force-deflection function [14, 3]. This model is shown to accurately predict the nonlinear dynamic response in spur gear pairs, including the elastic deformations and stresses in the tooth root and contact regions. Dai et al. [149] investigated the nonlinear in-plane dynamic response in multi-mesh gear chains and planetary gears using the same tooth contact formulation.

Conventional finite element models are usually not designed for gear dynamic analysis. When the gears are in contact, the elastic deformations in the tooth contact regions are usually orders of magnitude smaller than the gear teeth and body, a highly refined finite element mesh is required in the tooth contact region. When the gears are rotating kinematically, the contact locations moves along the tooth contact surface. Therefore, re-meshing is required for each time step or a highly refined finite element mesh is required for the entire tooth contact surface. Either method is computationally inefficient. Additionally, dynamic

analyses usually require a long time simulation to diminish the transient response. As a result, conventional finite element models are usually for static analyses and they do not have multi-body capabilities.

In recent years, a finite element/contact mechanics (FE/CM) formulation has been developed by Vijayakar and Co-workers [104, 105, 106] for contact problems in multi-body dynamics. This model combines a conventional finite element solution for the gear teeth and blank, and an analytical solution for the elastic tooth contact. Parker et al. [107] examined the dynamic response of a planetary gear system using the FE/CM model. Parker et al. [108] investigated the nonlinear dynamic response of a spur gear pair using the same FE/CM model. Classical softening type nonlinearities are accurately captured compared with experiments. Kahraman et al. [111] investigated the effect of flexibility of gears on the dynamic behavior of a planetary gear set. Tamminana et al. [118] studied the relationship between dynamic factors and dynamic transmission error using the FE/CM model. The dynamic factors defined in different parameters are compared. Ambarisha and Parker [51] investigated the nonlinear dynamics in planetary gears. Cooley et al. [109] developed a frequency domain method for fast and accurate dynamic analyses in gear pairs. Ericson and Parker [58] investigated the natural frequency and dynamic response of two planetary gear systems, and compared with experimental measurements. Dai et al. [135] studied the static and dynamic strain curves in spur gear pairs. The FE/CM results agree well with experiments. The FE/CM model is also used in studies for rolling element bearings. Guo and Parker [119] developed a method of obtaining accurate bearing stiffness for a wide range of bearing types and parameters.

In this work, we developed a hybrid analytical-computational (HAC) method that can accurately and efficiently predict the nonlinear dynamic response in helical gear pairs. The gears are analyzed using a lumped-parameter model, while the generalized dynamic mesh force at each time step is obtained from a generalized force-deflection function. The generalized force-deflection function is generated statically using the finite element/contact mechanics (FE/CM) model prior to the dynamic analyses. Alternatively, the FE/CM model can be replaced by other finite element or computational tools as long as they can give accurate static results. The micro geometries on the tooth contact surface due to tooth profile and lead modifications are precisely modeled in the FE/CM model, and incorporated in these static analyses; there is no additional procedures to include the effect from tooth modifications. In addition to the gear translational and rotational deflections, the HAC model can predict elastic deformations and stresses in the tooth root regions and contact zone. The HAC method is four orders of magnitude faster than the FE/CM model with almost no loss of accuracy.

5.2 Analytical Formulations

A non-unity ratio helical gear pair is studied in this work, as shown in Fig. 5.1. The input and output gears have 28 and 33 teeth, respectively. The gears have asymmetric teeth, and the transverse pressure angles are 20 ° and 25 °, respectively. Additionally, the gears have different facewidth and they have axially offset to represent the general situation. Both gears have tooth profile and lead modifications. Other gear parameters are shown in Tab. 5.1.

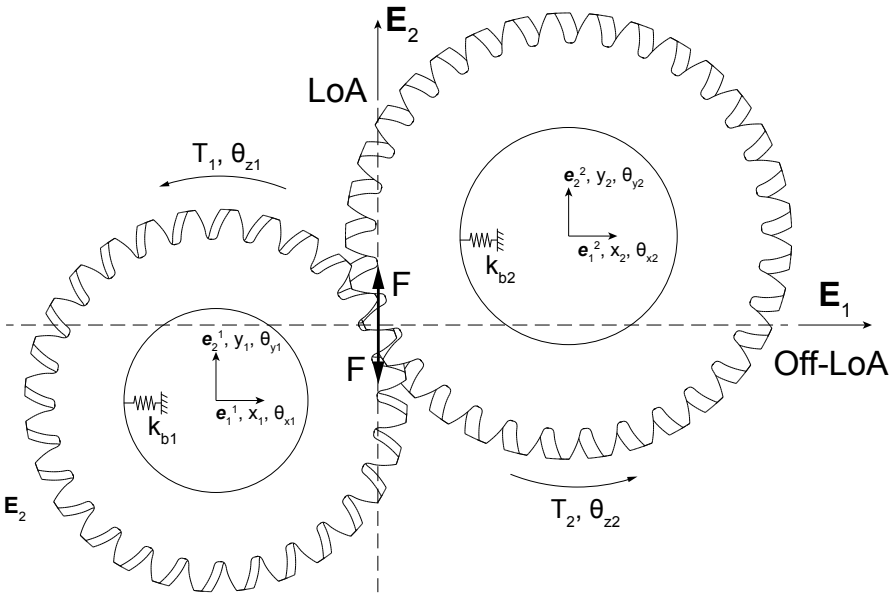

Figure 5.1: A Schematic of the non-unity ratio helical gear pair used in this study.

Table 5.1: Parameters for the non-unity-ratio helical gear pair system

Number of Teeth	28	33
Tip Diameter (mm)	149.925	174.925
Root Diameter (mm)	126.4	151.4
Face Width (mm)	10	16
Axial Position (mm)	1	-1
In-plane Center Distance (mm)	152.5	
Transverse Module (mm)	5	
Transverse Circular Tooth Thickness (mm)	7.6375	
Tooth Profile Modification	Quadratic	
Tip Relief (μm)	20	
Start Roll Angle (deg)	28.54	
Tip Relief (μm)	20	
Lead Crowning (μm)	5	
Density (kg/m^3)	7.85×10^3	
Young's Modulus (GPa)	201.5	
Translational Bearing Stiffness (N/m)	1e9	
Twisting and Tilting Bearing Stiffness (N·m/rad)	1e6	
Rotational Bearing Stiffness (N·m/rad)	5e4	

The system has 12 degrees of freedom: three translational and rotational degrees of freedom for each gear, as shown in Fig. 5.1. The input and output gears are formulated in fixed reference frames $\{\mathbf{e}_1^1, \mathbf{e}_2^1, \mathbf{e}_3^1\}$ and $\{\mathbf{e}_1^2, \mathbf{e}_2^2, \mathbf{e}_3^2\}$, respectively. The dynamic mesh force F

is within the $\mathbf{E}_2 - \mathbf{E}_3$ plane. The matrix equation of motion is

$$\mathbf{M}\ddot{\mathbf{q}} + \mathbf{C}\dot{\mathbf{q}} + \mathbf{K}\mathbf{q} + \mathbf{f}_{\mathrm{d}} = \mathbf{f}_{\mathrm{ext}}, \tag{5.1a}$$

$$\mathbf{q} = [x_1, y_1, z_1, \theta_{x1}, \theta_{y1}, \theta_{z1}, x_2, y_2, z_2, \theta_{x2}, \theta_{y2}, \theta_{z2}]^T. \tag{5.1b}$$

The mass matrix $\mathbf{M}$, damping matrix $\mathbf{C}$, and stiffness matrix $\mathbf{K}$ are

$$\mathbf{M} = \mathrm{diag}(m_1, m_1, m_1, I_{11}, I_{12}, I_{13}, m_2, m_2, m_2, I_{21}, I_{22}, I_{23}), \tag{5.2a}$$

$$\mathbf{C} = \mathrm{diag}(c_{x1}, c_{y1}, c_{y1}, c_{\theta_{x1}}, c_{\theta_{y1}}, c_{\theta_{z1}}, c_{x2}, c_{y2}, c_{y2}, c_{\theta_{x2}}, c_{\theta_{y2}}, c_{\theta_{z2}}), \tag{5.2b}$$

$$\mathbf{K} = \mathrm{diag}(k_{x1}, k_{y1}, k_{y1}, k_{\theta_{x1}}, k_{\theta_{y1}}, k_{\theta_{z1}}, k_{x2}, k_{y2}, k_{y2}, k_{\theta_{x2}}, k_{\theta_{y2}}, k_{\theta_{z2}}), \tag{5.2c}$$

where m_i $(i = 1, 2)$ and $I_{i,j}$ $(j = 1, 2, 3)$ are the masses and moment of inertia of the gears, respectively. c_{ui} and k_{ui} $(u = x, y, z, \theta_x, \theta_y, \theta_z)$ are the damping and stiffness in the bearing elements, respectively. The vector $\mathbf{f}_{\mathrm{d}}$ contains the generalized force due to contact. For three-dimensional helical gear systems, these forces and torques are determined by dynamic contact conditions and dynamic contact pressure distributions on the tooth contact surface. The vector $\mathbf{f}_{\mathrm{ext}}$ represents forcing due to the applied forces and torques. The gear mesh deflection and mesh twisting are given by

$$x = \mathbf{r}_{mesh}^T \mathbf{q}, \tag{5.3a}$$

$$\gamma = \mathbf{r}_{twist}^T \mathbf{q}, \tag{5.3b}$$

where the transformation vectors $\mathbf{r}_{mesh}$ and $\mathbf{r}_{twist}$ are given by

$$\mathbf{r}_{mesh} = \frac{1}{\sqrt{1 - sin^2\alpha sin^2\beta}}[\mathbf{r}_{t1}^T, \mathbf{r}_{r1}^T, \mathbf{r}_{t2}^T, \mathbf{r}_{r2}^T]^T, \tag{5.4a}$$

$$\mathbf{r}_{t1} = [0, cos\beta, cos\alpha sin\beta]^T, \tag{5.4b}$$

$$\mathbf{r}_{r1} = [r_1 sin\alpha sin\beta + \frac{z_0}{2}cos\beta, -r_1 cos\alpha sin\beta, r_1 cos\beta]^T, \tag{5.4c}$$

$$\mathbf{r}_{t2} = [0, -cos\beta, -cos\alpha sin\beta]^T, \tag{5.4d}$$

$$\mathbf{r}_{r2} = [r_2 sin\alpha sin\beta + \frac{z_0}{2}cos\beta, -r_2 cos\alpha sin\beta, r_2 cos\beta]^T, \tag{5.4e}$$

$$\mathbf{r}_{twist} = [0, 0, 0, 1, 0, 0, 0, 0, 0, -1, 0, 0]^T. \tag{5.4f}$$

When the gears are rotating kinematically, the dynamic contact condition changes periodically. As a result, the dynamic mesh force oscillates periodically. The generalized dynamic force $\mathbf{f}_{\mathrm{d}}$ due to contact in Eq. 5.1 is the key quantity that drives the system vibration. The accuracy of the model depends on the accuracy in predicting the generalized force. This force, however, is difficult to calculate because it is affected by tooth modifications, applied torque, and contact loss nonlinearities. For helical gears, the contact pressure distribution is highly affected by the gear twisting, thus changing the generalized force. The dynamic mesh force for spur gears are calculated using a force-deflection function in Refs. [14, 3, 149]. In this work, we calculate the generalized dynamic force using a generalized force-deflection function.

5.3 Finite Element Calculations of Force-Deflection Function

5.3.1 Assumption

The gear vibrations are classified into two types: the translational and rotational rigid body deflections associated with **q** in Eq. 5.1, and the elastic deformations in the gear teeth and blank, as shown in Fig. 5.2. The rigid body deflections vibrates at the mesh frequency and its first harmonics. These vibrations have higher amplitude near the natural frequencies of the system. The elastic deformations in the gear teeth and blank, for example, the in-plane and out-of-plane tooth bending and tooth twisting shown in Fig. 5.2, usually vibrate at frequencies that are much higher than the rigid body vibrations associated with **q** and the system natural frequencies. Additionally, these elastic deformation vibrations have small amplitudes. As a results, the vibrations in the elastic gear teeth and blank vanishes rapidly. In other words, the system reaches to its steady state rapidly compared with the gear rigid body motions. There is no other assumptions about the tooth contact.

Based on the situation above, we make the assumption that the elastic deformations in the gear teeth and blank are negligible. Under this assumption, the dynamic contact condition is approximated to the instantaneous equilibrium position, which is the static contact configuration at the same nominal gear mesh position with the same mesh deflection and mesh twisting. Thus, the generalized dynamic force is the same as those static values calculated in advance at the same contact configuration. Additionally, the dynamic tooth

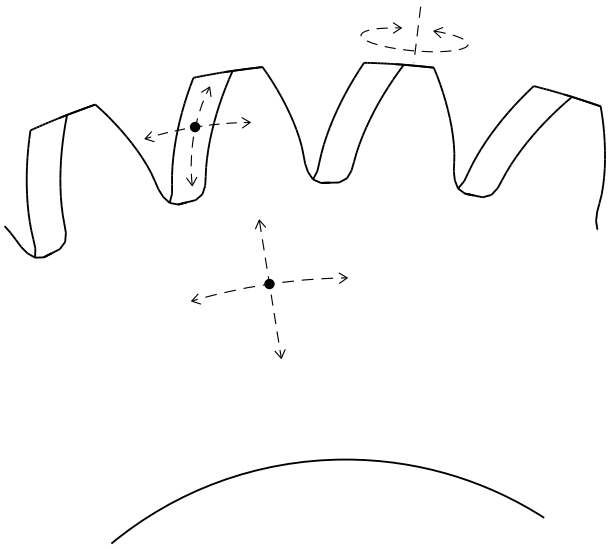

Figure 5.2: Schematic of the elastic deformations in the gear teeth and blank. The black circles represent arbitrary material points on the elastic gear body.

contact pressures, tooth root strains, and any other quantities of interest is also uniquely determined from the corresponding static configurations, as shown subsequently.

5.3.2 Generalized Force-Deflection Function

For in-plane motions in spur gears, like those studied in Refs. [14, 3, 149], the mesh force is determined by nominal gear mesh position (gear kinematics) and mesh deflection. For helical gears, however, the contact condition is highly affected by gear mesh twisting. Figure 5.3 compares the static contact pressure distribution on the 28-teeth gear at 200 N-m applied torque that calculated under the same condition except for the mesh twisting angle γ. The contact pressure distribution is highly sensitive to the mesh twisting angle, as shown in Fig. 5.3. Additionally, the generalized force $\mathbf{f}_{\mathrm{d}}$ due to contact is directly related to these contact pressure distributions. As a result, the generalized force is also affected by the mesh twisting angle γ.

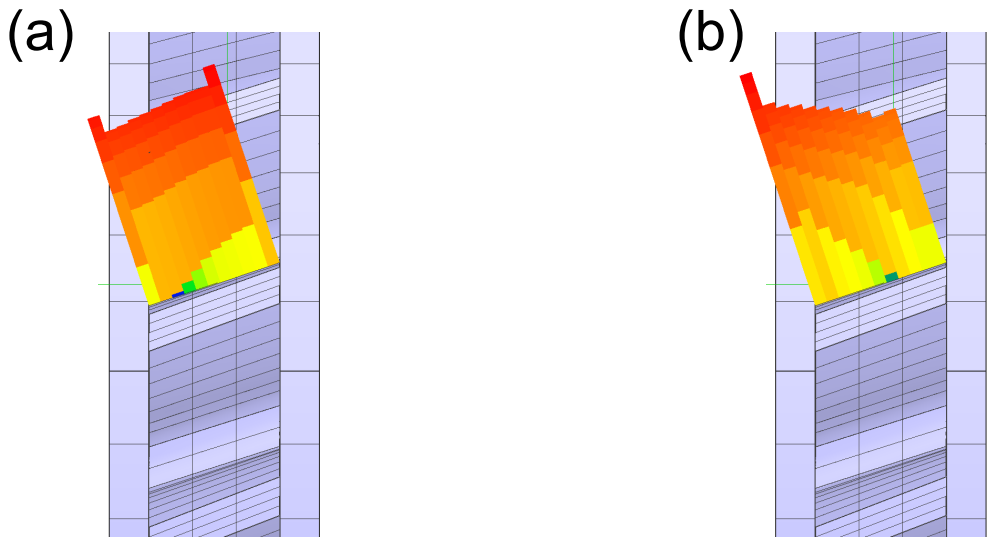

Figure 5.3: Contact pressure distribution on the 28-teeth gear with 200 N-m applied torque. The mesh twisting angle γ is (a) 0.002° and (b) -0.002°, respectively.

Figure 5.4 shows the finite element calculation of generalized force-deflection function (GFDF) for the 28-33 teeth helical gear pair. The GFDF is generated by combining a series of static finite element results. At each mesh twisting angle, the gear static mesh deflection is calculated, for many applied torques across the range of interest, throughout a mesh cycle. The effect of tooth profile and lead modifications are included in these static finite element analyses; there is no additional procedure to incorporate tooth modifications. The GFDF is then used to calculate the generalized dynamic force $\mathbf{f}_{\mathrm{d}}(x, \gamma, t)$ in Eq. 5.1 based on the instantaneous mesh deflection, mesh twisting angle, and gear mesh position, which is uniquely determined by kinematics. There are two mesh cycles in Fig. 5.4 for better graphic presentation; there is only one mesh cycle that calculated through the static analyses.

The accuracy of the HAC method relies on the accuracy in predicting the dynamic forces, which is further determined by the underlying tool to generate those GFDF through static analyses. In this work, we use a Finite Element/Contact Mechanics (FE/CM) model

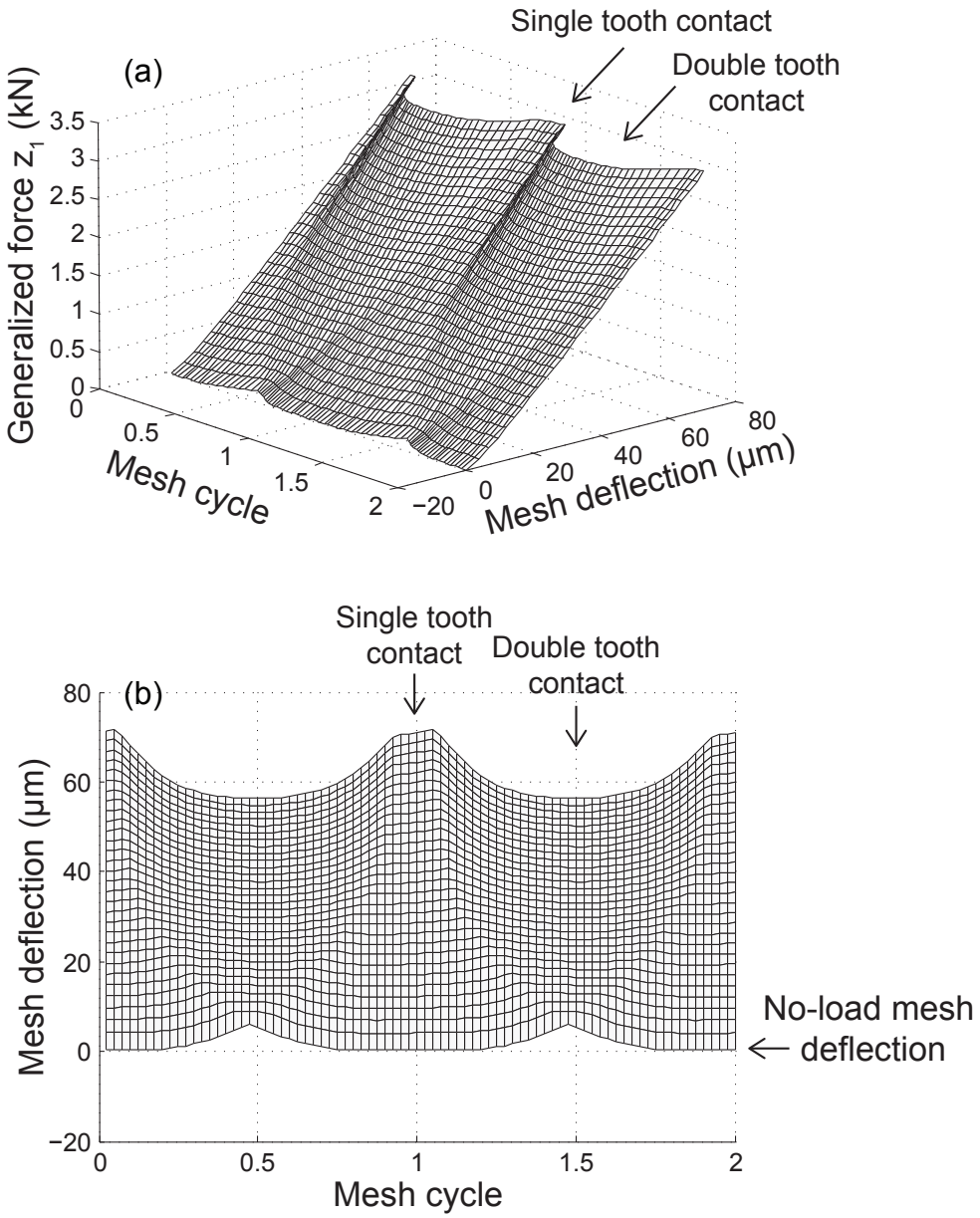

Figure 5.4: Finite element calculation of the generalized force-deflection function for the 28-33 tooth helical gear pair. The force is measured for the 28-teeth gear along $\mathbf{e}_3^1$ direction. The mesh twisting angle γ is 0°.

for the static calculations. Alternatively, the FE/CM model can be replaced by any other finite element softwares or even analytical models as long as they can give accurate static results.

The FE/CM model is developed by Vijayakar and co-workers [], and is designed for contact problems in multi-body dynamics. We brief introduce the model. The gears are divided into two-parts: a far-field for the gear teeth and blank, and a near-field on the gear tooth contact surface. In the far-field, conventional finite element method is used for the deformations in the gear teeth and blank. A special Hermite-polynomial shape function is used for the gear teeth to precisely model the micro-geometries on the tooth contact surface due to tooth profile and lead modifications. In the near-field, an analytical solution for a point force on a half-space is used to compute the contact force distribution. These two solutions are matched on a sub-surface that chosen carefully so that the two solutions remain valid. Using this method, only a relatively coarse finite element mesh is required for the FE/CM model. Additionally, when the gears are rotating kinematically, the same finite element mesh can be used; there is no need to re-mesh the gears for each time step. As a result, the FE/CM model is computationally efficiency and dynamic analyses are feasible. The FE/CM model is shown to accurately predict the gear translational and rotational vibrations [108, 109, 58] and tooth root stresses and strains [135] compared with experiments. More details about the FE/CM model can be found in the literature.

The GFDF in Fig. 5.4 only shows the generalized force on the 28-teeth gear along $\mathbf{e}_3^1$ direction. There is essentially 12 generalized force-deflection functions for the system: 6 for each gear. For each GFDF, there are multiple sub-force-deflection functions, one for each

mesh twisting angle. Only the sub-function at $\gamma = 0°$ is shown in Fig. 5.4. The sub-functions at other mesh twisting angles deviates from that at $\gamma = 0°$ due to the change of contact pressure distribution. The GFDF is very sensitive to the tooth profile and lead modifications on the tooth contact surface. The gear tooth modifications are precisely modeled using the FE/CM model, and the effect of contact pressure distribution from tooth modifications are accurately captured from the static analyses. There is no additional procedures to incorporate the tooth modifications. The non-zero mesh deflections at zero force in Fig. 5.4, defined as the no load mesh deflection(NLMD), are due to tooth modifications. The gears are engaged when the mesh deflection is greater than the corresponding NLMD at the same mesh cycle position. When the mesh deflection is smaller than the NLMD, the gear teeth separate. The resolution of the static analyses should be high enough so that the features of the FDF surface is accurately captured. Distinct boundaries are obtained for single- and double- tooth contact regions, as shown in Fig. 5.4. The double tooth contact region is wider with increasing mesh deflection, as expected. This is due to more tooth bending at high load region, causing more teeth to be engaged.

A highlight of this method is that theses static analyses need to be done for only once to generate the GFDF. Once the static analyses are finished, all the results of interest, including the gear translational and rotational deflections, mesh force, contact pressure, tooth root stresses and strains, etc., are saved for post processing. When generating the GFDF from the static analyses, the input quantities are the applied torque, mesh position, and twisting angle. When calculating the generalized force using the GFDF, however, the input quantities are mesh position, mesh deflection, and mesh twisting angle (determined by

q from Eqs. 5.3).

5.4 Calculation of Dynamic Response

The numerical procedures are similar to that used in Ref. [3] for single-mesh spur gear pairs, and in Ref. [149] for multi-mesh gear chains and planetary gears with spur gears. We brief summarize the process. More details about the dynamic response calculations can be found in the references.

5.4.1 Gear Translational and Rotational Vibrations

The gear translational and rotational vibrations are calculated by integrating Eq. 5.1 using Runge-Kutta methods. At each time step, the generalized dynamic force due to contact is calculated using the generalized force-deflection function, as discussed in Sec. 5.3. The gear mesh position is uniquely determined by kinematics because the gear vibrations are at a much smaller scale compared with gear kinematics. The gear mesh deflection and twisting angle are calculated based on the gear instantaneous translational and rotational deflections **q** using Eqs. 5.3. Using linear interpolation, the generalized dynamic force is calculated using the GFDF. Numerical integration is performed at a single time step. This procedure repeats until transient response diminishes and the system reaches steady state.

5.4.2 Elastic Stresses and Strains in the Gear Teeth

The dynamic response of other quantities, including the gear tooth contact pressure, root stresses and strains, are calculated through post-processing. In this work, we calculate the dynamic tooth root strains as an example. The strains at multiple locations in the tooth root region are calculated, as shown the red circles in Fig. 5.5. For each location, the strain-deflection function (SDF) is generated by calculating the static strains at each mesh position, mesh deflection, and mesh twisting angle from the same static results that used in Sec. 5.3.2. We emphasize that no additional numerical simulation is required; the strain-deflection function is entirely generated from post-processing using previous static results. Figure 5.6 shows the strain-deflection function calculated at location 3 of Fig. 5.5. Unlike the GFDF, which is unique for each gear pair, there are many SDFs for a system; one for a given position on the gear teeth and a specific direction. As discussed in Sec. 5.3, the SDF represents the relationship between strains and mesh deflection at giving mesh deflection, mesh twisting angle, and mesh position, and this relationship remains to be valid under dynamic conditions. The dynamic tooth root strains are calculated using the SDf and the instantaneous dynamic deflections computed from Sec. 5.4.1. Other dynamic quantities, tooth root strains at other locations or tooth contact pressure, for example, can be calculated similarly using the corresponding functions.

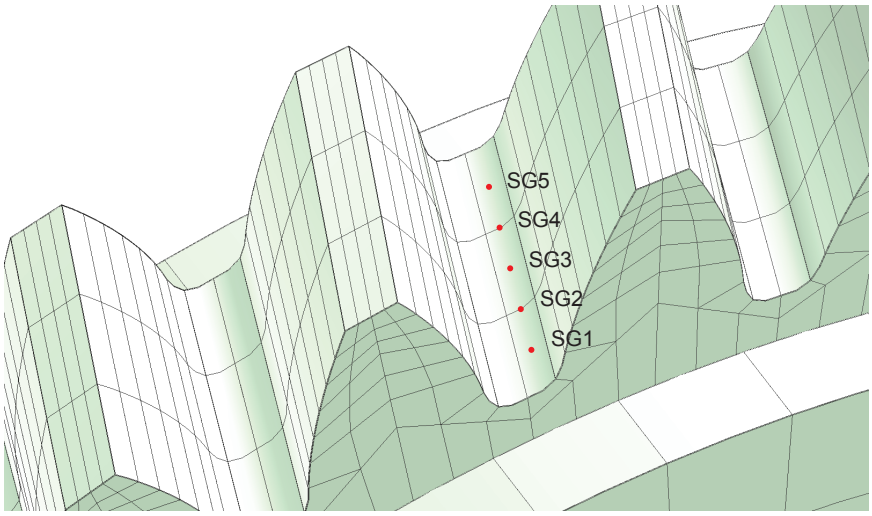

Figure 5.5: Strain gage locations on the 33-teeth gear. The strains are calculated on the drive side at 75.70 mm away from the gear center. The axial positions are 16.67%, 33.33%, 50%, 66.67%, and 83.33% of the facewidth, respectively.

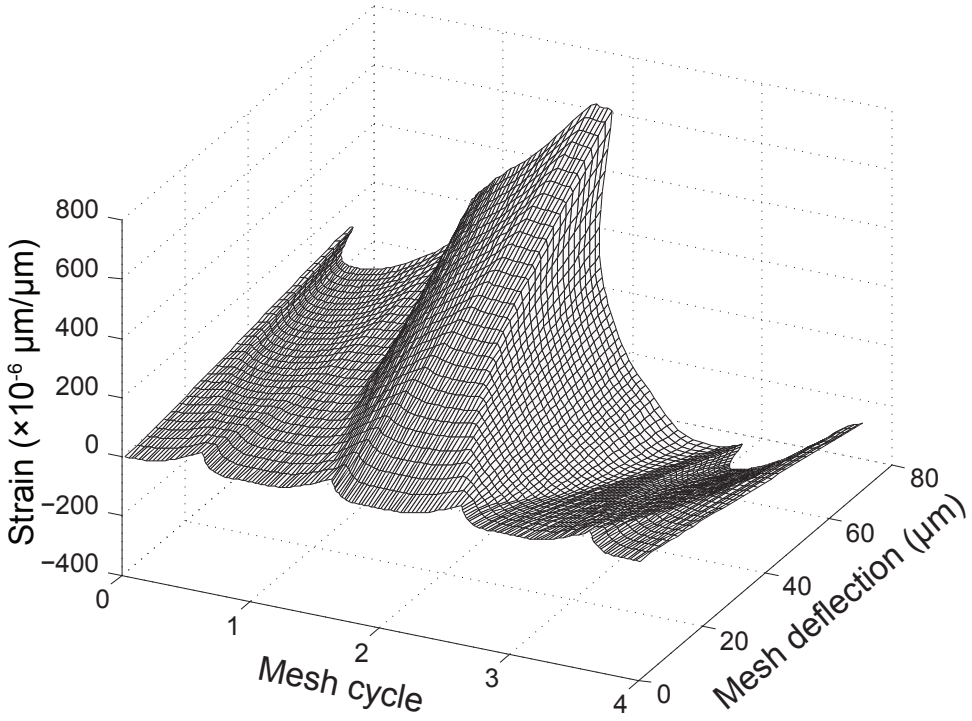

Figure 5.6: Finite element calculation of the strain-deflection function calculated for the 28-33 tooth helical gear pair. The strains are calculated at location SG3 on Fig. 5.5.

5.4.3 Computational Efficiency

The HAC method is computationally efficient. There are three steps: static analyses, dynamic numerical integration, and post-processing. The simulation time for the static analyses depends on the underlying tool. These static analyses at each torque is usually faster than dynamic analyses. At each torque, the gears are analyzed for only one mesh cycle; we do not require the long time analyses to diminish the transient response. These static analyses are performed for only one time, and they can be preformed in parallel. Once the static analyses are finished, all the necessary information of the system, including the gear translational and rotational deformations, stresses and strains at each node, and any other quantities of interest, are saved for post-processing.

The dynamic analytical calculations are as fast as conventional lumped-parameter models. For the current helical gear pair, it takes about 0.01 seconds on a conventional laptop for each mesh cycle using the HAC method, which is four orders of magnitude faster than the dynamic analysis with the FE/CM model. The speed increment is meaningful for nonlinear analyses, for which the gears are usually analyzed at multiple speeds sequentially.

5.5 Numerical Results

The proceeding section compares the HAC predictions of gear dynamic response for helical gear pairs with the FE/CM results for validation. The benchmark for the HAC model is the dynamic FE/CM model. Because the HAC predictions requires the GFDF from the static FE/CM model, it can not be more accurate. The proceeding comparisons

illustrate how good or how much or how little accuracy is lost with the HAC method.

The gears are analyzed over a wide range of speed and torque combinations. At each speed, the gears are analyzed over a long range so that the transient response diminishes and the steady state response is recorded. Figure 5.7 shows the HAC calculation of the root mean square (RMS) of the oscillating component of dynamic mesh deflections of the helical gear pair compared with FE/CM results. The applied torque is 200 N-m. The resonance locations are accurately predicted by the HAC model compared with the FE/CM results. There are multiple resonances occur within the speed range. This is because all the translational and rotational degrees of freedom of the gears are released, and the natural frequencies of the system associated with different mode shapes are widely distributed in the speed range. Some of the resonances are super harmonic resonances due to the nonlinearity of the system. Near these resonances, the higher (2nd, 3rd, etc.) harmonics of the mesh frequency is close to the natural frequency, thus causing resonances. The vibration amplitude predicted by the HAC model agree well with FE/CM calculations, including in- and off- resonant gear speeds. Unlike the spur gear pairs, the contact loss nonlinearity is much weaker in helical gears. The classical softening type nonlinearities and jump phenomena is not obtained for both the HAC and FE/CM results for these helical gear pairs. This result agrees with those from other works on helical gear pairs [109]. Although there is no complete contact loss, the system is still nonlinear. The nonlinearity comes from partial contact loss (for which portions of the gear teeth contact line losing contact [12](eritenelmmt2012)) and incomplete tooth contact (one of the adjacent tooth pairs normally in contact losing contact [135]).

Figure 5.8 compares the HAC and FE/CM calculations of translational and rotational

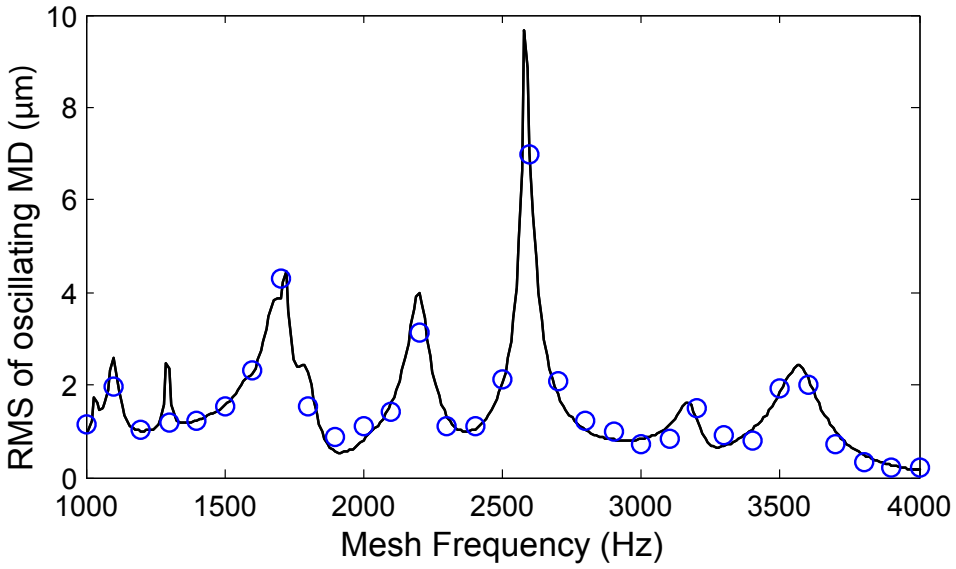

Figure 5.7: Oscillating (RMS) components of the dynamic mesh deflection for the helical gear system at 200 N-m applied torque on the 28-teeth gear. The black lines and blue circles denote the HAC calculations and FE/CM calculations, respectively.

vibrations for the 28-teeth gear. The gears are at 200 N-m applied torque and 1200 Hz mesh frequency. Good agreement is seen between the two solutions, including the shape and amplitude of the deflection curves. The shape and amplitude of the deflection curves for each direction varies, and they have different frequency content, as shown in Fig. 5.8. This is because the natural frequency for the vibration modes dominated by each direction differs, and the excitation from the generalized force-deflection function has different frequency content along each direction.

Figure 5.9 compares the HAC and FE/CM calculations of mesh deflection and mesh twisting angle for the helical gear pair. The applied torque and mesh frequency are the same as those in Fig. 5.8. Good agreement continues, as shown the shape and amplitude of the deflection curves in Fig. 5.9. Drastic difference of frequency content is seen between the mesh deflection (Fig. 5.9(a)) and mesh twisting angle (Fig. 5.9(b)), and they are all accurately

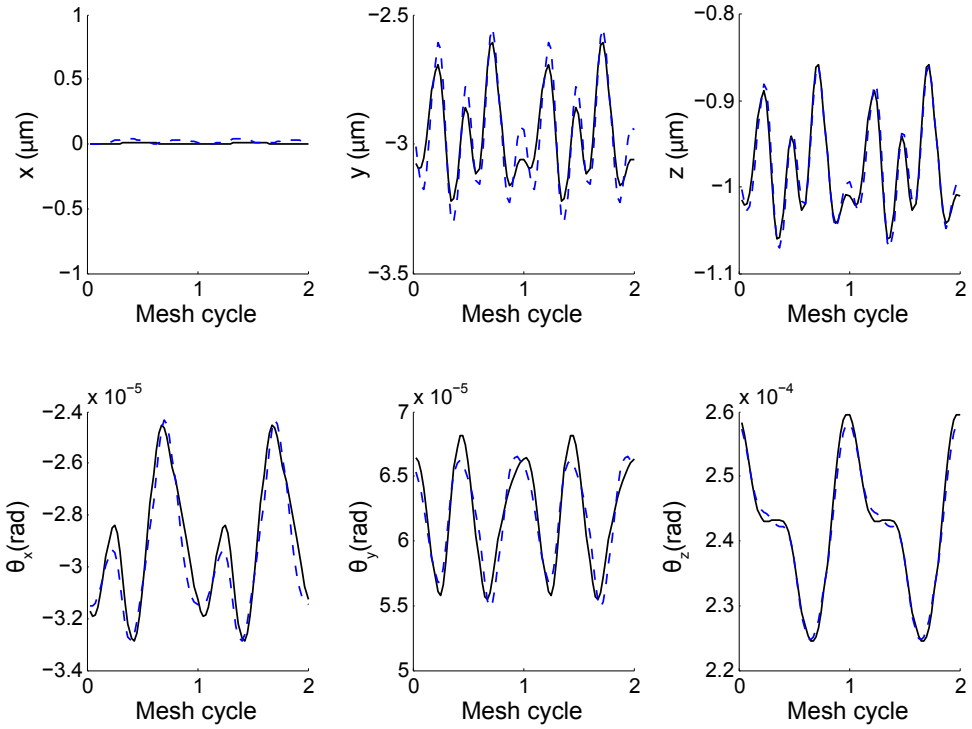

Figure 5.8: HAC calculation of translational and rotational deflections compared with FE/CM results for the 28-teeth gear. The gears are at 200 N-m applied torque and 1200 Hz mesh frequency. The solid black lines and dashed blue lines denote the HAC calculations and FE/CM calculations, respectively.

predicted by the HAC model compared with the FE/CM results. The good agreement in Fig. 5.9 is due to the good agreement in gear translational and rotational vibrations (as shown in Fig. 5.8). The gear mesh deflection and mesh twisting angle are directly calculated from those quantities using Eq. 5.3. As discussed in Sec. 5.3.2, the generalized dynamic mesh force is calculated using the dynamic quantities shown in Fig. 5.9. The accurate prediction of gear dynamic mesh deflection and mesh twisting angle guarantees the accuracy in predicting the generalized dynamic mesh force.

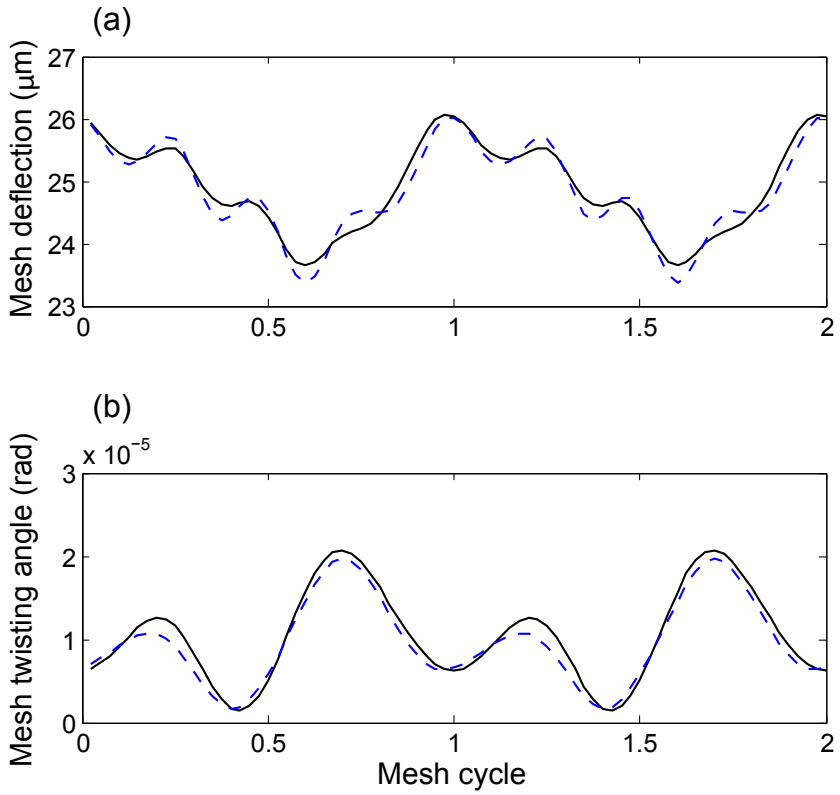

Figure 5.9: HAC calculation of (a) mesh deflection and (b) mesh twisting angle compared with FE/CM results for the 28-teeth gear. The gears are at 200 N-m applied torque and 1200 Hz mesh frequency. The solid black lines and dashed blue lines denote the HAC calculations and FE/CM calculations, respectively.

Figure 5.10 compares the gear translational and rotational vibrations from the HAC and FE/CM calculations. The applied torque is 200 N-m on the 28-teeth gear. The gears

are at 2600 Hz mesh frequency near resonant gear speeds, as shown in Fig. 5.7. High amplitude vibrations are observed near this resonance by comparing the dynamic amplitudes in Fig. 5.10 and 5.8 away from resonance. A meaningfully large difference is observed between the HAC and FE/CM results for the translational deflections along the off line-of-action, as shown in Fig. 5.10. This difference is mainly because the gears are near resonant speeds where the dynamic response is sensitive to the non-dimensional mesh frequency (mesh frequency divided by the natural frequency). For the HAC and FE/CM calculations, there is an error in natural frequency, thus the non-dimensional mesh frequencies are not the same, causing the difference shown in Fig. 5.10. Additionally, the effect of the gear translational deflections on the generalized mesh force is not included in the HAC model, which also cause some error. Good agreement between the HAC and FE/CM results is observed for the other 2 translational deflections and all the rotational deflections.

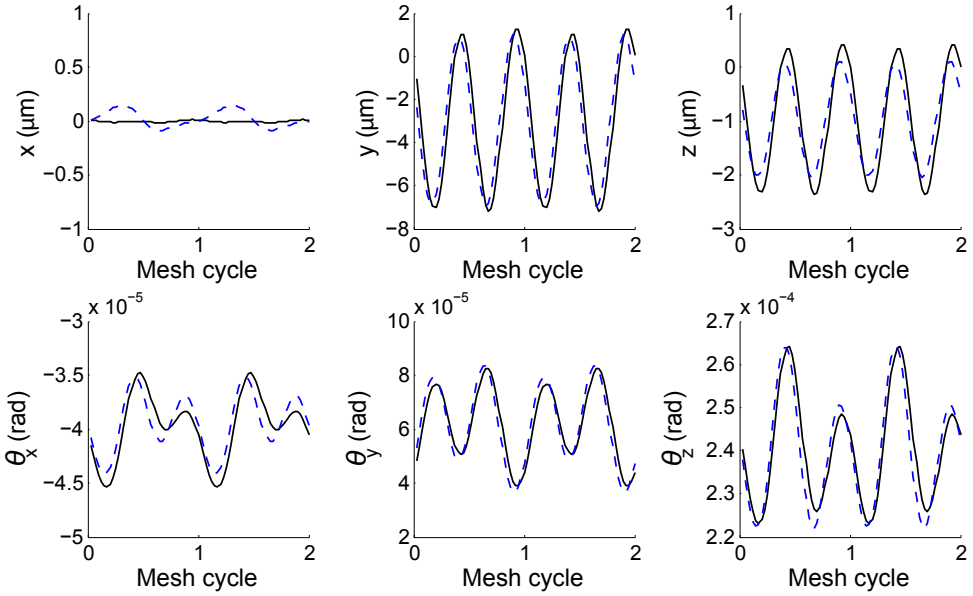

Figure 5.10: HAC calculation of translational and rotational deflections compared with FE/CM results for the 28-teeth gear. The gears are at 200 N-m applied torque and 2600 Hz mesh frequency. The solid black lines and dashed blue lines denote the HAC calculations and FE/CM calculations, respectively.

Figure 5.11 compares the HAC and FE/CM calculation of dynamic mesh deflection and mesh twisting angle for the helical gear system. The gears are at the same torque and speed combination shown in Fig. 5.10 near resonant gear speeds. High amplitude vibration is observed near resonant gear speeds, as shown in Fig. 5.11(a). The frequency content is different than that at off-resonant gear speeds (shown in Fig. 5.9(a)), and good agreement is observed between the HAC and FE/CM solutions. The dynamic mesh twisting angle is also accurately predicted by the HAC model compared with FE/CM calculations, as shown in Fig. 5.11(b). The accurate prediction of gear dynamic mesh deflections and mesh twisting angles guarantees the accuracy in predicting the generalized dynamic mesh force, which is directly related to the gear dynamic response predictions.

Figure 5.12 compares the HAC and FE/CM calculation of dynamic tooth root strains for the helical gear pair. The gears are at 200 N-m applied torque and 1200 Hz mesh frequency. The strains are calculated on the 33-teeth gear, as shown the strain gage locations in Fig. 5.5. Drastic difference is observed for the strains calculated at different locations, as shown in Fig. 5.12, and they are all accurately predicted by the HAC model compared with FE/CM results. Positive strains are observed before the tooth engagement, and negative strains are observed after the tooth engagement. These strains are due to the gear blank deformations while the adjacent teeth is taking load, and these features are all accurately predicted by the HAC model. More details about the features of the dynamic strain curves can be found in Ref. [135].

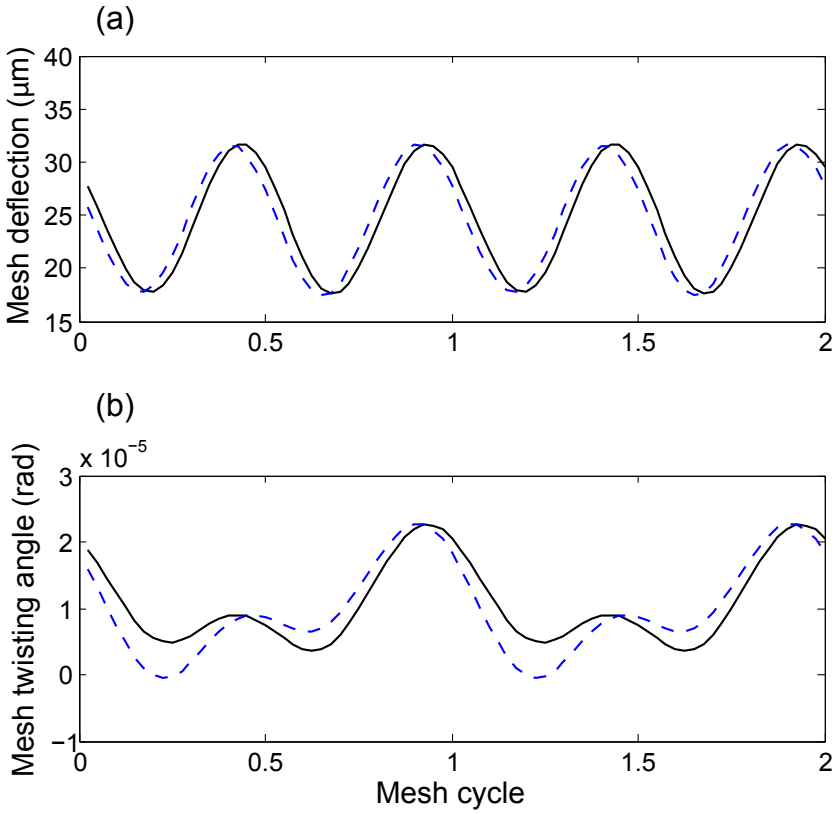

Figure 5.11: HAC calculation of (a) mesh deflection and (b) mesh twisting angle compared with FE/CM results for the 28-teeth gear. The gears are at 200 N-m applied torque and 2600 Hz mesh frequency. The solid black lines and dashed blue lines denote the HAC calculations and FE/CM calculations, respectively.

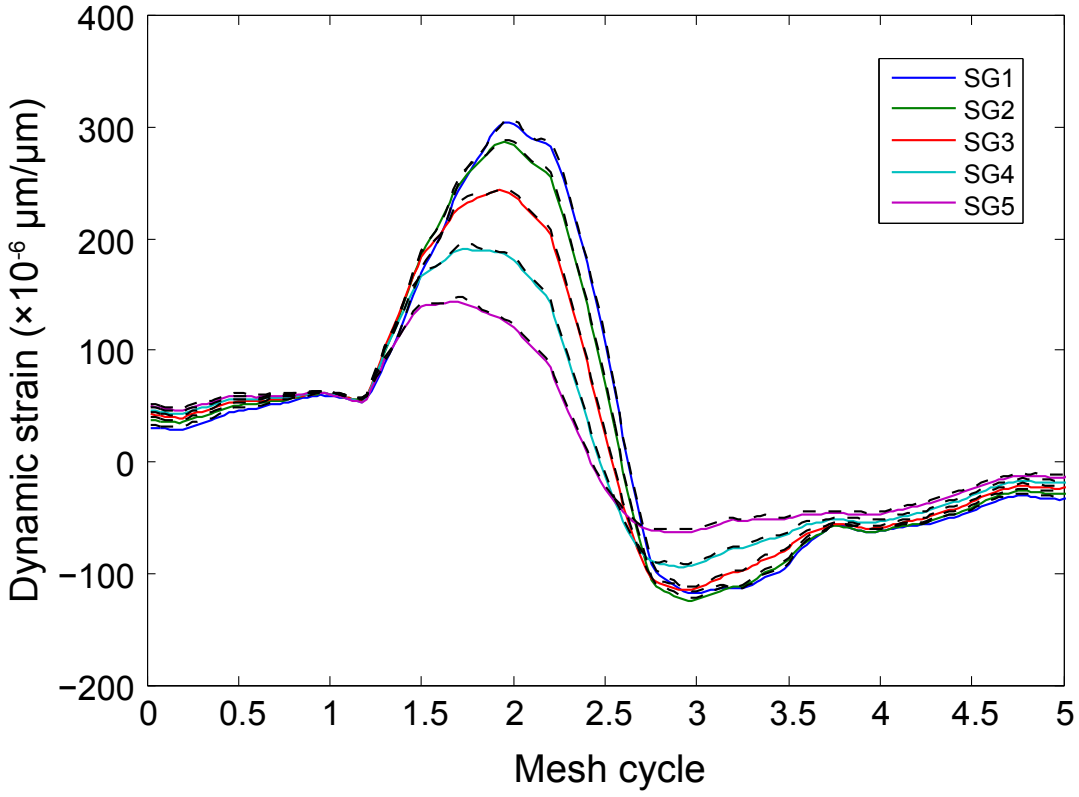

Figure 5.12: HAC calculation of dynamic tooth root strains compared with FE/CM results for the helical gear pair. The gears are at 200 N-m applied torque and 1200 Hz mesh frequency. The strains are calculated on the 33-teeth gear, and the strain gage locations are shown in Fig. 5.5. The solid colored lines and dashed black lines denote the HAC calculations and FE/CM calculations, respectively.

5.6 Conclusions

A hybrid analytical-computational (HAC) is developed for nonlinear dynamics in three-dimensional helical gear pairs. Neglecting the high frequency vibrations in the elastic gear teeth and blank, the instantaneous dynamic contact condition is approximated to the corresponding static conditions at the same nominal gear mesh position, mesh deflection, and mesh twisting angle. The gear translational and rotational vibrations are calculated using lumped-parameter models, while the generalized dynamic mesh force is calculated using a generalized force-deflection function that generated through a series of static finite element analyses using computational models. The dynamic tooth root strains are calculated through post-processing.

The HAC method accurately predicts the nonlinear dynamic responses in helical gears, including the translational and rotational vibrations near resonant gear speeds when high amplitude vibrations are excited. Different dynamic tooth root strains are obtained at different locations in the gear tooth root region, and they are all accurately predicted by the HAC model.

The HAC method is computationally efficient. It requires a one-time static analyses using the underlying finite element model to generate the generalized force-deflection function and any other quantity of interest. The analytical dynamic analysis is almost as fast as conventional lumped-parameter models. The simulation time for post-processing is negligible.

Bibliography

[1] Hotait, M. and Kahraman, A., 2013, "Experiments on the relationship between the dynamic transmission error and the dynamic stress factor of spur gear pairs," Mechanism and Machine Theory, **70**, pp. 116–128.

[2] Kahraman, A. and Blankenship, G. W., 1999, "Effect of involute contact ratio on spur gear dynamics," ASME Journal of Mechanical Design, **121**(1), pp. 112–118.

[3] Dai, X., Cooley, C. G., and Parker, R. G., 2017, "An efficient hybrid analytical-computational method for nonlinear spur gear dynamics," Submitted to ASME Journal of Vibration and Acoustics.

[4] Özgüven, H. N. and Houser, D. R., 1988, "Mathematical models used in gear dynamics - a review," Journal of Sound and Vibration, **121**(3), pp. 383–411.

[5] Velex, P. and Maatar, M., 1996, "A mathematical model for analyzing the influence of shape deviations and mounting errors on gear dynamic behaviour," Journal of Sound and Vibration, **191**(5), pp. 629–660.

[6] Wang, J., Li, R., and Peng, X., 2003, "Survey of nonlinear vibration of gear transmission systems," Applied Mechanics Reviews, **56**(3), pp. 309–329.

[7] Gregory, R. W., Harris, S. L., and Munro, R. G., 1963, "Dynamic behaviour of spur gears," Proceedings of the Institution of Mechanical Engineers, **178**(1), pp. 207–226.

[8] Blankenship, G. W. and Singh, R., 1995, "A new gear mesh interface dynamic model to predict multi-dimensional force coupling and excitation," Mechanism and Machine Theory, **30**(1), pp. 43–57.

[9] Blankenship, G. W. and Singh, R., 1995, "Dynamic force transmissibility in helical gear pairs," Mechanism and Machine Theory, **30**(3), pp. 323–339.

[10] Velex, P. and Ajmi, M., 2006, "On the modelling of excitations in geared systems by transmission errors," Journal of Sound and Vibration, **290**(3-5), pp. 882–909.

[11] Eritenel, T. and Parker, R. G., 2012, "Three-dimensional nonlinear vibration of gear pairs," Journal of Sound and Vibration, **331**(15), pp. 3628–3648.

[12] Eritenel, T. and Parker, R. G., 2012, "An investigation of tooth mesh nonlinearity and partial contact loss in gear pairs using a lumped-parameter model," Mechanism and Machine Theory, **56**(1), pp. 28–51.

[13] Palermo, A., Mundo, D., Hadjit, R., and Desmet, W., 2013, "Multibody element for spur and helical gear meshing based on detailed three-dimensional contact calculations," Mechanism and Machine Theory, **62**, pp. 13–30.

[14] Eritenel, T. and Parker, R. G., 2013, "Nonlinear vibration of gears with tooth surface modifications," Journal of Vibration and Acoustics, **135**(5), p. 051005.

[15] Cooley, C. G., Liu, C., Dai, X., and Parker, R. G., 2016, "Gear tooth mesh stiffness: A comparison of calculationapproaches," Mechanism and Machine Theory, **105**, pp. 540–553.

[16] Harker, R. J. and Bollinger, J. G., 1967, "Instability potential of high speed gearing," Journal of Industrial Mathematics, **17**, pp. 39–55.

[17] Benton, M. and Seireg, A., 1981, "Factors influencing instability and resonances in geared systems," ASME Journal of Mechanical Design, **103**(2), pp. 372–378.

[18] Amabili, M. and Rivola, A., 1997, "Dynamic analysis of spur gear pairs: steady-state response and stability of the sdof model with time-varying meshing damping," Mechanical systems and signal processing, **11**(3), pp. 375–390.

[19] Raghothama, A. and Narayanan, S., 1999, "Bifurcation and chaos in geared rotor bearing system by incremental harmonic balance method," Journal of Sound and Vibration, **226**(3), pp. 469–492.

[20] Theodossiades, S. and Natsiavas, S., 2001, "Periodic and chaotic dynamics of motor-driven gear-pair systems with backlash," Chaos, Solitons & Fractals, **12**(13), pp. 2427–2440.

[21] Litak, G. and Friswell, M. I., 2003, "Vibration in gear systems," Chaos, Solitons & Fractals, **16**(5), pp. 795–800.

[22] Ichimaru, K. and Hirano, F., 1974, "Dynamic behavior of heavy-loaded spur gears," ASME Journal of Engineering for Industry, **96**(2), pp. 373–381.

[23] Lee, C., Oswald, F. B., Townsend, D. P., and Lin, H. H., 1991, "Influence of linear profile modification and loading conditions on the dynamic tooth load and stress of high-contact-ratio spur gears," ASME Journal of Mechanical Design, **113**(4), pp. 473–480.

[24] Lin, H. H., Oswald, F., Townsend, D., and Lee, C., 1993, "Computer-aided design of high-contact-ratio gears for minimum dynamic load and stress," ASME Journal of Mechanical Design, **115**(1), pp. 171–178.

[25] Kelley, B. and Lemanski, A., 1967, "Lubrication of involute gearing," *Proceedings of the Institution of Mechanical Engineers, Conference Proceedings*, vol. 182, SAGE Publications, pp. 173–184.

[26] Martin, K., 1978, "A review of friction predictions in gear teeth," Wear, **49**(2), pp. 201–238.

[27] Wu, S. and Cheng, H., 1991, "A friction model of partial-ehl contacts and its application to power loss in spur gears," Tribology Transactions, **34**(3), pp. 398–407.

[28] Velex, P. and Cahouet, V., 2000, "Experimental and numerical investigations on the influence of tooth friction in spur and helical gear dynamics," ASME Journal of Mechanical Design, **122**(4), pp. 515–522.

[29] Vaishya, M. and Singh, R., 2001, "Sliding friction induced non-linearity and parametric effects in gear dynamics," Journal of Sound and Vibration, **248**(4), pp. 671–694.

[30] Vaishya, M. and Singh, R., 2001, "Analysis of periodically varying gear mesh systems with coulomb friction using floquet theory," Journal of Sound and Vibration, **243**(3), pp. 525–545.

[31] Vaishya, M. and Singh, R., 2003, "Strategies for modeling friction in gear dynamics," ASME Journal of Mechanical Design, **125**(2), pp. 383–393.

[32] Liu, G. and Parker, R. G., 2008, "Impact of tooth friction and its bending effect on gear dynamics," Journal of Sound and Vibration, **320**(4-5), pp. 1039–1063.

[33] LIN, J. and Parker, R., 2001, "Parametric resonance in two-stage gears from fluctuating mesh stiffness," IFToMM International Journal of Gearing and Transmissions, **3**, pp. 127–134.

[34] Lin, J. and Parker, R. G., 2002, "Mesh stiffness variation instabilities in two-stage gear systems," ASME Journal of Vibration and Acoustics, **124**(1), pp. 68–76.

[35] Liu, G. and Parker, R. G., 2008, "Dynamic modeling and analysis of tooth profile modification for multimesh gear vibration," Journal of Mechanical Design, **130**(12), p. 121402.

[36] Liu, G. and Parker, R. G., 2008, "Nonlinear dynamics of idler gear systems," Nonlinear Dynamics, **53**(4), pp. 345–367.

[37] Liu, G. and Parker, R. G., 2012, "Nonlinear, parametrically excited dynamics of two-stage spur gear trains with mesh stiffness fluctuation," Proceedings of the Institution of Mechanical Engineers, Part C: Journal of Mechanical Engineering Science, p. 0954406212447509.

[38] Krantz, T. L., 1993, "Mechanical systems technology branch research summary, 1985-1992," Tech. rep., DTIC Document.

[39] Cooley, C. G. and Parker, R. G., 2014, "A review of planetary and epicyclic gear dynamics and vibrations research," Applied Mechanics Reviews, **66**(4), p. 040804.

[40] Cunliffe, F., Smith, J. D., and Welbourn, D. B., 1974, "Dynamic tooth loads in epicyclic gears," Journal of Engineering for Industry, **96**(2), pp. 578–584.

[41] Botman, M., 1976, "Epicyclic gear vibrations," Journal of Engineering for Industry, **98**(3), pp. 811–815.

[42] Frater, J., August, R., and Oswald, F. B., 1983, "Vibration in planetary gear systems with unequal planet stiffness," NASA, (TM-83428).

[43] Kahraman, A., 1994, "Natural modes of planetary gear trains," Journal of Sound and Vibration, **173**(1), pp. 125–130.

[44] Saada, A. and Velex, P., 1995, "An extended model for the analysis of the dynamic behavior of planetary trains," ASME Journal of Mechanical Design, **117**(2), pp. 241–247.

[45] Lin, J. and Parker, R. G., 1999, "Analytical characterization of the unique properties of planetary gear free vibration," ASME Journal of Vibration and Acoustics, **121**(3), pp. 316–321.

[46] Lin, J. and Parker, R. G., 1999, "Sensitivity of planetary gear natural frequencies and vibration modes to model parameters," Journal of Sound and Vibration, **228**(1), pp. 109–128.

[47] Lin, J. and Parker, R. G., 2000, "Structured vibration characteristics of planetary gears with unequally spaced planets," Journal of Sound and Vibration, **233**(5), pp. 921–928.

[48] Lin, J. and Parker, R. G., 2001, "Natural frequency veering in planetary gears," Mechanics of Structures and Machines, **29**(4), pp. 411–429.

[49] Sun, T. and Hu, H., 2003, "Nonlinear dynamics of a planetary gear system with multiple clearances," Mechanism and Machine Theory, **38**(12), pp. 1371–1390.

[50] Abousleiman, V. and Velex, P., 2006, "A hybrid 3d finite element/lumped parameter model for quasi-static and dynamic analyses of planetary/epicyclic gear sets," Mechanism and Machine Theory, **41**(6), pp. 725–748.

[51] Ambarisha, V. K. and Parker, R. G., 2007, "Nonlinear dynamics of planetary gears using analytical and finite element models," Journal of Sound and Vibration, **302**(3), pp. 577–595.

[52] Al-Shyyab, A. and Kahraman, A., 2007, "A non-linear dynamic model for planetary gear sets," Proceedings of the Institution of Mechanical Engineers, Part K: Journal of Multi-body Dynamics, **221**, pp. 567–576.

[53] Eritenel, T. and Parker, R. G., 2009, "Modal properties of three-dimensional helical planetary gears," Journal of Sound and Vibration, **325**(1-2), pp. 397–420.

[54] Guo, Y. and Parker, R. G., 2010, "Dynamic modeling and analysis of a spur planetary gear involving tooth wedging and bearing clearance nonlinearity," European Journal of Mechanics A/Solids, **29**, pp. 1022–1033.

[55] Guo, Y. and Parker, R. G., 2012, "Dynamic analysis of planetary gears with bearing clearance," ASME Journal of Computational and Nonlinear Dynamics, **7**(1), p. 041002.

[56] Bahk, C.-J. and Parker, R. G., 2011, "Analytical solution for the nonlinear dynamics of planetary gears," ASME Journal of Computational and Nonlinear Dynamics, **6**(2), p. 021007.

[57] Bahk, C.-J. and Parker, R. G., 2013, "Analytical investigation of tooth profile modification effects on planetary gear dynamics," Mechanism and Machine Theory, **70**, pp. 298–319.

[58] Ericson, T. E. and Parker, R. G., 2013, "Planetary gear modal vibration experiments and correlation against lumped-parameter and finite element models," Journal of Sound and Vibration, **332**(9), pp. 2350–2375, .

[59] Seager, D. L., 1975, "Conditions for the neutralization of excitation by the teeth in epicyclic gearing," Journal of Mechanical Engineering Science, **17**(5), pp. 293–298.

[60] August, R. and Kasuba, R., 1986, "Torsional vibrations and dynamic loads in a basic planetary gear system," ASME Journal of Vibration, Acoustics, Stress, and Reliability in Design, **108**(3), pp. 348–353.

[61] Velex, P. and Flamand, L., 1996, "Dynamic response of planetary trains to mesh parametric excitations," ASME Journal of Mechanical Design, **118**(1), pp. 7–14.

[62] Kahraman, A., 1994, "Planetary gear train dynamics," ASME Journal of Mechanical Design, **116**(3), pp. 713–720.

[63] Parker, R. G., 2000, "A physical explanation for the effectiveness of planet phasing to suppress planetary gear vibration," Journal of Sound and Vibration, **236**, pp. 561–573.

[64] Lin, J. and Parker, R. G., 2004, "Mesh phasing relationships in planetary and epicyclic gears," ASME Journal of Mechanical Design, **126**, pp. 365–370.

[65] Ambarisha, V. K. and Parker, R. G., 2006, "Suppression of planet mode response in planetary gear dynamics through mesh phasing," ASME Journal of Vibration and Acoustics, **128**(2), pp. 133–142.

[66] Lin, J. and Parker, R. G., 2002, "Planetary gear parametric instability caused by mesh stiffness variation," Journal of Sound and Vibration, **249**(1), pp. 129–145.

[67] Vangipuram Canchi, S. and Parker, R. G., 2008, "Effect of ring-planet mesh phasing and contact ratio on the parametric instabilities of a planetary gear ring," ASME Journal of Mechanical Design, **130**, p. 014501.

[68] Kahraman, A., 1994, "Load sharing characteristics of planetary transmissions," Mechanism and Machine Theory, **29**(8), pp. 1151–1165.

[69] Ligata, H., Kahraman, A., and Singh, A., 2009, "A closed-form planet load sharing formulation for planetary gear sets using a translational analogy," ASME Journal of Mechanical Design, **131**(2), p. 021007.

[70] Singh, A., 2010, "Load sharing behavior in epicyclic gears: Physical explanation and generalized formulation," Mechanism and Machine Theory, **45**(3), pp. 511–530.

[71] Montestruc, A. N., 2010, "A numerical approach to calculation of load sharing in planetary gears," ASME Journal of Mechanical Design, **132**(1), p. 014503.

[72] Singh, A., 2011, "Epicyclic load sharing map - development and validation," Mechanism and Machine Theory, **46**(5), pp. 632–646.

[73] Gu, X. and Velex, P., 2011, "A lumped parameter model to analyse the dynamic load sharing in planetary gears with planet errors," Applied Mechanics and Materials, **86**, pp. 374–379.

[74] Gu, X. and Velex, P., 2012, "A dynamic model to study the influence of planet position errors in planetary gears," Journal of Sound and Vibration, **331**(20), pp. 4554–4574.

[75] Gu, X. and Velex, P., 2013, "On the dynamic simulation of eccentricity errors in planetary gears," Mechanism and Machine Theory, **61**, pp. 14–29.

[76] Inalpolat, M. and Kahraman, A., 2008, "Dynamic modelling of planetary gears of automatic transmissions," Proceedings of the Institution of Mechanical Engineers, Part K: Journal of Multi-body Dynamics, **222**(3), pp. 229–242.

[77] Inalpolat, M. and Kahraman, A., 2009, "A theoretical and experimental investigation of modulation sidebands of planetary gear sets," Journal of Sound and Vibration, **323**(3-5), pp. 677–696.

[78] Inalpolat, M. and Kahraman, A., 2010, "A dynamic model to predict modulation sidebands of a planetary gear set having manufacturing errors," Journal of Sound and Vibration, **329**(4), pp. 371–393.

[79] Cooley, C. G. and Parker, R. G., 2012, "Vibration properties of high-speed planetary gears with gyroscopic effects," ASME Journal of Vibration and Acoustics, **134**(6), p. 061014.

[80] Cooley, C. G. and Parker, R. G., 2013, "Mechanical stability of high-speed planetary gears," International Journal of Mechanical Sciences, **69**, pp. 59–71.

[81] Cooley, C. G. and Parker, R. G., 2013, "Unusual gyroscopic system eigenvalue behaviour in high-speed planetary gears," Journal of Sound and Vibration, **332**(7), pp. 1820–1828.

[82] Abousleiman, V., Velex, P., and Becquerelle, S., 2007, "Modeling of spur and helical gear planetary drives with flexible ring gears and planet carriers," ASME Journal of Mechanical Design, **129**(1), pp. 95 –106.

[83] Wu, X. and Parker, R. G., 2008, "Modal properties of planetary gears with an elastic continuum ring gear," ASME Journal of Applied Mechanics, **75**(3), p. 031014.

[84] Parker, R. and Wu, X., 2010, "Vibration modes of planetary gears with unequally spaced planets and an elastic ring gear," Journal of Sound and Vibration, **329**(11), pp. 2265–2275.

[85] Parker, R. G. and Wu, X., 2012, "Parametric instability of planetary gears with elastic continuum ring gears," ASME Journal of Vibration and Acoustics, **134**(4), p. 041011.

[86] Kahraman, A., 2001, "Free torsional vibration characteristics of compound planetary gear sets," Mechanism and Machine Theory, **36**(8), pp. 953–971.

[87] Kiracofe, D. R. and Parker, R. G., 2007, "Structured vibration modes of general compound planetary gear systems," ASME Journal of Vibration and Acoustics, **129**(1), pp. 1–16.

[88] Guo, Y. and Parker, R. G., 2010, "Sensitivity of general compound planetary gear natural frequencies and vibration modes to modal parameters," ASME Journal of Vibration and Acoustics, **132**(1), p. 011006.

[89] Guo, Y. and Parker, R. G., 2010, "Purely rotational model and vibration modes of compound planetary gears," Mechanism and Machine Theory, **45**(3), pp. 365–377.

[90] Guo, Y. and Parker, R. G., 2011, "Analytical determination of mesh phase relations in general compound planetary gears," Mechanism and Machine Theory, **46**, pp. 1869–1887.

[91] Sondkar, P. and Kahraman, A., 2013, "A dynamic model of a double-helical planetary gear set," mechanism and machine Theory, **70**, pp. 157–174.

[92] Ericson, T. M. and Parker, R. G., 2013, "Natural frequency clusters in planetary gear vibration," ASME Journal of Vibration and Acoustics, **135**(6), p. 061002.

[93] Chabert, G., Tran, T. D., and Mathis, R., 1974, "An evaluation of stresses and deflection of spur gear teeth under strain," ASME Journal of Engineering for Industry, **96**(1), pp. 85–93.

[94] Oda, S., Nagamura, K., and Aoki, K., 1981, "Stress analysis of thin rim spur gears by finite element method," Bulletin of JSME, **24**(193), pp. 1273–1280.

[95] Oda, S., Miyachika, K., Koide, T., and Mizune, M., 1986, "Stress analysis of thin-rimmed spur gears by boundary element method," Bulletin of JSME, **29**(248), pp. 593–599.

[96] Bibel, G. D., Reddy, S., Handschuh, R., and Savage, M., 1994, "Effects of rim thickness on spur gear bending stress," ASME Journal of Mechanical Design, **116**(4), pp. 1157–1162.

[97] Baud, S. and Velex, P., 2002, "Static and dynamic tooth loading in spur and helical geared systems-experiments and model validation," ASME Journal of Mechanical Design, **124**(2), pp. 334–346.

[98] Wang, J. and Howard, I., 2005, "Finite element analysis of high contact ratio spur gears in mesh," Journal of Tribology, **127**(3), pp. 469–483.

[99] Kawalec, A., Ceglarek, D., and Wiktor, J., 2006, "Comparative analysis of tooth-root strength using ISO and AGMA standards in spur and helical gears with fem-based verification," ASME Journal of Mechanical Design, **128**(5), pp. 1141–1158.

[100] Thirumurugan, R. and Muthuveerappan, G., 2010, "Maximum fillet stress analysis based on load sharing in normal contact ratio spur gear drives," Mechanics Based Design of Structures and Machines, **38**(2), pp. 204–226.

[101] Palmer, D. and Fish, M., 2010, "Evaluation of methods for calculating effects of tip relief on transmission error, noise and stress in loaded spur gears," American Gear Manufacturers Association Fall Technical Meeting 2010, pp. 112–126.

[102] Li, N., Li, W., Liu, N., and Liu, H. G., 2011, "Analytical method on contact stress of helical gear with asymmetric involutes," Advanced Materials Research, **321**, pp. 157–160.

[103] Li, S., 2012, "Contact stress and root stress analyses of thin-rimmed spur gears with inclined webs," ASME Journal of Mechanical Design, **134**(5), p. 051001.

[104] Vijayakar, S. M., Busby, H. R., and Houser, D. R., 1988, "Linearization of multibody frictional contact problems," Computers and Structures, **29**(4), pp. 569–576.

[105] Vijayakar, S. M., Busby, H. R., and Wilcox, L., 1989, "Finite element analysis of three-dimensional conformal contact with friction," Computers and Structures, **33**(1), pp. 49–61.

[106] Vijayakar, S. M., 1991, "A combined surface integral and finite element solution for a three-dimensional contact problem," International Journal for Numerical Methods in Engineering, **31**(3), pp. 525–545.

[107] Parker, R. G., Agashe, V., and Vijayakar, S. M., 2000, "Dynamic response of a planetary gear system using a finite element/contact mechanics model," ASME Journal of Mechanical Design, **122**(3), pp. 304–310.

[108] Parker, R. G., Vijayakar, S. M., and Imajo, T., 2000, "Non-linear dynamic response of a spur gear pair: Modelling and experimental comparisons," Journal of Sound and Vibration, **237**(3), pp. 435–455.

[109] Cooley, C. G., Parker, R. G., and Vijayakar, S. M., 2011, "A frequency domain finite element approach for three-dimensional gear dynamics," ASME Journal of Vibration and Acoustics, **133**, p. 041004.

[110] Kahraman, A. and Vijayakar, S. M., 2001, "Effect of internal gear flexibility on the quasi-static behavior of a planetary gear set," ASME Journal of Mechanical Design, **123**(3), pp. 408–415.

[111] Kahraman, A., Kharazi, A. A., and Umrani, M., 2003, "A deformable body dynamic analysis of planetary gears with thin rims," Journal of Sound and Vibration, **262**(3), pp. 752–768.

[112] Bodas, A. and Kahraman, A., 2004, "Influence of carrier and gear manufacturing errors on the static load sharing behavior of planetary gear sets," JSME International Journal Series C, **47**(3), pp. 908–915.

[113] Cheon, G.-J. and Parker, R. G., 2004, "Influence of manufacturing errors on the dynamic characteristics of planetary gear systems," KSME International Journal, **18**(4), pp. 606–621.

[114] Cheon, G.-J. and Parker, R. G., 2004, "Influence of bearing stiffness on the static properties of a planetary gear system with manufacturing errors," KSME International Journal, **18**(11), pp. 1978–1988.

[115] Yuksel, C. and Kahraman, A., 2004, "Dynamic tooth loads of planetary gear sets having tooth profile wear," Mechanism and Machine Theory, **39**, pp. 695–715.

[116] Singh, A., 2005, "Application of a system level model to study the planetary load sharing behavior," Journal of Mechanical Design, **127**(3), pp. 469–476.

[117] Singh, A., 2007, "Influence of planetary needle bearings on the performance of single and double pinion planetary systems," ASME Journal of Mechanical Design, **129**(1), pp. 85–94.

[118] Tamminana, V. K., Kahraman, A., and Vijayakar, S., 2007, "A study of the relationship between the dynamic factors and the dynamic transmission error of spur gear pairs," ASME Journal of Mechanical Design, **129**(1), pp. 75–84.

[119] Guo, Y. and Parker, R. G., 2012, "Stiffness matrix calculation of rolling element bearings using a finite element/contact mechanics model," Mechanism and Machine Theory, **51**, pp. 32–45.

[120] Kahraman, A. and Blankenship, G. W., 1997, "Experiments on nonlinear dynamic behavior of an oscillator with clearance and periodically time-varying parameters," ASME Journal of Applied Mechanics, **64**(1), pp. 217–226.

[121] Kahraman, A. and Blankenship, G. W., 1999, "Effect of involute tip relief on dynamic response of spur gear pairs," ASME Journal of Mechanical Design, **121**(5), pp. 313–315.

[122] Harris, S. L., 1957, "Dynamic loads on the teeth of spur gears," Proceedings of the Institution of Mechanical Engineers, **172**, pp. 87–100.

[123] Wang, M.-J., 2003, "A new photoelastic investigation of the dynamic bending stress of spur gears," ASME Journal of Mechanical Design, **125**(2), pp. 365–372.

[124] Chong, T.-H., Suzuki, T., Aida, T., and Fujio, H., 1982, "Bending stresses of internal spur gear," Bulletin of JSME, **25**(202), pp. 679–686.

[125] Houser, D. R. and Seireg, A., 1970, "An experimental investigation of dynamic factors in spur and helical gears," Journal of Engineering for Industry, **92**(2), pp. 495–503.

[126] Rao, S. B., Schwanger, V., McPherson, D. R., and Rudd, C., 2005, "Measurement and validation of dynamic bending stresses in spur gear teeth," *ASME 2005 International Design Engineering Technical Conferences*, American Society of Mechanical Engineers, pp. 755–764.

[127] Hotait, M. and Kahraman, A., 2008, "Experiments on root stresses of helical gears with lead crown and misalignments," ASME Journal of Mechanical Design, **130**(7), p. 074502.

[128] Botman, M., 1980, "Vibration measurement on planetary gears of aircraft turbine engines," Journal of Aircraft, **17**(5), pp. 351–357.

[129] Krantz, T. L., 1991, "Gear tooth stress measurements of two helicopter planetary stages," Tech. Rep. 91-C-038, NASA Technical Report.

[130] Kahraman, A., 1999, "Static load sharing characteristics of transmission planetary gear sets: Model and experiment," SAE Technical Paper Series, pp. 1999–01–1050.

[131] Ligata, H., Kahraman, A., and Singh, A., 2008, "An experimental study of the influence of manufacturing errors on the planetary gear stresses and planet load sharing," ASME Journal of Mechanical Design, **130**(4), p. 041701.

[132] Singh, A., Kahraman, A., and Ligata, H., 2008, "Internal gear strains and load sharing in planetary transmissions: Model and experiments," ASME Journal of Mechanical Design, **130**(7), p. 072602.

[133] Kahraman, A., Ligata, H., and Singh, A., 2010, "Influence of ring gear rim thickness on planetary gear set behavior," ASME Journal of Mechanical Design, **132**(2), p. 021002.

[134] Boguski, B., Kahraman, A., and Nishino, T., 2012, "A new method to measure planet load sharing and sun gear radial orbit of planetary gear sets," Journal of Mechanical Design, **134**(7), p. 071002.

[135] Dai, X., Cooley, C. G., and Parker, R. G., 2016, "Dynamic tooth root strains and experimental correlations in spur gear pairs," Mechanism and Machine Theory, **101**, pp. 60–74.

[136] Kahraman, A. and Singh, R., 1990, "Non-linear dynamics of a spur gear pair," Journal of Sound and Vibration, **142**(1), pp. 49–75.

[137] Vinayak, H. and Singh, R., 1998, "Multi-body dynamics and modal analysis of compliant gear bodies," Journal of Sound and Vibration, **210**(2), pp. 171–214.

[138] Vinayak, H., Singh, R., and Padmanabhan, C., 1995, "Linear dynamic analysis of multi-mesh transmissions containing external, rigid gears," Journal of Sound and Vibration, **185**(1), pp. 1–32.

[139] Sainte-Marie, N., Velex, P., Roulois, G., and Caillet, J., 2017, "A study on the correlation between dynamic transmission error and dynamic tooth loads in spur and helical gears," Journal of Vibration and Acoustics, **139**(1), pp. 011–001.

[140] Benton, M. and Seireg, A., 1978, "Simulation of resonances and instability conditions in pinion-gear systems," Journal of Mechanical Design, **100**(1), pp. 26–32.

[141] Kahraman, A. and Singh, R., 1991, "Interactions between time-varying mesh stiffness and clearance non-linearities in a geared system," Journal of Sound and Vibration, **146**(1), pp. 135–156.

[142] Cai, Y., 1995, "Simulation on the rotational vibration of helical gears in consideration of the tooth separation phenomenon," ASME Journal of Mechanical Design, **117**(3), pp. 460–469.

[143] Kahraman, A. and Blankenship, G. W., 1996, "Interactions between commensurate parametric and forcing excitations in a system with clearance," Journal of Sound and Vibration, **194**(3), pp. 317–336.

[144] Theodossiades, S. and Natsiavas, S., 2000, "Non-linear dynamics of gear-pair systems with periodic stiffness and backlash," Journal of Sound and Vibration, **229**(2), pp. 287–310.

[145] Palermo, A., Mundo, D., Hadjit, R., and Desmet, W., 2012, "Effects of variable loads and misalignments on gear noise and vibration through multibody simulation based on transmission error," in Proceedings of the International Conference on Noise and

Vibration Engineering and 4th International Conference on Uncertainty in Structural Dynamics, pp. 3995–4006.

[146] Palermo, A., Mundo, D., Hadjit, R., and Desmet, W., 2013, "Multibody element for spur and helical gear meshing based on detailed three-dimensional contact calculations," Mechanism and Machine Theory, **62**, pp. 13–30.

[147] Korta, J., Palermo, A., Mundo, D., and Shweiki, S., 2015, "Combining finite element and multibody modeling techniques for time-efficient simulation of nonlinear gear dynamics," The Seventh International Conference on Advances in System Simulation.

[148] Hidaka, T., Terauchi, Y., and Fujii, M., 1980, "Analysis of dynamic tooth load on planetary gear," Bulletin of JSME, **23**(176), pp. 315–323.

[149] Dai, X., Cooley, C. G., and Parker, R. G., 2017, "An efficient hybrid analytical-computational method for nonlinear gear dynamics in multi-mesh systems," in preparation.